Astronomy Unit
School of Physics and Astronomy
Queen Mary, University of London

Relativistic effects in the galaxy bispectrum

Eline Maaike de Weerd

Supervised by Dr. Chris Clarkson & Dr. Alkistis Pourtsidou

Submitted in partial fulfillment of the requirements of the Degree of
Doctor of Philosophy

Declaration

I, Eline Maaike de Weerd, confirm that the research included within this thesis is my own work or that where it has been carried out in collaboration with, or supported by others, that this is duly acknowledged below and my contribution indicated. Previously published material is also acknowledged below.

I attest that I have exercised reasonable care to ensure that the work is original, and does not to the best of my knowledge break any UK law, infringe any third party's copyright or other Intellectual Property Right, or contain any confidential material.

I accept that the College has the right to use plagiarism detection software to check the electronic version of the thesis.

I confirm that this thesis has not been previously submitted for the award of a degree by this or any other university. The copyright of this thesis rests with the author and no quotation from it or information derived from it may be published without the prior written consent of the author.

Details of collaboration and publications: Part of this work has been done in collaboration with Stefano Camera, Chris Clarkson, Sheean Jolicoeur, Roy Maartens, and Obinna Umeh. It is based on the following publications, all of which I have contributed to:

- The dipole of the galaxy bispectrum
  C. Clarkson, E.M. De Weerd, S. Jolicoeur, R. Maartens, O. Umeh
  Published: *MNRAS Letters 486 (2019) L101*, arXiv: 1812.09512 [astro-ph.CO]

- Detecting the relativistic galaxy bispectrum
  R. Maartens, S. Jolicoeur, O. Umeh, E.M. De Weerd, C. Clarkson, S. Camera
  Published: *JCAP03(2020)065*, arXiv: 1911.02398 [astro-ph.CO]

- Multipoles of the relativistic galaxy bispectrum
  E.M. De Weerd, C. Clarkson, S. Jolicoeur, R. Maartens, O. Umeh
  Published: *JCAP05(2020)018*, arXiv: 1912.11016 [astro-ph.CO]

- Detecting the relativistic bispectrum in 21cm intensity maps
  S. Jolicoeur, R. Maartens, E.M. De Weerd, O. Umeh, C. Clarkson, S. Camera
  Published: *JCAP06(2021)039*, arXiv: 2009.06197 [astro-ph.CO]

- Local primordial non-Gaussianity in the relativistic galaxy bispectrum
  R. Maartens, S. Jolicoeur, O. Umeh, E.M. De Weerd, C. Clarkson
  Published: *JCAP04(2021)013*, arXiv: 2011.13660 [astro-ph.CO]

Signature: Eline Maaike de Weerd
Date: xx.xx.2021

Abstract

Next-generation galaxy surveys will provide us with a wealth of high-precision cosmological data. To be able to use this information in an as unbiased manner as possible, theoretical accuracy must match the experimental precision. The three-point function, or bispectrum, is the first of the higher-order statistics beyond the power spectrum, and contains information both complementary and additional to what is contained in the power spectrum.

On large scales, the galaxy bispectrum will be a key probe for measuring primordial non-Gaussianity, improve constraints on cosmological parameters, and hence help discriminate between various models of inflation and other theories of the early universe. On these scales, a variety of relativistic effects come into play once the galaxy number-count fluctuation is projected onto the past light cone. It is important for these effects to be taken into account in our theoretical treatment of the bispectrum, as they will contaminate the primordial non-Gaussian signal and bias measurements.

In this thesis, we review the relativistic projection effects in the galaxy bispectrum, and examine in detail how these relativistic effects contribute to the invariant multipoles of the galaxy bispectrum about the observer's line of sight. The Fourier-space bispectrum is complex, with an imaginary part arising from the relativistic effects only, which generates odd multipoles. This means that detection of this imaginary part is a smoking gun signal of the relativistic contributions, and we show that such a signal is in principle detectable in future surveys, although with a higher signal-to-noise ratio for spectroscopic surveys compared to 21cm intensity mapping surveys. Finally, we include local primordial non-Gaussianity in the theoretical description of the relativistic bispectrum, separating the relativistic corrections from the primordial signal, and use the bispectrum in Fisher matrix forecasts for cosmological parameters.

Acknowledgements

Round up the usual suspects

Contents

1. Introduction

Some introduction! General overview of the current observational state of things to make bispectrum work more relevant.

2. Statistics of galaxy clustering

Desciption of the role of statistics in cosmology

The galaxy bispectrum is the Fourier-space equivalent of the three-point function and is as such the first of the higher-order statistics beyond the power spectrum. Next-generation large scale structure such as Euclid (galaxy) and the SKA (21cm intensity mapping) will rely on a combination of the power spectrum and the bispectrum for high-precision measurements of primordial non-Gaussianity and for improvement of constraints on cosmological parameters. In particular, improvement on constraints on the primordial non-Gaussian parameter $f_{\rm NL}$ will be crucial for discrimitation between various models of inflation and other theories of the early universe.

As it stands, our current understanding of the universe is that large scale structure of matter is a result of the growth of small primordial fluctuations which have functioned as seeds for structure growth in an otherwise homogeneous universe. These small fluctuations have been amplified by gravitatational instability, resulting in the formation of the structure that we know as the cosmic web on cosmological scales. Tests of theories describing these primordial fluctuations are statistical in nature for the following reasons. For one, there is no direct observationa access to primordial fluctuations, and additionally, the time-scales required to follow cosmological evolution of systems is much much longer than that over which observations are realistically possible. In essence this means that observations on the past lightcone how different objects at different phases of their evolution, and as a result tests of the evolution of large scale structure must be carried out statistically.

A goal of theoretical cosmology is to make statistical predictions which depend on the statistical properties of primordial perturbations, which in turn lead to the formation of large scale structures in the universe. In these models, the observable universe is modelled simply as a stochastic realisation of a statistical ensemble of possibilities. The most widely considered models are based on the inflationary paradism, and generically give rise to adiabatic Gaussian initial fluctuations. In this case, the origin of stochasticity lies in quantum fluctuations that were generated in the early universe.

2.1. The two-point function

A purely Gaussian field is fully described by the two-point correlation function or power spectrum. The two-point correlation function is defined as the joint ensemble average of the density at two different points $\boldsymbol{x}$ and $\boldsymbol{x} + \mathbf{r}$, i.e.

$$\xi(r) = \langle \delta(\boldsymbol{x})\delta(\boldsymbol{x} + \mathbf{r})\rangle, \tag{2.1}$$

which is dependent on the distance r between the two points only, due to statistical homogeneity and isotropy which are assumed throughout. Usually, the density contrast δ is expressed in terms of its Fourier space components, where our Fourier convention is

$$\delta(\boldsymbol{x}) = \int \frac{\mathrm{d}^3 k}{(2\pi)^3}\, e^{\mathrm{i}\,\boldsymbol{k}\cdot\boldsymbol{x}}\delta(\boldsymbol{x}), \tag{2.2}$$

where $\delta(\boldsymbol{k})$ are complex random variables. Note that there are generally two Fourier conventions that are used in literature on the galaxy statistics, which lead to a difference of $(2\pi)^3$ in the definition of the power spectrum or two-point function. The other choice of Fourier convention is to reverse where the factor of $(2\pi)^3$ goes in the Fourier transforms, that is, using $f(\boldsymbol{x}) = \int \mathrm{d}^3 k e^{\mathrm{i}\,\boldsymbol{k}\cdot\boldsymbol{x}} f(\boldsymbol{k})$ and $f(\boldsymbol{k}) = \int \frac{\mathrm{d}^3 x}{(2\pi)^3} e^{-\mathrm{i}\,\boldsymbol{k}\cdot\boldsymbol{x}} f(\boldsymbol{x})$ instead of our convention used here.

Since the density contrast is real, this means that we have

$$\delta(k) = \delta^*(-\boldsymbol{k}). \tag{2.3}$$

Similarly, the correlators can also be computed in Fourier space, as follows,

$$\langle \delta(\boldsymbol{k})\delta(\boldsymbol{k}')\rangle = \int \mathrm{d}^3 x\, \mathrm{d}^3 r \langle \delta(\boldsymbol{x})\delta(\boldsymbol{x} + \boldsymbol{r})\rangle e^{-\mathrm{i}\,(\boldsymbol{k}+\boldsymbol{k}')\cdot\boldsymbol{x} - \mathrm{i}\,\boldsymbol{k}'\cdot\boldsymbol{r}}. \tag{2.4}$$

This can be rewritten using the definition of the two-point correlation function as

$$\langle\delta(\boldsymbol{k})\delta(\boldsymbol{k}')\rangle = \int \mathrm{d}^3x\,\mathrm{d}^3r\xi(r)e^{-\mathrm{i}\,(\boldsymbol{k}+\boldsymbol{k}')\cdot\boldsymbol{x}-\mathrm{i}\,\boldsymbol{k}'\cdot\boldsymbol{r}}, \tag{2.5}$$

and, performing one of the intregrals,

$$\langle\delta(\boldsymbol{k})\delta(\boldsymbol{k}')\rangle = (2\pi)^3\delta^D(\boldsymbol{k}+\boldsymbol{k}')\int \mathrm{d}^3r\xi(r)e^{\mathrm{i}\,\boldsymbol{k}\cdot\boldsymbol{r}} \tag{2.6}$$

$$\equiv (2\pi)^3\delta^D(\boldsymbol{k}+\boldsymbol{k}')P(k), \tag{2.7}$$

where $P(k)$ is by definition the density power spectrum.

2.2. The three-point function

Higher-order correlation functions are defined as the connected part of the joint ensemble average of the density in an arbitrary number of locations. In principle it is possible define any order of correlation function like this, but they will rapidly become more computationally complex and expensive. In the case of a purely Gaussian field, the only non-vanishing connected part is the two-point correlation function. This is a direct consequence of Wick's theorem for Gaussian fields, and has a number of important consequences. Firstly it means that a purely Gaussian, statistically homogeneous and isotropic field is fully described by its two-point correlation function or power spectrum, and secondly it means that the statistical properties of any field, which is not necessarily linear, can be written in terms of combinations of two-point correlation functions – as long as the field is built from a Gaussian field δ. In a generic form, Wick's theorem can be expressed as

$$\begin{aligned}\langle\delta(\boldsymbol{k}_1)\ldots\delta(\boldsymbol{k}_{2p+1})\rangle &= 0\\ \langle\delta(\boldsymbol{k}_1)\ldots\delta(\boldsymbol{k}_{2p})\rangle &= \sum_{[\text{all distinct pairs}]}\ \prod_{[p\text{ pairs }(i,j)]}\langle\delta(\boldsymbol{k}_i)\delta(\boldsymbol{k}_j)\rangle.\end{aligned} \tag{2.8}$$

More concretely, this means that for a purely Gaussian field, $\langle\delta(\boldsymbol{k}_1)\delta(\boldsymbol{k}_2)\delta(\boldsymbol{k}_3)\rangle = 0$. However, this changes in the presence of any sources of non-linearity. BLAH. An important consequence of non-linear evolution of structure is that the statistics of odd-number density fields are no longer vanishing. The leading odd-number statistic which will be non-zero in the case of non-linear evolution if the three-point correlation function or the bispectrum in Fourier space,

$$\langle \delta(\boldsymbol{k}_1)\delta(\boldsymbol{k}_2)\delta(\boldsymbol{k}_3)\rangle = (2\pi)^3\delta^{\mathrm{D}}(\boldsymbol{k}_1+\boldsymbol{k}_2+\boldsymbol{k}_3)\left[2F_2(\boldsymbol{k}_1,\boldsymbol{k}_2)P_{\mathrm{L}}(\boldsymbol{k}_1)P_{\mathrm{L}}(\boldsymbol{k}_2) + \text{ 2 c.p.}\right] \quad (2.9)$$

where F_2 is the Fourier space density evolution kernel, P_{L} is the linear power spectrum from the previous discussion, and redshift dependence is suppressed for brevity.

Some blah blah about higher order statistics and their importance in future surveys (higher precision data, non-Gaussianities in the universe and effects that give rise to nonlinearities)

2.2.1. The matter bispectrum

The bispectrum is a non-Gaussian statistic, and as such is especially sensitive to any forms of non-linearity in the universe. It is an essential probe for e.g. primordial non-Gaussianity, though there are also other sources of non-Gaussianities in the universe. Primordial non-Gaussianity, which is often parametrised by the non-linear parameter f_{NL}, is predicted by different types of inflation and other theories of the early universe; meaning that improvement of constraints on f_{NL} could help discriminate between these theories and help shed light on the very early universe and the seeds of structure formation.

In this section we will go into more detail as to how various amplitudes and signs of the bispectrum correspond to real-space signatures. The bispectrum in Fourier space forms a closed triangle correlating three different wave-vectors and, unlike the power spectrum or two-point function, is able to correlate different scales. The matter bispectrum is unique from the thus far more well-studied CMB bispectrum in that it is able to form a three-dimensional map of the universe, whereas the cosmic microwave background provides a two-dimensional snapshot of the first light only. It is therefore essential to try and improve the theoretical description of the matter bispectrum if we are to utilise the wealth of information from next-generation high-precision galaxy surveys in as good and as unbiased a manner as possible.

Where the power spectrum is a measure of probability of, e.g. in the case of the galaxy power spectrum, finding galaxies at distance corresponding to separation of points r from each other, the bispectrum similarly maps this to a probability in a three-dimensional equivalent. That is, it can correspond directly to what we know as the cosmic web, and the galaxy or dark matter distributions therein. The bispectrum has degrees of freedom in both modulus of the wavevector i.e. scales of correlation, as well as the shape of the triangle itself. Different triangle shapes correspond to different real-space bispectrum signatures.

Theoretical blah about the matter bispectrum, definitions, showing how various bispectrum signals translate to real space shapes and modulations of signal

2.2.2. Matter bispectrum in observations

Bispectrum in observation – can skip over any CMB and just focus on lss

2.3. Galaxy bias

(Very) brief overview of the relevant bias

2.4. Primordial non-Gaussianity

Types of primodial non-Gaussianity in the bispectrum, their signatures on various scales, scale dependence it introduces in the clustering bias etc.

cum sit enim proprium
viro sapienti
supra petram ponere
sedem fundamenti
stultus ego comparor
fluvio labenti
sub eodem tramite
nunquam permanenti

3. Relativistic effects

Relativistic effects in galaxy number counts at first and second order

Observations in large scale structure surveys pose a variety of challenges. As opposed to CMB observations, in which in great detail temperature fluctuations can be measured and mapped, LSS surveys have the downside that one observes galaxies and not the underlying density field. Since galaxies are a biased tracer of the underlying density field, this in itself imposes the problem of how galaxy clustering biases measurements. Furthermore, there are various sources of non-linearities in galaxy clustering, which give rise to non-trivial higher order correlations aside from the power spectrum. Where a purely Gaussian field is fully described by the power spectrum, that is, all statistical information about the field is contained therein and odd correlators vanish identically, in the case of non-Gaussianities the three-point correlations and higher are generated and are needed in addition to the power spectrum to describe the field at high enough accuracy.

For a highly non-linear regime it would probably be necessary to turn to full numerical simulations for an analysis, but in the intermediate, weakly non-linear regime, higher order perturbation theory can be used for our analysis. In this chapter I will discuss the relativistic effects on galaxy number counts at first and second order.

In a typical galaxy survey, the observer looks down the past lightcone and observes some number of galaxies $\mathrm{d}N$, which are above some threshold luminosity L, in a redshift interval $\mathrm{d}z$ and within an element of solid angle $\mathrm{d}\Omega_o$, about direction of observation $\boldsymbol{n}$.

The fractional perturbation of observed number counts Δ_g is defined by

$$\frac{\mathrm{d}N(z,\boldsymbol{n},>\ln L)}{\mathrm{d}z\,\mathrm{d}\Omega_o} = \frac{\chi^2(z)}{(1+z)^4\mathcal{H}(z)}\bar{\mathcal{N}}(z,>\ln L)\left[1+\Delta_g(z,\boldsymbol{n},>\ln L)\right], \tag{3.1}$$

where $\mathcal{H}$ is the conformal Hubble rate, χ is the comoving line-of-sight distance, and $\bar{\mathcal{N}}$ is the background magnitude-limited number density of sources. The dependence of Δ_g on $\ln L$ will be suppressed for brevity. Expanding Δ_g up to second order in perturbation theory as follows,

$$\Delta_g(z, \boldsymbol{n}) = \Delta_g^{(1)}(z, \boldsymbol{n}) + \frac{1}{2}\left[\Delta_g^{(2)}(z, \boldsymbol{n}) - \langle \Delta_g^{(2)}(z, \boldsymbol{n}) \rangle\right], \tag{3.2}$$

subtracting off the average value of $\Delta_g^{(2)}$ to ensure that $\langle \Delta_g \rangle = 0$.

3.1. First order

see title

3.2. Second order

see title again

4. The Dipole of the Galaxy Bispectrum

4.1. The dipole

In this chapter we examine the leading-order relativistic contributions in the galaxy bispectrum, which arise predominantly from RSD and other Doppler-type observational effects. These give rise to corrections at $\mathcal{O}(\mathcal{H}/k)$ in the galaxy bispectrum. Higher order $\mathcal{H}/k$ contributions are, while being subdominant, still present in the galaxy bispectrum; and a full treatment of the bispectrum at all orders can be found in chapter 7.

The dominant RSD effect on galaxy number counts at first order is given by $\delta_g(z, \boldsymbol{k}) = (b_1(z) + f(z)\mu^2)\delta(z, \boldsymbol{k})$, where $\mu = \boldsymbol{n} \cdot \hat{\boldsymbol{k}}$, with $\boldsymbol{n}$ the line of sight direction, f the growth rate, and b_1 is the linear bias. Henceforth the redshift dependence will be dropped for brevity as we are working at fixed redshift. At leading order, there is a Doppler type correction to this effect (Kaiser, 1987; McDonald, 2009; Challinor & Lewis, 2011) (see also (Raccanelli et al., 2018; Hall & Bonvin, 2017; Abramo & Bertacca, 2017)) proportional to $\boldsymbol{v} \cdot \boldsymbol{n}$, where $\boldsymbol{v}$ is the peculiar velocity:[1]

$$\delta_g(\boldsymbol{x}) = b_1\delta(\boldsymbol{x}) - \frac{1}{\mathcal{H}}\partial_r(\boldsymbol{v} \cdot \boldsymbol{n}) + A\,\boldsymbol{v} \cdot \boldsymbol{n} \quad \rightarrow \tag{4.1}$$

$$\delta_g(\boldsymbol{k}) = \Big(b_1 + f\mu^2 + \mathrm{i}\,A\,f\mu\frac{\mathcal{H}}{k}\Big)\delta(\boldsymbol{k})\,, \tag{4.2}$$

where

$$A = b_\mathrm{e} + 3\Omega_m/2 - 3 + (2 - 5s)(1 - 1/r\mathcal{H})\,. \tag{4.3}$$

Here $b_\mathrm{e} = \partial(a^3\bar{n}_g)/\partial \ln a$ is the evolution of comoving galaxy number density, $s = -(2/5)\partial \ln \bar{n}_g/\partial \ln L$ is the magnification bias (L is the threshold luminosity), r is the

[1](Challinor & Lewis, 2011) provides the relativistic correction to the coefficient of $\boldsymbol{v} \cdot \boldsymbol{n}$ given in (Kaiser, 1987; McDonald, 2009).

comoving radial distance ($\partial_r = \boldsymbol{n}\cdot\boldsymbol{\nabla}$) and we have assumed a ΛCDM background ($\mathcal{H}'/\mathcal{H}^2 = 1-3\Omega_m/2$, where $\mathcal{H}$ is the conformal Hubble rate, a prime is differentiation with respect to conformal time, Ω_m is the evolving density contrast). In the Fourier space expression (4.2) we can read off the relative contribution of each term by how they scale with k: terms like $\mathcal{H}/k$ are suppressed on small scales when $\mathcal{H}/k \ll 1$ but become important around and above the equality scale.

Although the galaxy density contrast (4.2) is complex, the power spectrum of a single tracer is real:

$$\big\langle \delta_g(\boldsymbol{k})\delta_g(-\boldsymbol{k})\big\rangle = \left[\left(b_1 + f\mu^2\right)^2 + \left(A\, f\mu\frac{\mathcal{H}}{k}\right)^2\right]\big\langle \delta(\boldsymbol{k})\delta(-\boldsymbol{k})\big\rangle\,,$$

since $\mu_{-\boldsymbol{k}} = -\mu_{\boldsymbol{k}}$ enforces a cancellation of the imaginary part, and the RSD contribution is separate from the Doppler term. However, if we consider the cross-power spectrum for *two* matter tracers, this cancellation breaks down, and there is an imaginary part in the cross-power (McDonald, 2009; Bonvin, 2014),

$$\begin{aligned} P_{g\tilde{g}}(k) = \bigg\{&\left[\left(b_1 + f\mu^2\right)\left(\tilde{b}_1 + f\mu^2\right) + A\tilde{A}f^2\mu^2\frac{\mathcal{H}^2}{k^2}\right] \\ &+ \mathrm{i}\, f\mu\left[\left(\tilde{b}_1 + f\mu^2\right)A - \left(b_1 + f\mu^2\right)\tilde{A}\right]\frac{\mathcal{H}}{k}\bigg\}P(k)\,. \end{aligned}$$

While the Doppler contribution to P_g is $\mathcal{O}((\mathcal{H}/k)^2)$, the Doppler contribution to $P_{g\tilde{g}}$ mixes with the density and RSD to give an additional less suppressed part, i.e. $\mathcal{O}(\mathcal{H}/k)$. The nonzero multipoles of P_g are $\ell = 0, 2, 4$, whereas $P_{g\tilde{g}}$ has a nonzero dipole (as well as a smaller octupole). There are also further relativistic corrections to this dipole part of the cross power spectrum (Di Dio & Seljak, 2019).

A natural question is: what about the galaxy bispectrum? In the standard 'Newtonian' approximation, with only RSD, the galaxy bispectrum for a single tracer at fixed redshift has no dipole, and only has even multipoles (Scoccimarro et al., 1999; Nan et al., 2018). But with a lightcone corrected galaxy density contrast, the 3-point correlator, even for a *single* tracer, will no longer be an even function of $\boldsymbol{k}_a\cdot\boldsymbol{n}\,(a = 1,2,3)$. In order to compute the consequent contribution to the galaxy bispectrum, (4.1) is not sufficient: we need its second-order generalisation, $\delta_g \to \delta_g + \delta_g^{(2)}/2$.

4.2. Relativistic contributions to the galaxy bispectrum

At second order, the Doppler correction in (4.1) generalises to $A\,\boldsymbol{v}^{(2)}\cdot\boldsymbol{n}$, but there are also quadratic coupling terms. The couplings involve not only the Doppler effect, but also radial gradients of the potential ('gravitational redshift'), volume distortion effects, and second-order corrections to the density contrast. Most of these contributions are small, but those that scale as $(\mathcal{H}/k)\delta^2$ are not, even on equality scales. Except on super-equality scales we can often neglect any terms $\mathcal{O}((\mathcal{H}/k)^2)$ and higher, which makes the calculation considerably simpler. The treatment of higher-order terms is left to chapter 7.

The leading correction can be extracted from the general expressions that include all relativistic corrections to the Newtonian approximation, as given in Bertacca (2015) (see also Bertacca et al. (2014a); Yoo & Zaldarriaga (2014); Di Dio et al. (2014); Jolicoeur et al. (2017); Di Dio & Seljak (2019)),

$$\begin{aligned}\delta_{g\mathrm{D}}^{(2)} &= A\,\boldsymbol{v}^{(2)}\cdot\boldsymbol{n} + 2C(\boldsymbol{v}\cdot\boldsymbol{n})\delta + 2\frac{E}{\mathcal{H}}(\boldsymbol{v}\cdot\boldsymbol{n})\partial_r(\boldsymbol{v}\cdot\boldsymbol{n}) \\ &\quad + 2\frac{b_1}{\mathcal{H}}\phi\,\partial_r\delta + \frac{2}{\mathcal{H}^2}\big[\boldsymbol{v}\cdot\boldsymbol{n}\,\partial_r^2\phi - \phi\,\partial_r^2(\boldsymbol{v}\cdot\boldsymbol{n})\big] - \frac{2}{\mathcal{H}}\partial_r(\boldsymbol{v}\cdot\boldsymbol{v}),\end{aligned} \tag{4.4}$$

where ϕ is the gravitational potential, and the coefficients C and E are,

$$C = b_1(A+f) + b_1'/\mathcal{H} + 2(1-1/r\mathcal{H})\partial b_1/\partial\ln L\,, \tag{4.5}$$

and

$$E = 4 - 2A - \frac{3}{2}\Omega_m\,. \tag{4.6}$$

This is in agreement with the independent re-derivation of the leading correction given in Di Dio & Seljak (2019). We have corrected a typo in the last bracket of line 1 of Eq. (2.15): $-f_{\mathrm{evo}} \to -2f_{\mathrm{evo}} \equiv -2b_{\mathrm{e}}$. Note that our $\boldsymbol{n}$ is minus theirs, and they use the convention $\delta_g + \delta_g^{(2)}$. All but one of the contributions to this leading term contain Doppler contributions, so we label these terms with a D subscript. In this sense, they can be thought of as the relativistic correction to redshift space distortions, but their origin is considerably more subtle than in the Newtonian picture (Bertacca et al., 2014a; Di Dio & Seljak, 2019). These relativistic corrections all arise as projections along the line of sight $\boldsymbol{n}$. It is this projection that is responsible for the dipole in the observed bispectrum. Beyond these leading terms in (4.4) there are a host of local coupled terms which appear on larger scales.

We follow most work on the Fourier bispectrum and neglect the effect of lensing magnification. This is reasonable for correlations at the same redshift and when using very thin redshift bins allowed by spectroscopic surveys (Di Dio et al., 2019). We also use the standard plane-parallel approximation, which is reasonable on ultra-large scales. However, we note that wide-angle effects in the power spectrum can be of the same order of magnitude as the Doppler-type effects in certain circumstances (Tansella et al., 2018), and these should be incorporated in a more complete treatment.

The galaxy bispectrum is defined in Fourier space by,

$$\begin{aligned} B_g(\boldsymbol{k}_1, \boldsymbol{k}_2, \boldsymbol{k}_3) = \mathcal{K}(\boldsymbol{k}_1)\mathcal{K}(\boldsymbol{k}_2)\mathcal{K}^{(2)}(\boldsymbol{k}_1, \boldsymbol{k}_2, \boldsymbol{k}_3)P(k_1)P(k_2) \\ + 2 \text{ cyclic permutations}\,. \end{aligned} \tag{4.7}$$

The first-order kernel $\mathcal{K} = \mathcal{K}_{\rm N} + \mathcal{K}_{\rm D}$ is given by the term in brackets in (4.2). At second order, $\mathcal{K}^{(2)} = \mathcal{K}_{\rm N}^{(2)} + \mathcal{K}_{\rm D}^{(2)}$, where the Newtonian kernel is (Verde et al., 1998)

$$\begin{aligned} \mathcal{K}_{\rm N}^{(2)}(\boldsymbol{k}_1, \boldsymbol{k}_2, \boldsymbol{k}_3) = b_2 + b_1 F_2(\boldsymbol{k}_1, \boldsymbol{k}_2) + b_s S_2(\boldsymbol{k}_1, \boldsymbol{k}_2) \\ + f\mu_3^2 G_2(\boldsymbol{k}_1, \boldsymbol{k}_2) + \mathcal{Z}_2(\boldsymbol{k}_1, \boldsymbol{k}_2)\,. \end{aligned} \tag{4.8}$$

Here $F_2(\boldsymbol{k}_1, \boldsymbol{k}_2)$ is the standard Newtonian mode-coupling kernel for ΛCDM (Villa & Rampf, 2016),

$$F_2(a, \boldsymbol{k}_1, \boldsymbol{k}_2) = 1 + \frac{F(a)}{D(a)^2} + \left(\frac{k_1}{k_2} + \frac{k_2}{k_1}\right) \hat{\boldsymbol{k}}_1 \cdot \hat{\boldsymbol{k}}_2 + \left[1 - \frac{F(a)}{D(a)^2}\right] \left(\hat{\boldsymbol{k}}_1 \cdot \hat{\boldsymbol{k}}_2\right)^2\,, \tag{4.9}$$

where F is the second-order growth factor. For ΛCDM, the Einstein-De Sitter relation $F/D^2 = 3/7$ is a very good approximation. Using this approximation, F_2 is essentially time-independent. $G_2(\boldsymbol{k}_1, \boldsymbol{k}_2, \boldsymbol{k}_3)$ is the second-order velocity kernel,

$$G_2(a, \boldsymbol{k}_1, \boldsymbol{k}_2) = \frac{F'(a)}{D(a)D'(a)} + \left(\frac{k_1}{k_2} + \frac{k_2}{k_1}\right) \hat{\boldsymbol{k}}_1 \cdot \hat{\boldsymbol{k}}_2 + \left(2 - \frac{F'(a)}{D(a)D'(a)}\right) \left(\hat{\boldsymbol{k}}_1 \cdot \hat{\boldsymbol{k}}_2\right)^2\,, \tag{4.10}$$

where, since we use the Einstein-De Sitter approximation $F/D^2 = 3/7$ in F_2, we have $F'/(DD') = 6/7$ in G_2. We use a local bias model (Desjacques et al., 2018), which includes tidal bias kernel

$$S_2(\boldsymbol{k}_1, \boldsymbol{k}_2) = (\hat{\boldsymbol{k}}_1 \cdot \hat{\boldsymbol{k}}_2)^2 - \frac{1}{3}\,, \tag{4.11}$$

with tidal bias b_s. Finally, the kernel $\mathcal{Z}_2(\boldsymbol{k}_1, \boldsymbol{k}_2)$ incorporates the non-linear Kaiser RSD contribution (Verde et al., 1998; Scoccimarro et al., 1999),

$$\mathcal{Z}_2(\boldsymbol{k}_1, \boldsymbol{k}_2) = b_1 f(\mu_1 k_1 + \mu_2 k_2)\left(\frac{\mu_1}{k_1} + \frac{\mu_2}{k_2}\right) + f^2 \frac{\mu_1 \mu_2}{k_1 k_2}\left(\mu_1 k_1 + \mu_2 k_2\right)^2 . \tag{4.12}$$

The Doppler correction to (4.8) in Fourier space follows from (4.4) (Jolicoeur et al., 2018),

$$\begin{aligned}\mathcal{K}_{\mathrm{D}}^{(2)}(\boldsymbol{k}_1, \boldsymbol{k}_2, \boldsymbol{k}_3) = \mathrm{i}\,\mathcal{H}\Bigg[&-\frac{3}{2}\left(\mu_1 \frac{k_1}{k_2^2} + \mu_2 \frac{k_2}{k_1^2}\right)\Omega_m b_1 + 2\mu_{12}\left(\frac{\mu_1}{k_2} + \frac{\mu_2}{k_1}\right) f^2 \\ &\left(\frac{\mu_1}{k_1} + \frac{\mu_2}{k_2}\right) C f - \frac{3}{2}\left(\mu_1^3 \frac{k_1}{k_2^2} + \mu_2^3 \frac{k_2}{k_1^2}\right)\Omega_m f \\ &+\mu_1 \mu_2\left(\frac{\mu_1}{k_2} + \frac{\mu_2}{k_1}\right)\left(\frac{3}{2}\Omega_m - E f\right) f + \frac{\mu_3}{k_3} G_2(\boldsymbol{k}_1, \boldsymbol{k}_2, \boldsymbol{k}_3) A f\Bigg] ,\end{aligned} \tag{4.13}$$

where $\mu_{ab} = \hat{\boldsymbol{k}}_a \cdot \hat{\boldsymbol{k}}_b$ and $\mu_a = \hat{\boldsymbol{k}}_a \cdot \boldsymbol{n}$. The Newtonian kernel (4.8) scales as $(\mathcal{H}/k)^0$, while the Doppler kernel (4.13) scales as $(\mathcal{H}/k)$. Using (4.8) and (4.13) in (4.7), and dropping terms that scale as $(\mathcal{H}/k)^2$ and $(\mathcal{H}/k)^3$, we find that

$$\begin{aligned}B_{g\mathrm{N}}(\boldsymbol{k}_1, \boldsymbol{k}_2, \boldsymbol{k}_3) &= \mathcal{K}_{\mathrm{N}}(\boldsymbol{k}_1)\mathcal{K}_{\mathrm{N}}(\boldsymbol{k}_2)\mathcal{K}_{\mathrm{N}}^{(2)}(\boldsymbol{k}_1, \boldsymbol{k}_2, \boldsymbol{k}_3)\, P(k_1) P(k_2) \\ &\quad + 2 \text{ cyclic permutations}, \qquad (4.14) \\ B_{g\mathrm{D}}(\boldsymbol{k}_1, \boldsymbol{k}_2, \boldsymbol{k}_3) &= \Big\{\mathcal{K}_{\mathrm{N}}(\boldsymbol{k}_1)\mathcal{K}_{\mathrm{N}}(\boldsymbol{k}_2)\mathcal{K}_{\mathrm{D}}^{(2)}(\boldsymbol{k}_1, \boldsymbol{k}_2, \boldsymbol{k}_3) \\ &\quad + \left[\mathcal{K}_{\mathrm{N}}(\boldsymbol{k}_1)\mathcal{K}_{\mathrm{D}}(\boldsymbol{k}_2) + \mathcal{K}_{\mathrm{D}}(\boldsymbol{k}_1)\mathcal{K}_{\mathrm{N}}(\boldsymbol{k}_2)\right]\mathcal{K}_{\mathrm{N}}^{(2)}(\boldsymbol{k}_1, \boldsymbol{k}_2, \boldsymbol{k}_3)\Big\}\, P(k_1) P(k_2) \\ &\quad + 2 \text{ cyclic permutations}. \qquad (4.15)\end{aligned}$$

Since (4.13) scales as $\mathcal{H}/k$ it is purely imaginary, as all these contributions have at least one $\boldsymbol{k}$ projected along the line of sight – i.e., they contain odd powers of μ_a's. This means that *the leading relativistic correction in the observed galaxy Fourier bispectrum of a single tracer is a purely imaginary addition to the Newtonian approximation.* On larger scales, terms $\mathcal{O}((\mathcal{H}/k)^2)$ and higher appear in both the real and imaginary parts, with the kernels given in Umeh et al. (2017); Jolicoeur et al. (2017, 2018, 2019). We include the higher-order terms in our plots below, and a full treatment can be found in chapter 7.

4.3. Extracting the dipole

The bispectrum can be considered as a function of $k_1, k_2, k_3, \mu_1, \mu_2, \mu_3$ and φ, which is the azimuthal angle giving the orientation of the triangle relative to $\boldsymbol{n}$. In order to extract the dipole it is easiest to write $\mu_3 = -(k_1\mu_1 + k_2\mu_2)/k_3$, so that we can write $B_g = \sum_{i,j} \mathcal{B}_{ij}(\mathrm{i}\,\mu_1)^i(\mathrm{i}\,\mu_2)^j$, where $i, j = 0 \ldots 6$ which factors out the angular dependence multiplying real coefficients $\mathcal{B}_{ij}$ with no angular dependence. Then, use the identity $\mu_2 = \mu_1 \cos\theta + \sqrt{1-\mu_1^2}\,\sin\theta\,\cos\varphi$, where $\theta = \theta_{12}$ (and we define $\mu = \cos\theta$ – note that θ is the angle outside the triangle as the $\boldsymbol{k}_a$'s are head-to-tail). We use standard orthonormal spherical harmonics with the triangle lying in the $y-z$ plane, with $\boldsymbol{k}_1$ aligned along the z-axis (Nan et al., 2018), see Figure 4.1 for a schematic overview of the relevant angles and vectors of our decomposition. Then

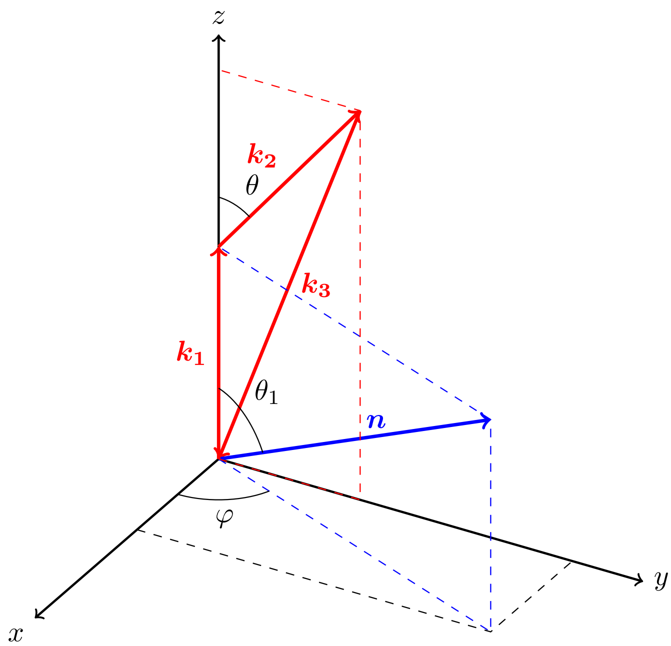

Figure 4.1.: Overview of the relevant vectors and angles for the Fourier-space bispectrum.

we have $Y_{\ell m}(\mu_1, \varphi)$, so that we can write $B_g = \sum_{\ell m} B_{\ell m} Y_{\ell m}(\mu_1, \varphi)$. The leading relativistic terms we consider here generate odd-power multipoles up to $\ell = 7$, and the full expression generates even and odd multipoles up to $\ell = 8$– see Chapter 7.

Different powers of $(\mathrm{i}\,\mu_1)$ and $(\mathrm{i}\,\mu_2)$ contribute to the dipole as follows,

$$\int \mathrm{d}\Omega(\mathrm{i}\,\mu_1)^a(\mathrm{i}\,\mu_2)^b Y^*_{1m} = \delta_{m,0}\frac{\mathrm{i}\sqrt{3\pi}}{15}\begin{bmatrix} 0 & 10\mu & 0 & -6\mu & \\ 10 & 0 & -4\mu^2-2 & 0 & \cdots \\ 0 & -6\,\mu & 0 & \frac{12\mu^3+18\mu}{7} & \\ -6 & 0 & \frac{24\,\mu^2+6}{7} & 0 & \\ & \vdots & & & \ddots \end{bmatrix}$$
$$+\,\delta_{m,\pm1}\frac{\sqrt{6\pi}}{15}\begin{bmatrix} 0 & -5 & 0 & 3 & \\ 0 & 0 & 2\,\mu & 0 & \cdots \\ 0 & 1 & 0 & -\frac{6\mu^2+3}{7} & \\ 0 & 0 & -\frac{6}{7}\,\mu & 0 & \\ & \vdots & & & \ddots \end{bmatrix}\sin\theta\,, \qquad (4.16)$$

where each matrix element corresponds to a particular combination of a, b, where the matrix indices run over the values $a = 0\ldots6, b = 0\ldots6$, with powers above 3 not written above; these are polynomials in μ up to order 6. From this we can read off the terms from $\mathcal{K}_{\mathrm{D}}$ contribute to differing $m = 0, \pm1$. In particular, if $i + j$ is even – i.e., the real part of the bispectrum – there is no contribution: only the imaginary terms, corresponding to $i + j$ odd, contribute. For the monopole, only $i + j$ even contribute. Therefore, at $\mathcal{O}(\mathcal{H}/k)$, *the monopole of the bispectrum is the Newtonian part, while the dipole is purely from the relativistic corrections. The presence of the dipole is therefore a 'smoking gun' signal for the leading relativistic correction to the bispectrum.* At order $\mathcal{O}((\mathcal{H}/k)^2)$, relativistic terms appear in the monopole, which were considered in Umeh et al. (2017); Jolicoeur et al. (2017, 2018, 2019).

4.4. Squeezed, equilateral and flattened limits

It is relatively straightforward to understand the type of dipole generated in different triangular configurations in our conventions. In particular, for the $\mathcal{O}(\mathcal{H}/k)$ relativistic dipole:

- The squeezed case is zero for $m = 0$, and is non-zero for $m = \pm1$. We see this directly from (4.16): with $\mu = -1$ the $m = 0$ contribution is anti-symmetric in i, j while $\mathcal{B}_{ij}$ is symmetric in this limit.

- In the equilateral case, the dipole is zero (this is the case for all orders in $\mathcal{H}/k$).
- The flattened case ($k_1 = k_2 = k_3/2, \theta = 0$) is zero for $m = \pm 1$ (for all orders in $\mathcal{H}/k$), but is non-zero for $m = 0$. This can be seen directly from (4.16) with $\theta = 0$.

To show the equilateral case is zero is a lengthy calculation involving many cancellations. Let us illustrate instead the squeezed case. We write $k_1 = k_2 = \sqrt{1+\varepsilon^2}k_S, k_3 = 2\varepsilon k_S$. In this case the triangle has small angle 2ε and equal angles $\pi/2 - \varepsilon$, where the squeezed limit is $\varepsilon \to 0$. It is convenient to replace $(1,2,3)$ by $(S,-S,L)$. Then to $O(\varepsilon)$, $k_{-S} = k_S\,, \quad k_L = 2\varepsilon k_S\,, \quad \mu_{-S} = -\mu_S - 2\varepsilon\mu_L\,, \mu_L = -\sqrt{1-\mu_S^2}\cos\varphi - \varepsilon\mu_S\,.$ In this limit, the permutations of the relativistic kernels become

$$\begin{aligned}\mathcal{K}_{\rm D}^{(2)}(\boldsymbol{k}_L, \boldsymbol{k}_S, \boldsymbol{k}_{-S}) = \mathrm{i}\,\mathcal{H}\bigg[& -\frac{3}{2}\Omega_m b_1 \mu_S \frac{k_S}{k_L^2} + Cf\frac{\mu_L}{k_L} \\ & -\frac{3}{2}\Omega_m f\mu_S^3\frac{k_S}{k_L^2} + \Big(\frac{3}{2}\Omega_m - Ef\Big) f\mu_S^2\frac{\mu_L}{k_L}\bigg]\end{aligned} \tag{4.17}$$

and $\mathcal{K}_{\rm D}^{(2)}(\boldsymbol{k}_{-S}, \boldsymbol{k}_L, \boldsymbol{k}_S) = \mathcal{K}_{\rm D}^{(2)}(\boldsymbol{k}_L, \boldsymbol{k}_S, \boldsymbol{k}_{-S})\big|_{\mu_S \to \mu_{-S}}$ while $\mathcal{K}_{\rm D}^{(2)}(\boldsymbol{k}_S, \boldsymbol{k}_{-S}, \boldsymbol{k}_L) = 0$. In the squeezed limit of the cyclic sum (4.7), the terms $\mathcal{K}^{(2)}(\boldsymbol{k}_L, \boldsymbol{k}_S, \boldsymbol{k}_{-S})$ and $\mathcal{K}^{(2)}(\boldsymbol{k}_{-S}, \boldsymbol{k}_L, \boldsymbol{k}_S)$ appear only in the form $\mathcal{K}^{(2)}(\boldsymbol{k}_L, \boldsymbol{k}_S, \boldsymbol{k}_{-S}) + \mathcal{K}^{(2)}(\boldsymbol{k}_{-S}, \boldsymbol{k}_L, \boldsymbol{k}_S)$. This sum regularises the divergent $k_S/k_L = (2\varepsilon)^{-1}$ and $k_S/k_L^2 = (2\varepsilon k_L)^{-1}$ terms. We obtain the bispectrum in the squeezed limit,

$$\begin{aligned}B_g^{\rm sq} = b_{1S}b_{1L}b_{SL}\,P_L P_S + \mathrm{i}\, b_{1S}\Big\{ & b_{SL} f A + \frac{3}{2}\Omega_m b_{1S} b_{1L} \\ & + 2b_{1L} f C + b_{1L}\mu_S^2\Big[\frac{3}{2}\Omega_m - Ef\Big]\Big\} P_L P_S\,\mu_L \frac{\mathcal{H}}{k_L}\,,\end{aligned} \tag{4.18}$$

where $P_{S,L} = P(k_{S,L})$, $b_{1S,L} \equiv b_1 + f\mu_{S,L}^2$ and

$$b_{SL} \equiv 2b_2 + \frac{43}{21}b_1 - \frac{4}{21} + \Big(2b_1 + \frac{5}{7}\Big) f\mu_S^2 + f\mu_L^2 b_{1S}\,.$$

Note that only the first term in the squeezed bispectrum comes from the Newtonian limit.

The type of dipole extracted from this term is seen as follows. To this order we can write $\mu_S^2 = \mu_S\mu_{-S}$. Then, since $\mu_L = -2(\mu_S + \mu_{-S})/\varepsilon$, we see that the $m = 0$ term

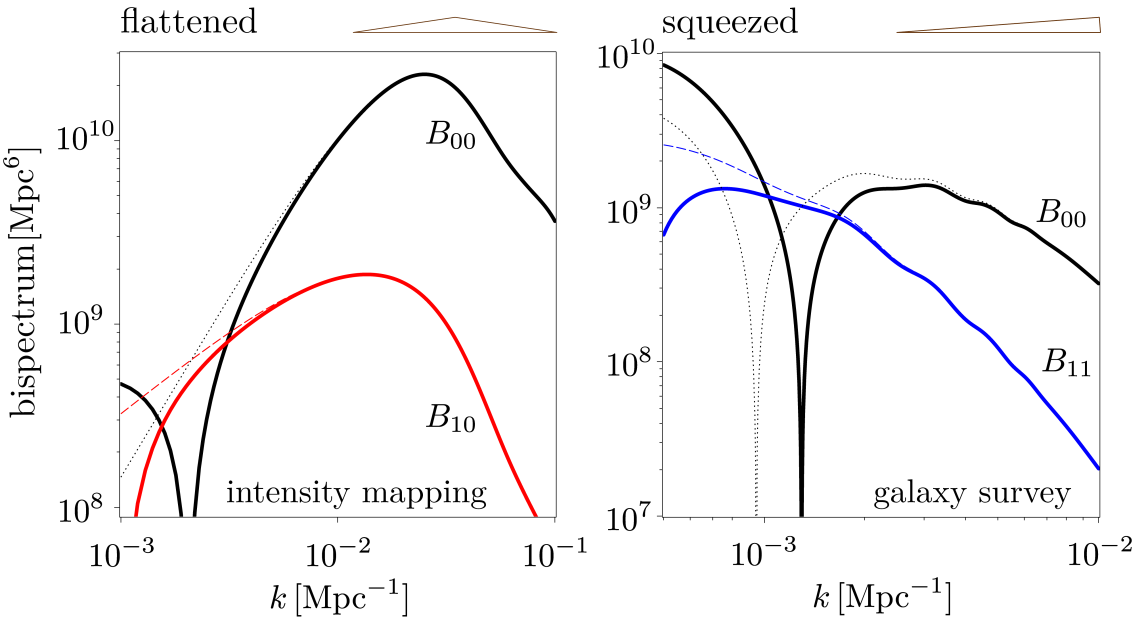

Figure 4.2.: The absolute value of the bispectrum dipole at $z = 1$ as a function of triangle size, in the flattened (Left, $\theta = 2°$, for intensity mapping bias) and squeezed (Right, $\theta = 178°$, for Euclid-like bias) configurations, with k_3 as the horizontal axis. Red is the $m = 0$ part and blue is $m = \pm1$. Dashed (and dotted) lines show up to the $\mathcal{O}(\mathcal{H}/k)$ terms considered analytically here, while solid lines indicate larger-scale contributions. For reference the monopole is in black, with the dotted line the Newtonian part. (The zero-crossing in the monopole for the squeezed case is a result of the tidal bias.)

is zero because $B^{\rm sq}_{g\rm D}$ is symmetric in $\mu^i_S\mu^j_{-S}$ under $i \leftrightarrow j$, while the $m = 0$ term is antisymmetric in (4.16). This leaves just the $m = \pm1$ contribution in (4.16).

4.5. The dipole in intensity mapping and galaxy surveys

We now consider the amplitude of the dipole relevant for upcoming galaxy surveys, which have different bias parameters. We consider two different types of survey: an SKA intensity mapping of 21 cm radio emission, as well as a Euclid-like optical/infrared spectroscopic survey. An intensity map of the 21cm emission of neutral hydrogen (HI) in the post-reionization Universe records the total emission in galaxies containing HI, without detecting individual galaxies. There

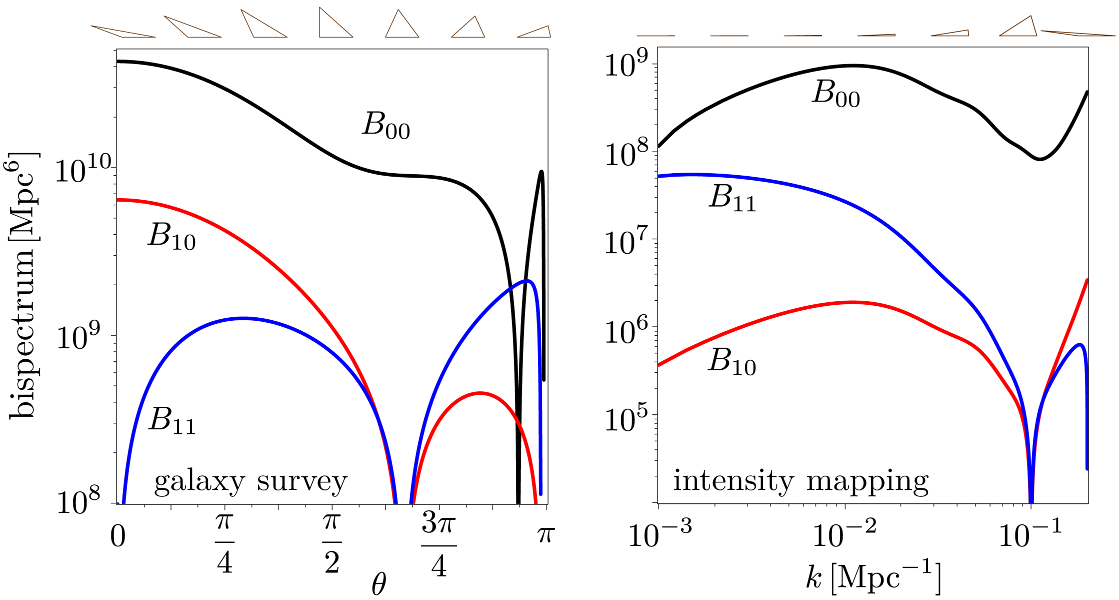

Figure 4.3.: (Left) We show the dipoles as a function of θ with a bias appropriate for a Euclid-like survey, for $k_1 = k_2 = 0.01\,\text{Mpc}^{-1}$. The left of the plot corresponds to the flattened case where the $m = 0$ (red) dipole reaches 10% of the monopole. (Right) We show the IM signal with $k_1 = k_2 = 0.1\,\text{Mpc}^{-1}$ versus the long mode k_3. Except for very long modes $\theta \approx \pi$, our $\mathcal{O}(\mathcal{H}/k)$ truncation is a very good approximation in these examples.

is an equivalence between the brightness temperature contrast and number count contrast (Umeh et al., 2016). For IM we use the bias parameters at $z = 1$, $b_1 = 0.856, b_2 = -0.321, b_1' = -0.5 \times 10^{-4}, b_e = -0.5, b_e' = 0, s = 2/5$ (Fonseca et al., 2018; Umeh et al., 2016) while for the spectroscopic survey we use $b_1 = 1.3, b_2 = -0.74, b_1' = -1.6 \times 10^{-4}, b_e = -4, b_e' = 0, s = -0.95$ (Camera et al., 2018; Yankelevich & Porciani, 2019). For intensity mapping, $\partial b_1/\partial lnL = 0$ and we assume it is zero for simplicity for the spectroscopic survey. We use a LCDM model with standard parameters $\Omega_m = 0.314, h = 0.67, f_{\rm baryon} = 0.157, n_s = 0.968$. Plots are presented using linear power spectra generated using CAMB (Lewis et al., 2000).

In Fig. (4.2) we show how changing the scale of a fixed triangle changes the amplitude of the dipole, with reference to the monopole. In the flattened case with $m = 0$ we see the signal peaks for triangles below the equality scale, while for squeezed shapes, with $m = \pm 1$, the signal is smaller, and peaks when the long mode approaches the Hubble scale. In Fig. (4.3) we change the shape with fixed $k_1 = k_2$ for both galaxy and IM surveys. We confirm our analytical results that the equilateral limit is zero, as well as the other limits. For triangles between right-angle and flattened the dipole is more than 10% of the monopole, and the signal is largest in the flattened case – except in the extreme squeezed limit (not shown).

4.6. Conclusions

We have shown for the first time that the relativistic galaxy bispectrum has a leading correction which is a local dipole with respect to the observers line of sight. In contrast to the power spectrum, this dipole exists even for a single tracer. We have shown analytically how the dipole is generated for the leading terms, and numerically we have included all local contributions, which show up above the equality scale. We have neglected integrated terms which will also contribute to the dipole, but their inclusion in a Fourier space bispectrum is non-trivial. Local relativistic corrections will induce all multipoles up to $\ell = 8$ at every m, in contrast to the Newtonian case which only induces even $\ell = 0, 2, 4$. We will investigate these new multipoles in a forthcoming publication.

We have shown that this dipole is large with respect to the monopole in both the flattened and squeezed limits, which excite different orders of the dipole orientation m. We have shown that even on equality scales it is about 10% of the monopole at

$z = 1$ for flattened shapes which have the largest amplitude. In more squeezed cases where the short mode is $\sim 10\,\mathrm{Mpc}$ the dipole can also be a large part of the IM signal. Furthermore, although we have only considered Gaussian initial conditions here, the dipole will be unaffected by non-Gaussianity at leading order because these corrections start at $\mathcal{O}((\mathcal{H}/k)^2)$, making our predictions relatively robust to this. This implies that the dipole of the bispectrum is a unique signature of general relativity on cosmological scales, and therefore offers a new observational window onto modifications of general relativity.

5. Detectability in next-generation galaxy surveys

The Fourier galaxy bispectrum is complex, with the imaginary part arising from leading-order relativistic corrections, due to Doppler, gravitational redshift and related line-of-sight effects in redshift space. The detection of the imaginary part of the bispectrum is potentially a smoking gun signal of relativistic contributions. Long-mode relativistic effects couple to short-mode Newtonian effects in the galaxy bispectrum, but not in the galaxy power spectrum. This is the basis for detectability of relativistic effects in the bispectrum of a single galaxy survey, whereas the power spectrum requires multiple galaxy surveys to detect the corresponding signal.

In this chapter, we investigate whether the next generation of high-precision cosmological surveys will be able to make such a detection. First, we consider a Stage IV spectroscopic $H\alpha$ survey similar to Euclid, and we find that the cumulative signal to noise of this relativistic signature is $\mathcal{O}(10)$. Secondly, we look at some future 21cm intensity mapping surveys; MeerKAT, SKA, PUMA, and HIRAX. Due to foreground and telescope beam effects, the signal-to-noise ratio for intensity mapping surveys is typically lower than for spectroscopic $H\alpha$ surveys, though also still detectable.

5.1. Introduction

The bispectrum of number count fluctuations in redshift space will become an increasingly important complement to the power spectrum in the extraction of cosmological information from galaxy surveys, in the measurement of clustering bias parameters and in the breaking of degeneracies between the clustering amplitude and growth rate. Analysis of the Fourier galaxy bispectrum is already well advanced for existing survey data (e.g Gil-Marín et al. (2017); Sugiyama et al. (2018)) and for mock data of future surveys (e.g. Karagiannis et al. (2018); Yankelevich & Porciani (2019); Oddo et al. (2020); Sugiyama et al. (2020)).

Here we highlight a feature of the tree-level Fourier galaxy bispectrum which follows from the leading-order relativistic contribution – due to Doppler, gravitational redshift and related line-of-sight effects – that is omitted in the standard Newtonian analysis. These effects generate an imaginary part of the galaxy bispectrum, which can be understood as follows (see also McDonald (2009); Clarkson et al. (2019); Jeong & Schmidt (2020) for a more general discussion). The Doppler-type contributions to the galaxy density contrast involve one or three derivatives of scalars along the fixed line of sight $\boldsymbol{n}$ [see (5.6), (5.7) below]. In Fourier space, with the plane-parallel approximation, we have $\boldsymbol{n}\cdot\boldsymbol{\nabla} \to \mathrm{i}\ \boldsymbol{n}\cdot\boldsymbol{k}$, and this leads to imaginary corrections to the galaxy density contrast, which do not cancel in the bispectrum, unlike in the power spectrum. At first order, we have $\delta_g = \delta_{g\mathrm{N}} + \delta_{g\mathrm{D}}$, where the Newtonian part $\delta_{g\mathrm{N}}$ is real and scales as the linear matter density contrast δ. The relativistic Doppler-type part $\delta_{g\mathrm{D}}$ scales as $\mathrm{i}\,(\mathcal{H}/k)\delta$ (see McDonald (2009); Jeong et al. (2012); Abramo & Bertacca (2017); Clarkson et al. (2019) and below). At second order, the relativistic contribution $\delta^{(2)}_{g\mathrm{D}}$ scales as $\mathrm{i}\,(\mathcal{H}/k)(\delta)^2$ (see Clarkson et al. (2019) and below).

In the case of the galaxy auto-power spectrum, $P_g \sim \langle|\delta_g|^2\rangle$, the relativistic part is real and scales as $(\mathcal{H}/k)^2P$: therefore we can neglect $P_{g\mathrm{D}}$ at leading order. By contrast, for the galaxy bispectrum, $B_g \sim \langle\delta_g\,\delta_g\,\delta_g^{(2)}\rangle$, a coupling of relativistic contributions to short-scale Newtonian terms (which is absent in P_g) produces a $B_{g\mathrm{D}}$ that is imaginary and scales as $\mathrm{i}\,(\mathcal{H}/k)P^2$. We therefore expect these relativistic effects to be more accessible in the bispectrum than in the power spectrum, for the case of a single tracer of the matter distribution.

Although the galaxy bispectrum is statistically isotropic, the plane-parallel approximation in redshift space breaks 3-dimensional isotropy, since a preferred direction is imposed by the observer's fixed line of sight.

Let us introduce a more explicit analysis, as follows.

At tree-level, the Fourier galaxy bispectrum at a redshift z is given by

$$\Big\langle\delta_g(z,\boldsymbol{k}_1)\delta_g(z,\boldsymbol{k}_2)\delta_g^{(2)}(z,\boldsymbol{k}_3)\Big\rangle + 2\ \mathrm{cp} = 2(2\pi)^3B_g(z,\boldsymbol{k}_1,\boldsymbol{k}_2,\boldsymbol{k}_3)\delta^{\mathrm{Dirac}}\big(\boldsymbol{k}_1+\boldsymbol{k}_2+\boldsymbol{k}_3\big)\,, \tag{5.1}$$

where cp denotes cyclic permutation and the factor 2 on the right arises from the convention that the total number density contrast is $\delta_g + \delta_g^{(2)}/2$. In terms of the first- and second-order kernels, we have

$$B_g(z, \boldsymbol{k}_1, \boldsymbol{k}_2, \boldsymbol{k}_3) = \mathcal{K}^{(1)}(z, \boldsymbol{k}_1)\mathcal{K}^{(1)}(z, \boldsymbol{k}_2)\mathcal{K}^{(2)}(z, \boldsymbol{k}_1, \boldsymbol{k}_2, \boldsymbol{k}_3)P(z, k_1)P(z, k_2) + 2\ \mathrm{cp}\,, \tag{5.2}$$

where P is the linear matter power spectrum. The $9 - 3 = 6$ degrees of freedom in the triangle condition $\boldsymbol{k}_1 + \boldsymbol{k}_2 + \boldsymbol{k}_3 = \boldsymbol{0}$ at each z are reduced to 5 by the fixed observer's line of sight direction $\boldsymbol{n}$. The bispectrum can be chosen at each z to be a function of the 3 magnitudes $k_a = \big(k_1, k_2, k_3\big)$ and 2 angles that define the orientation of the triangle (see Fig. 5.1):

$$B_g(z, \boldsymbol{k}_a) = B_g(z, k_a, \mu_1, \varphi)\,. \tag{5.3}$$

Here $\mu_a = \hat{\boldsymbol{k}}_a \cdot \boldsymbol{n} = \cos\theta_a$, and φ is the angle between the triangle plane and the $(\boldsymbol{n}, \boldsymbol{k}_1)$-plane. The three angles $\theta_{ab} = \cos^{-1}\big(\hat{\boldsymbol{k}}_a \cdot \hat{\boldsymbol{k}}_b\big)$, are determined by k_a; then $\mu_2 = \mu_1 \cos\theta_{12} + \sin\theta_1 \sin\theta_{12}\cos\varphi$ is determined when φ is given, and $\mu_3 = -(\mu_1 k_1 + \mu_2 k_2)/k_3$.

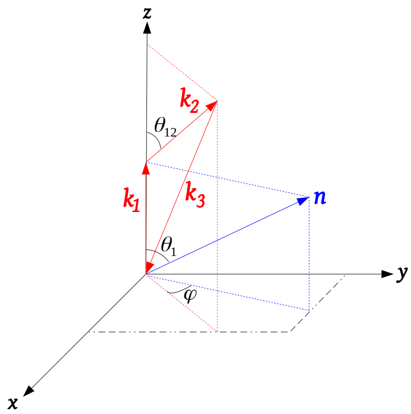

Figure 5.1.: Relevant vectors and angles for the Fourier bispectrum.

In the standard Newtonian approximation, $B_g = B_{g\mathrm{N}}$, the kernels in (5.2) contain the galaxy bias and the redshift-space distortions (RSD) at first and second order Bernardeau et al. (2002); Karagiannis et al. (2018):

$$\mathcal{K}^{(1)}_{\mathrm{N}}(\boldsymbol{k}_1) = b_1 + f\mu_1^2\,, \tag{5.4}$$

$$\mathcal{K}^{(2)}_{\mathrm{N}}(\boldsymbol{k}_1, \boldsymbol{k}_2, \boldsymbol{k}_3) = b_1 F_2(\boldsymbol{k}_1, \boldsymbol{k}_2) + b_2 + f\mu_3^2 G_2(\boldsymbol{k}_1, \boldsymbol{k}_2) + fZ_2(\boldsymbol{k}_1, \boldsymbol{k}_2) + b_{s^2} S_2(\boldsymbol{k}_1, \boldsymbol{k}_2), \tag{5.5}$$

where we dropped the z-dependence for brevity. Here f is the linear matter growth rate, b_1, b_2 are the linear and second-order clustering biases, and b_{s^2} is the tidal bias. The kernel F_2 is for second-order density, $G_2, \mathcal{Z}_2$ are for RSD, and S_2 is the kernel for tidal bias (see Appendix G for the full expressions).

The Doppler-type relativistic corrections to the Newtonian number count contrast in redshift space are given at first order by Bonvin & Durrer (2011):

$$\delta_{g\mathrm{D}} = A\, \boldsymbol{v}\cdot\boldsymbol{n}\,, \tag{5.6}$$

where $A(z)$ is given below in (5.12) and the momentum conservation equation has been used to eliminate the gravitational redshift: $\boldsymbol{n}\cdot\boldsymbol{\nabla}\Phi \equiv \partial_r\Phi = -\boldsymbol{v}'\cdot\boldsymbol{n} - \mathcal{H}\,\boldsymbol{v}\cdot\boldsymbol{n}$. Here Φ is the gravitational potential, $\boldsymbol{v}$ is the peculiar velocity, $\mathcal{H}$ is the comoving Hubble parameter, and r is the line-of-sight comoving distance. Note that $\boldsymbol{v}\cdot\boldsymbol{n} = \partial_r V$, where V is the velocity potential ($v_i = \partial_i V$). At second order, and neglecting vector and tensor modes, it is shown in Clarkson et al. (2019) that (see also Di Dio & Seljak (2019))

$$\begin{aligned}\delta^{(2)}_{g\mathrm{D}} &= A\,\boldsymbol{v}^{(2)}\!\cdot\boldsymbol{n} + 2C(\boldsymbol{v}\cdot\boldsymbol{n})\,\delta + 2\frac{E}{\mathcal{H}}(\boldsymbol{v}\cdot\boldsymbol{n})\,\partial_r(\boldsymbol{v}\cdot\boldsymbol{n}) + \frac{2}{\mathcal{H}^2}\big[(\boldsymbol{v}\cdot\boldsymbol{n})\,\partial_r^2\Phi - \Phi\,\partial_r^2(\boldsymbol{v}\cdot\boldsymbol{n})\big]\\ &\quad - \frac{2}{\mathcal{H}}\,\partial_r(\boldsymbol{v}\cdot\boldsymbol{v}) + 2\frac{b_1}{\mathcal{H}}\,\Phi\,\partial_r\delta\,.\end{aligned} \tag{5.7}$$

The redshift-dependent coefficients C, E are given below in (5.13), (5.14).

In Fourier space, neglecting sub-leading $\mathcal{O}(\mathcal{H}^2/k^2)$ terms, we find from (5.2) that

$$\begin{aligned}B_{g\mathrm{D}}(\boldsymbol{k}_1,\boldsymbol{k}_2,\boldsymbol{k}_3) = \bigg\{&\Big[\mathcal{K}^{(1)}_{\mathrm{N}}(\boldsymbol{k}_1)\mathcal{K}^{(1)}_{\mathrm{D}}(\boldsymbol{k}_2) + \mathcal{K}^{(1)}_{\mathrm{D}}(\boldsymbol{k}_1)\mathcal{K}^{(1)}_{\mathrm{N}}(\boldsymbol{k}_2)\Big]\mathcal{K}^{(2)}_{\mathrm{N}}(\boldsymbol{k}_1,\boldsymbol{k}_2,\boldsymbol{k}_3)\\ &+ \mathcal{K}^{(1)}_{\mathrm{N}}(\boldsymbol{k}_1)\mathcal{K}^{(1)}_{\mathrm{N}}(\boldsymbol{k}_2)\mathcal{K}^{(2)}_{\mathrm{D}}(\boldsymbol{k}_1,\boldsymbol{k}_2,\boldsymbol{k}_3)\bigg\}P(k_1)P(k_2) + 2\text{ cp.}\end{aligned} \tag{5.8}$$

The relativistic kernels follow from (5.6) and (5.7); they are given in Clarkson et al. (2019) as

$$\mathcal{K}^{(1)}_{\mathrm{D}}(\boldsymbol{k}_1) = \mathrm{i}\,\mathcal{H}fA\,\frac{\mu_1}{k_1}\,, \tag{5.9}$$

$$\begin{aligned}\mathcal{K}^{(2)}_{\mathrm{D}}(\boldsymbol{k}_1,\boldsymbol{k}_2,\boldsymbol{k}_3) &= \mathrm{i}\,\mathcal{H}f\bigg[A\,\frac{\mu_3}{k_3}G_2(\boldsymbol{k}_1,\boldsymbol{k}_2) + C\left(\frac{\mu_1}{k_1}+\frac{\mu_2}{k_2}\right) + \left(\frac{3}{2}\Omega_m - fE\right)\mu_1\mu_2\left(\frac{\mu_1}{k_2}+\frac{\mu_2}{k_1}\right)\\ &\quad - \frac{3}{2}\Omega_m\left(\mu_1^3\frac{k_1}{k_2^2}+\mu_2^3\frac{k_2}{k_1^2}\right) + 2f\,\hat{\boldsymbol{k}}_1\cdot\hat{\boldsymbol{k}}_2\left(\frac{\mu_1}{k_1}+\frac{\mu_2}{k_2}\right) - \frac{3\Omega_m b_1}{2f}\left(\mu_1\frac{k_1}{k_2^2}+\mu_2\frac{k_2}{k_1^2}\right)\bigg].\end{aligned} \tag{5.10}$$

It is clear from (5.8)–(5.10) and from the general expressions given in Umeh et al. (2017); Jolicoeur et al. (2017), that Doppler-type relativistic effects generate an imaginary correction to the Newtonian bispectrum:

$$\mathrm{Re}\, B_g = B_{g\mathrm{N}} + \mathcal{O}(\mathcal{H}^2/k^2)\,, \quad \mathrm{i}\;\mathrm{Im}\, B_g = B_{g\mathrm{D}} + \mathcal{O}(\mathcal{H}^3/k^3)\,. \tag{5.11}$$

The coefficients in (5.9) and (5.10) are Clarkson et al. (2019)

$$A = b_e - 2\mathcal{Q} + \frac{2(\mathcal{Q}-1)}{r\mathcal{H}} - \frac{\mathcal{H}'}{\mathcal{H}^2}\,, \tag{5.12}$$

$$C = b_1\big(A+f\big) + \frac{b_1'}{\mathcal{H}} + 2\left(1-\frac{1}{r\mathcal{H}}\right)\frac{\partial b_1}{\partial \ln L}\bigg|_{\mathrm{c}}\,, \tag{5.13}$$

$$E = 4 - 2A - \frac{3}{2}\Omega_m\,, \tag{5.14}$$

where a prime is a conformal time derivative, $\Omega_m = \Omega_{m0}(1+z)H_0^2/\mathcal{H}^2$, L is the luminosity, and $|_{\mathrm{c}}$ denotes evaluation at the flux cut.

In addition to the clustering bias b_1, the relativistic bispectrum is sensitive to the evolution bias and magnification bias, which are defined as Alonso et al. (2015)

$$b_e = -\frac{\partial \ln n_g}{\partial \ln(1+z)}\,, \quad \mathcal{Q} = -\frac{\partial \ln n_g}{\partial \ln L}\bigg|_{\mathrm{c}}\,. \tag{5.15}$$

Here and below, n_g is the *comoving* galaxy number density. (Note that the alternative magnification bias parameter $s = 2\mathcal{Q}/5$ is often used.)

It is interesting to note that the magnification bias $\mathcal{Q}$ enters the relativistic bispectrum, even though we have not included the effect of the integrated lensing magnification κ. The reason for this apparent inconsistency is that there is a (non-integrated) Doppler correction to κ at leading order Bonvin (2008); Bolejko et al. (2013).

5.2. Signal-to-Noise

The signal-to-noise ratio (SNR) for the bispectrum at some redshift z is in the Gaussian approximation of uncorrelated triangles given by (Scoccimarro et al., 2004),

$$\left[\frac{S}{N}(z)\right]^2 = \sum_{k_a,\,\mu_1,\,\varphi} \frac{1}{\mathrm{Var}[B_g(z,k_a,\mu_1,\varphi)]}\, B_g(z,k_a,\mu_1,\varphi)\, B_g^*(z,k_a,\mu_1,\varphi)\,, \tag{5.16}$$

where we have introduced the complex conjugate B_g^* as the galaxy bispectrum has an imaginary correction. Here $\mathrm{Var}[B_g]$ is the variance of the bispectrum estimator (Chan & Blot, 2017),

$$\hat{B}_g(z, \boldsymbol{k}_a) = \frac{k_\mathrm{f}^3}{V_{123}} \int_{\boldsymbol{k}_a} \mathrm{d}^3\boldsymbol{q}_1\, \mathrm{d}^3\boldsymbol{q}_2\, \mathrm{d}^3\boldsymbol{q}_3\, \delta^\mathrm{Dirac}(\boldsymbol{q}_1 + \boldsymbol{q}_2 + \boldsymbol{q}_3)\, \delta_g(z, \boldsymbol{q}_1)\delta_g(z, \boldsymbol{q}_2)\delta_g(z, \boldsymbol{q}_3)\,, \tag{5.17}$$

where integration is over the shells $k_a - \Delta k/2 \leq q_a \leq k_a + \Delta k/2$ and the shell volume is $V_{123} = \int_{\boldsymbol{k}_a} \mathrm{d}^3\boldsymbol{q}_1\, \mathrm{d}^3\boldsymbol{q}_2\, \mathrm{d}^3\boldsymbol{q}_3\, \delta^\mathrm{Dirac}(\boldsymbol{q}_1 + \boldsymbol{q}_2 + \boldsymbol{q}_3)$.

In the Newtonian approximation, the Gaussian variance can be given as (Scoccimarro et al., 2004; Karagiannis et al., 2018),

$$\mathrm{Var}[B_g(z, k_a, \mu_1, \varphi)] = s_B\, \frac{\pi k_\mathrm{f}(z)^3}{k_1 k_2 k_3 (\Delta k)^3}\, \frac{N_{\mu_1} N_\varphi}{\Delta\mu_1 \Delta\varphi}\, \tilde{P}_{g\mathrm{N}}(z, k_1, \mu_1)\tilde{P}_{g\mathrm{N}}(z, k_2, \mu_2)\tilde{P}_{g\mathrm{N}}(z, k_3, \mu_3)\,, \tag{5.18}$$

where,

$$\tilde{P}_{g\mathrm{N}}(z, k_a, \mu_a) = P_{g\mathrm{N}}(z, k_a, \mu_a) + \frac{1}{n_g(z)}\,, \tag{5.19}$$

and $P_{g\mathrm{N}} = (b_1 + f\mu_a^2)^2 P$ is the linear galaxy power spectrum. In (5.18), s_B is 6, 2, 1 respectively for equilateral, isosceles and non-isosceles triangles, and N_{μ_1}, N_φ are the ranges for μ_1, φ (which are sometimes reduced from their full values of 2 and 2π using symmetry arguments). The fundamental mode is determined by the comoving survey volume of the redshift bin centred at z, i.e. $k_\mathrm{f}(z) = 2\pi V(z)^{-1/3}$, where $V(z) = 4\pi f_\mathrm{sky}[r(z + \Delta z/2)^3 - r(z - \Delta z/2)^3]$.

6. Detectability in Spectroscopic Surveys

The Fourier galaxy bispectrum is complex, with the imaginary part arising from leading-order relativistic corrections, due to Doppler, gravitational redshift and related line-of-sight effects in redshift space. The detection of the imaginary part of the bispectrum is potentially a smoking gun signal of relativistic contributions. We investigate whether next-generation spectroscopic surveys could make such a detection. For a Stage IV spectroscopic $H\alpha$ survey similar to Euclid, we find that the cumulative signal to noise of this relativistic signature is $\mathcal{O}(10)$. Long-mode relativistic effects couple to short-mode Newtonian effects in the galaxy bispectrum, but not in the galaxy power spectrum. This is the basis for detectability of relativistic effects in the bispectrum of a single galaxy survey, whereas the power spectrum requires multiple galaxy surveys to detect the corresponding signal.

6.1. Introduction

6.2. Signal-to-Noise

The signal-to-noise ratio (SNR) for the bispectrum at redshift z is given in the Gaussian approximation of uncorrelated triangles by Scoccimarro et al. (2004)

$$\left[\frac{S}{N}(z)\right]^2 = \sum_{k_a,\,\mu_1,\,\varphi} \frac{1}{\mathrm{Var}[B_g(z,k_a,\mu_1,\varphi)]}\, B_g(z,k_a,\mu_1,\varphi)\, B_g^*(z,k_a,\mu_1,\varphi) \tag{6.1}$$

where we have introduced the complex conjugate B_g^* since the bispectrum has an imaginary correction. Here $\mathrm{Var}[B_g]$ is the variance of the bispectrum estimator Chan

& Blot (2017):

$$B_g(z,\boldsymbol{k}_a) = \frac{k_{\rm f}^3}{V_{123}} \int_{\boldsymbol{k}_a} {\rm d}^3\boldsymbol{q}_1\, {\rm d}^3\boldsymbol{q}_2\, {\rm d}^3\boldsymbol{q}_3\, \delta^{\rm Dirac}(\boldsymbol{q}_1+\boldsymbol{q}_2+\boldsymbol{q}_3)\, \delta_g(z,\boldsymbol{q}_1)\delta_g(z,\boldsymbol{q}_2)\delta_g(z,\boldsymbol{q}_3)\,, \tag{6.2}$$

where integration is over the shells $k_a - \Delta k/2 \le q_a \le k_a + \Delta k/2$ and the shell volume is $V_{123} = \int_{\boldsymbol{k}_a} {\rm d}^3\boldsymbol{q}_1\, {\rm d}^3\boldsymbol{q}_2\, {\rm d}^3\boldsymbol{q}_3\, \delta^{\rm Dirac}(\boldsymbol{q}_1+\boldsymbol{q}_2+\boldsymbol{q}_3)$.

In the Newtonian approximation, the Gaussian variance can be given as Scoccimarro et al. (2004); Karagiannis et al. (2018)

$${\rm Var}[B_g(z,k_a,\mu_1,\varphi)] = s_B\, \frac{\pi k_{\rm f}(z)^3}{k_1k_2k_3(\Delta k)^3}\, \frac{N_{\mu_1}N_\varphi}{\Delta\mu_1\Delta\varphi}\, \tilde{P}_{g{\rm N}}(z,k_1,\mu_1)\tilde{P}_{g{\rm N}}(z,k_2,\mu_2)\tilde{P}_{g{\rm N}}(z,k_3,\mu_3)\,, \tag{6.3}$$

where

$$\tilde{P}_{g{\rm N}}(z,k_a,\mu_a) = P_{g{\rm N}}(z,k_a,\mu_a) + \frac{1}{n_g(z)}\,, \tag{6.4}$$

and $P_{g{\rm N}} = (b_1 + f\mu_a^2)^2 P$ is the linear galaxy power spectrum. In (5.18), s_B is 6, 2, 1 respectively for equilateral, isosceles and non-isosceles triangles, and N_{μ_1}, N_φ are the ranges for μ_1, φ (which are sometimes reduced from their full values of 2 and 2π using symmetry arguments). The fundamental mode is determined by the comoving survey volume of the redshift bin centred at z, i.e., $k_{\rm f}(z) = 2\pi V(z)^{-1/3}$, where $V(z) = 4\pi f_{\rm sky}[r(z+\Delta z/2)^3 - r(z-\Delta z/2)^3]$.

For a survey with redshift bin centres ranging from $z_{\rm min}$ to $z_{\rm max}$, the cumulative SNR is

$$\frac{S}{N}(\le z) = \left\{ \sum_{z'=z_{\rm min}}^{z} \left[\frac{S}{N}(z')\right]^2 \right\}^{1/2}\,, \tag{6.5}$$

and then the total SNR is $S/N(\le z_{\rm max})$.

6.2.1. Relativistic contribution to the variance

For the full bispectrum, including the relativistic part, (5.17) leads to a variance of the form

$${\rm Var}[B_g(z,\boldsymbol{k}_a)] \propto \tilde{P}_g(z,k_1,\mu_1)\tilde{P}_g(z,k_2,\mu_2)\tilde{P}_g(z,k_3,\mu_3)\,. \tag{6.6}$$

In the Newtonian approximation, this gives (5.18). By (5.9), the galaxy number density contrast has an imaginary relativistic correction, $\delta_g = \delta_{g{\rm N}} + \delta_{g{\rm D}}$. However, since $P_g \sim \langle \delta_g(\boldsymbol{k})\delta_g(-\boldsymbol{k})\rangle = \langle |\delta_g(\boldsymbol{k})|^2\rangle$, the galaxy power spectrum is given by McDonald (2009); Abramo & Bertacca (2017); Clarkson et al. (2019)

$$P_g = P_{g\mathrm{N}} + P_{g\mathrm{D}} = P_{g\mathrm{N}} + \mathcal{O}(\mathcal{H}^2/k^2)\,. \tag{6.7}$$

It follows from (6.6) and (6.7) that at leading order, the relativistic contribution to the variance can be neglected:

$$\mathrm{Var}[B_g] = \mathrm{Var}[B_{g\mathrm{N}}] + \mathcal{O}(\mathcal{H}^2/k^2)\,. \tag{6.8}$$

Therefore the SNR for the Newtonian and relativistic parts of the bispectrum are

$$\left(\frac{S}{N}\right)^2_{\mathrm{N}} = \sum_{k_a,\,\mu_1,\,\varphi} \frac{B_{g\mathrm{N}}\,B_{g\mathrm{N}}}{\mathrm{Var}[B_{g\mathrm{N}}]}\,, \tag{6.9}$$

$$\left(\frac{S}{N}\right)^2_{\mathrm{D}} = \sum_{k_a,\,\mu_1,\,\varphi} \frac{B_{g\mathrm{D}}\,B^*_{g\mathrm{D}}}{\mathrm{Var}[B_{g\mathrm{N}}]}\,. \tag{6.10}$$

6.2.2. Nonlinear effects

In order to avoid nonlinear effects of matter clustering, the maximum k is chosen as a scale where perturbation theory for the matter density contrast begins to break down. It is known that the matter bispectrum is more sensitive to nonlinearity than the matter power spectrum: at $z \sim 0$ nonlinearity sets in at $k \sim 0.1h/\,\mathrm{Mpc}$ for the matter bispectrum, as opposed to $k \sim 0.2h/\,\mathrm{Mpc}$ for the matter power spectrum. To account for the growth of k_{max} with redshift, we use the redshift-dependence proposed in Smith et al. (2003) for the power spectrum, but with half the amplitude at $z = 0$:

$$k_{\mathrm{max}}(z) = 0.1h\big(1+z\big)^{2/(2+n_s)}\,. \tag{6.11}$$

The cut-off $k \le k_{\mathrm{max}}(z)$ avoids a breakdown of perturbative accuracy in the matter correlations, but nonlinearities in the galaxy correlations due to RSD can affect longer wavelength modes. The effect of RSD on these scales is to damp the power – the 'FoG' effect. In order to take account of this, we follow Karagiannis et al.

(2018); Yankelevich & Porciani (2019) and use the simple model of FoG damping,

$$P_g \to D_P\, P_g\,, \quad D_P(z,\boldsymbol{k}) = \exp\Big\{-frac12\big[k\mu\,\sigma(z)\big]^2\Big\}\,, \tag{6.12}$$

$$B_g \to D_B\, B_g\,, \quad D_B(z,\boldsymbol{k}_1,\boldsymbol{k}_2,\boldsymbol{k}_3) = \exp\Big\{-\frac{1}{2}\big[k_1^2\mu_1^2 + k_2^2\mu_2^2 + k_3^2\mu_3^2\big]\,\sigma(z)^2\Big\}\,, \tag{6.13}$$

where σ is the linear velocity dispersion.

On sufficiently large scales the non-Gaussian contribution to the bispectrum covariance can be approximated by including corrections to the power spectra appearing in the bispectrum variance (B.5). This is shown by Chan & Blot (2017) (see also Karagiannis et al. (2018)), using the approximation:

$$\mathrm{Var}[B_g] \to \mathrm{Var}[B_g] + \delta\mathrm{Var}[B_g]\,, \tag{6.14}$$

$$\delta\mathrm{Var}[B_g] = \frac{s_B \pi k_\mathrm{f}^3 N_{\mu_1} N_\varphi}{k_1 k_2 k_3 (\Delta k)^3 \Delta\mu_1 \Delta\varphi}\Big\{\tilde{P}_{g\mathrm{N}}(1)\tilde{P}_{g\mathrm{N}}(2)\Big[\tilde{P}_{g\mathrm{N}}^{\mathrm{NL}}(3) - \tilde{P}_{g\mathrm{N}}(3)\Big] + 2\,\mathrm{cp}\Big\}\,. \tag{6.15}$$

Here $\tilde{P}_{g\mathrm{N}}(a) \equiv \tilde{P}_{g\mathrm{N}}(z, k_a, \mu_a)$ and $\tilde{P}_{g\mathrm{N}}^{\mathrm{NL}}(a) = (b + f\mu_a^2)^2 P^{\mathrm{NL}} + n_g^{-1}$, where P^{NL} is the nonlinear matter power spectrum, computed with a modified Halofit emulator.

6.2.3. Summations over triangles

The counting of triangles $\boldsymbol{k}_1 + \boldsymbol{k}_2 + \boldsymbol{k}_3 = \boldsymbol{0}$ that contribute to the signal-to-noise involves a sum in k_a-space and a sum over orientations.

The triangle sides are chosen so that $k_1 \geq k_2 \geq k_3$, and must satisfy $k_1 - k_2 - k_3 \leq 0$. For the summation in k_a we choose the minimum and the step-length as

$$k_{\min}(z) = k_\mathrm{f}(z) \quad \text{and} \quad \Delta k(z) = k_\mathrm{f}(z)\,, \tag{6.16}$$

as in Karagiannis et al. (2018); Yankelevich & Porciani (2019). Then the k_a sum is defined as Liguori et al. (2010); Oddo et al. (2020)

$$\sum_{k_a} = \sum_{k_1 = k_{\min}}^{k_{\max}} \sum_{k_2 = k_{\min}}^{k_1} \sum_{k_3 = k_{\min}}^{k_2}\,. \tag{6.17}$$

The coordinates ($\mu_1 = \cos\theta_1, \varphi$) describe all possible orientations of the triangle. We follow Karagiannis et al. (2018) and choose the ranges $N_{\mu_1} = 2, N_\varphi = 2\pi$. For a given μ_1, a complete rotation in φ about $\boldsymbol{k}_1$ double counts the triangle falling onto the fixed $(\boldsymbol{n}, \boldsymbol{k}_1)$-plane at $\varphi = 0$ and $\varphi = 2\pi$ (see Fig. 5.1). Similarly, for a given φ, the end-points $\theta_1 = 0$ and $\theta_1 = \pi$ correspond to equivalent triangles, with $\boldsymbol{k}_a \to -\boldsymbol{k}_a$. This double-counting can be avoided by imposing suitable upper limits: $-1 \leq \mu_1 < 1$ and $0 \leq \varphi < 2\pi$. The signal to noise is quite sensitive to the step-lengths $\Delta\mu_1, \Delta\varphi$. We find (see the Appendix for details) that a suitable choice for convergence is

$$\Delta\mu_1 = 0.04\,, \quad \Delta\varphi = \pi/25\,. \tag{6.18}$$

6.3. Galaxy Survey

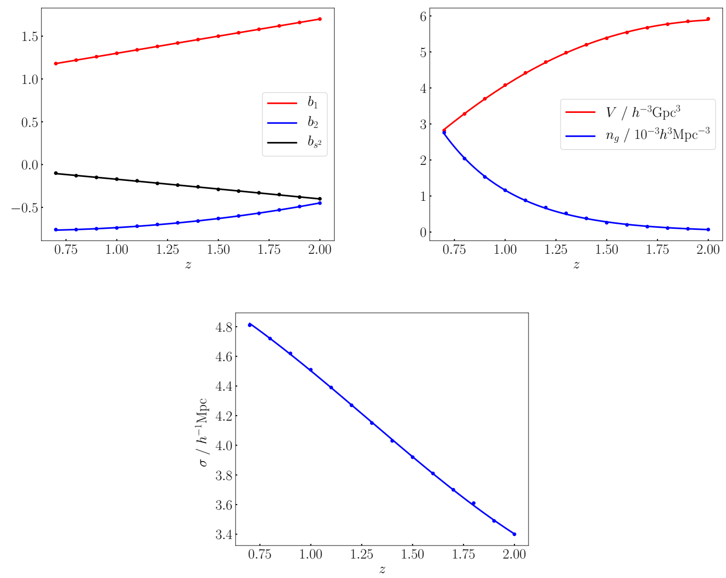

Figure 6.1.: Clustering bias parameters (*left*), comoving volume and number density (*middle*) and RSD damping parameter (*right*). Points are the data from Table 1 in Yankelevich & Porciani (2019).

We consider a Stage IV $H\alpha$ spectroscopic survey, with clustering bias, comoving volume, comoving number density and RSD damping parameter given by Table 1 in Yankelevich & Porciani (2019), over the redshift range $0.65 \leq z \leq 2.05$, with $\Delta z = 0.1$ bins. We provide fitting formulas for these quantities in the Appendix. Figure 6.1 shows the values given in Yankelevich & Porciani (2019) together with the fitting curves. For the cosmological parameters, we use Planck 2018 Aghanim et al. (2018): $h = 0.6766, \Omega_{m0} = 0.3111, \Omega_{b0}h^2 = 0.02242, \Omega_{c0}h^2 = 0.11933, n_s = 0.9665, \sigma_8 = 0.8102, \gamma = 0.545, \Omega_{K0} = 0 = \Omega_{\nu 0}$.

We checked that the SNR for the Newtonian bispectrum is consistent with Fig. 4 of Yankelevich & Porciani (2019), when we use their redshift-independent $k_{\rm max} = 0.15h$ Mpc^{-1}, and when we remove the flattened triangle shapes that are excluded by Yankelevich & Porciani (2019). When we include the flattened shapes, we checked that we recover the total number of triangles given in Table 1 of Oddo et al. (2020).

6.3.1. Evolution bias and magnification bias

The relativistic bispectrum depends also on b_e and $\mathcal{Q}$, as shown in (5.10)–(5.14). These parameters do *not* appear in the Newtonian approximation, but they are crucial for the relativistic correction, and we need to evaluate them in a physically consistent way. We compute these parameters from the same luminosity function that is used to generate the number density shown in Fig. 6.1, i.e., Model 1 in Pozzetti et al. (2016):

$$\Phi(z, y) = \Phi_*(z) y^\alpha \, \mathrm{e}^{-y} \,, \quad y \equiv \frac{L}{L_*} \,. \tag{6.19}$$

We have written Φ in terms of the redshift z and the normalised dimensionless luminosity y, where $L_* = L_{*0}(1+z)^\delta$ and L_{*0} is a characteristic luminosity. Here α is the faint-end slope, and Φ_* is a characteristic comoving density of $H\alpha$ emitters, modelled as

$$\frac{\Phi_*}{\Phi_{*0}} = \begin{cases} (1+z)^\epsilon & z \le z_{\rm b} \,, \\ (1+z_{\rm b})^{2\epsilon}(1+z)^{-\epsilon} & z > z_{\rm b} \,. \end{cases} \tag{6.20}$$

The best-fit parameters for Model 1 are given by Pozzetti et al. (2016) as

$$\alpha = -1.35 \,, \quad \delta = 2 \,, \quad L_{*0} = 10^{41.5} \, \mathrm{erg\, s^{-1}} \,, \quad \Phi_{*0} = 10^{-2.8} \, \mathrm{Mpc^{-3}} \,, \quad \epsilon = 1 \,, \quad z_{\rm b} = 1.3 \,. \tag{6.21}$$

The flux cut $F_{\rm c}$ translates to a luminosity cut:

$$L_{\rm c}(z) = 4\pi F_{\rm c} \, d_L(z)^2 \,, \quad F_{\rm c} = 3 \times 10^{-16} \, \mathrm{erg\, cm^{-2}\, s^{-1}} \,, \tag{6.22}$$

where d_L is the background luminosity distance and the choice of F_c follows Yankelevich & Porciani (2019).

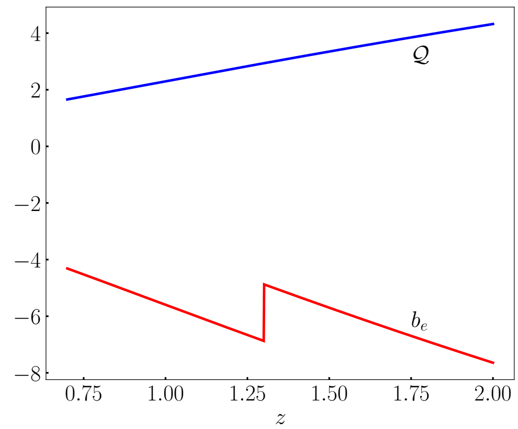

Figure 6.2.: Magnification and evolution bias (6.25), (6.26).

In order to compute b_e and $\mathcal{Q}$, we require the comoving number density

$$n_g(z) = \int_{y_c(z)}^{\infty} \mathrm{d}y\, \Phi(z,y) = \Phi_*(z)\, \Gamma(\alpha+1, y_c(z))\,, \tag{6.23}$$

where Γ is the upper incomplete Gamma function and

$$y_c(z) = \frac{4\pi F_\mathrm{c}}{L_{*0}}\, r(z)^2 = \left[\frac{r(z)}{2.97\,h \times 10^3\ (\mathrm{Mpc}/h)}\right]^2 . \tag{6.24}$$

Using (6.24) and (6.19)–(6.22), we confirm that the analytical form (6.23) for n_g recovers the points from Table 1 in Yankelevich & Porciani (2019).

By (5.15), the magnification bias follows as

$$\mathcal{Q}(z) = \left(y\,\frac{\Phi}{n_g}\right)_\mathrm{c} = \frac{y_\mathrm{c}(z)^{\alpha+1} \exp\big[-y_\mathrm{c}(z)\big]}{\Gamma(\alpha+1, y_\mathrm{c}(z))}\,, \tag{6.25}$$

since $\partial/\partial \ln L = \partial/\partial \ln y$, and the evolution bias is

$$b_e(z) = -\frac{\mathrm{d}\ln \Phi_*(z)}{\mathrm{d}\ln(1+z)} + \frac{\mathrm{d}\ln y_\mathrm{c}(z)}{\mathrm{d}\ln(1+z)}\, \mathcal{Q}(z)\,. \tag{6.26}$$

Figure 6.2 shows the analytical forms (6.25) and (6.26) for b_e and $\mathcal{Q}$.

Table 6.1 collects the information in Figs. 6.1 and 6.2 to provide an extension of

Table 1 in Yankelevich & Porciani (2019).

Table 6.1.: Stage IV $H\alpha$ spectroscopic survey parameters.

z	b_1	b_2	b_{s^2}	b_e	$\mathcal{Q}$	n_g $10^{-3}h^3\mathrm{Mpc}^{-3}$	V $h^{-3}\mathrm{Gpc}^3$	σ $h^{-1}\mathrm{Mpc}$
0.7	1.18	-0.766	-0.105	-4.31	1.66	2.76	2.82	4.81
0.8	1.22	-0.759	-0.127	-4.74	1.87	2.04	3.38	4.72
0.9	1.26	-0.749	-0.149	-5.17	2.08	1.53	3.70	4.62
1.0	1.30	-0.737	-0.172	-5.60	2.30	1.16	4.08	4.51
1.1	1.34	-0.721	-0.194	-6.02	2.51	0.880	4.42	4.39
1.2	1.38	-0.703	-0.217	-6.45	2.72	0.680	4.72	4.27
1.3	1.42	-0.682	-0.240	-6.76	2.94	0.520	4.98	4.15
1.4	1.46	-0.658	-0.262	-5.29	3.14	0.380	5.20	4.03
1.5	1.50	-0.631	-0.285	-5.70	3.35	0.260	5.38	3.92
1.6	1.54	-0.600	-0.308	-6.10	3.55	0.200	5.54	3.81
1.7	1.58	-0.567	-0.332	-6.50	3.75	0.150	5.67	3.70
1.8	1.62	-0.531	-0.355	-6.89	3.94	0.110	5.77	3.61
1.9	1.66	-0.491	-0.378	-7.27	4.13	0.0900	5.85	3.49
2.0	1.70	-0.449	-0.401	-7.64	4.32	0.0700	6.92	3.40

Finally, we need to deal with the luminosity derivative of the bias in (5.13). Simulations by Pan et al. (2019) indicate that the clustering bias of $H\alpha$ galaxies does not vary appreciably with luminosity near the fiducial luminosity L_{*0} in (6.21) and for $z \lesssim 2$ (see their Fig. 8). We therefore take

$$\left.\frac{\partial b_1}{\partial \ln L}\right|_{\mathrm{c}} = 0\,, \tag{6.27}$$

in (5.13).

6.3.2. Signal to noise of the relativistic bispectrum

We can now evaluate the Doppler-type relativistic part of the bispectrum, (5.8)–(5.14), using (6.25)–(6.27). Then the SNR is computed using (6.5) and (6.10) together with (6.15). The results, for SNR in each z-bin, $S/N(z)$, and for the cumulative SNR, $S/N(\leq z)$, are shown in Fig. 6.3. Our forecasts indicate that the total SNR, $S/N(\leq z_{\max})$, for a Stage IV $H\alpha$ survey could be $\mathcal{O}(10)$, which is high enough for a detection in principle.

The relativistic SNR is sensitive in particular to two factors:

- Changes in the nonperturbative scale $k_{\rm max}(z)$: this sensitivity is due to the coupling of long-wavelength relativistic terms to short-wavelength Newtonian terms. We use a conservative and redshift-dependent $k_{\rm max}$, given in (6.11). In Fig. 6.4 we show the comparison of SNR using (6.11) and using the redshift-independent $k_{\rm max} = 0.15h/\,$Mpc. The redshift-independent model does not incorporate the increase in the nonperturbative scale with growing z, and therefore produces a lower SNR; however, the difference is not large.

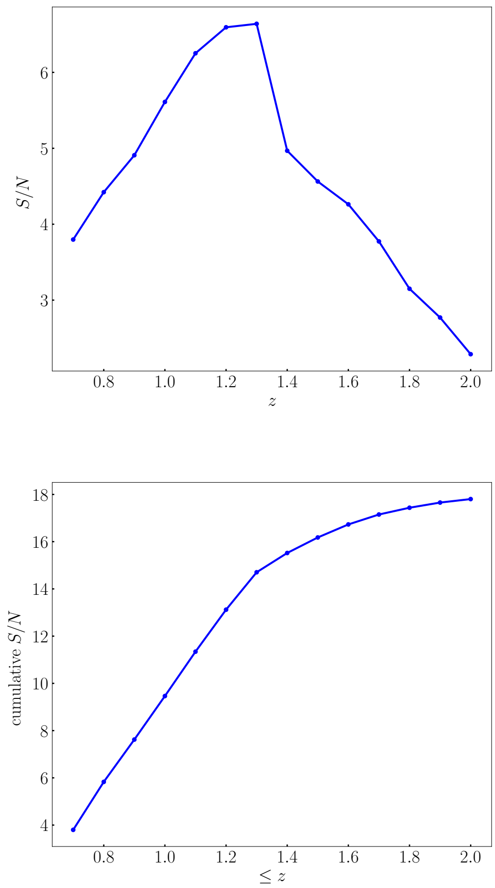

Figure 6.3.: Relativistic SNR per z-bin (*left*) and cumulative (*right*) for a Stage IV $H\alpha$ survey.

- Changes in $b_e(z), \mathcal{Q}(z)$: In the Appendix (Fig. G.2) we illustrate the significant impact on cumulative SNR of changing $b_e, \mathcal{Q}$. We use a range of constant choices for $b_e, \mathcal{Q}$ – which are not physically motivated. This shows the importance of modelling $b_e, \mathcal{Q}$ self-consistently from the same luminosity function that produces the number density, as we have done.

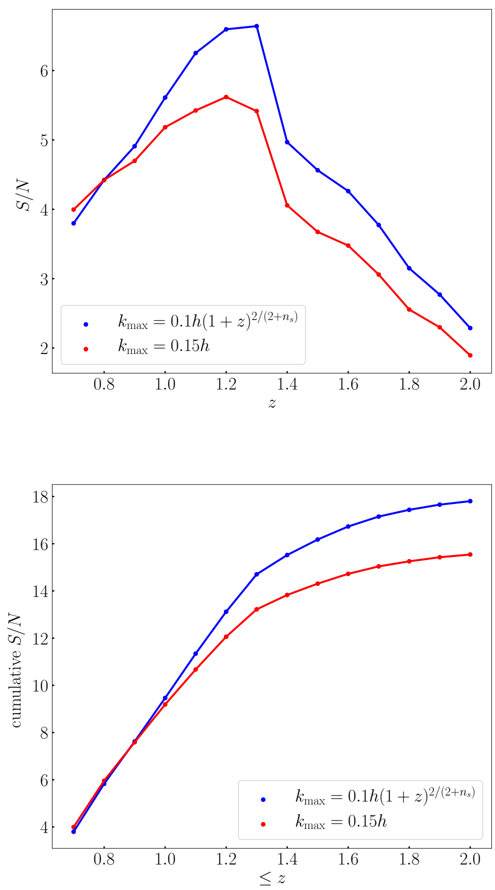

Figure 6.4.: Effect of changing $k_{\rm max}$ on SNR per bin (*left*) and cumulative SNR (*right*).

The sensitivity of the relativistic SNR to $k_{\rm max}$ reflects the importance of the coupling of the relativistic signal to Newtonian terms on short scales. How sensitive is the SNR to the signal on the largest scales? We can answer this by increasing $k_{\rm min}$ from its fiducial value $k_{\rm f}$, which is the maximal observable scale. The result is that there is only a small reduction when $k_{\rm min}/k_{\rm f}$ is increased by a factor up to 5, as shown in Fig. 6.5. Even with $k_{\rm min} = 10k_{\rm f}$, the total SNR is ~ 10. This means that the relativistic SNR does not depend critically on accessing the largest possible scales.

It is also interesting to investigate how important for the SNR is the second-order relativistic contribution in the bispectrum, i.e. from terms of the form

$$\mathcal{K}_{\rm N}^{(1)}(\boldsymbol{k}_1)\mathcal{K}_{\rm N}^{(1)}(\boldsymbol{k}_2)\mathcal{K}_{\rm D}^{(2)}(\boldsymbol{k}_1, \boldsymbol{k}_2, \boldsymbol{k}_3)\,, \tag{6.28}$$

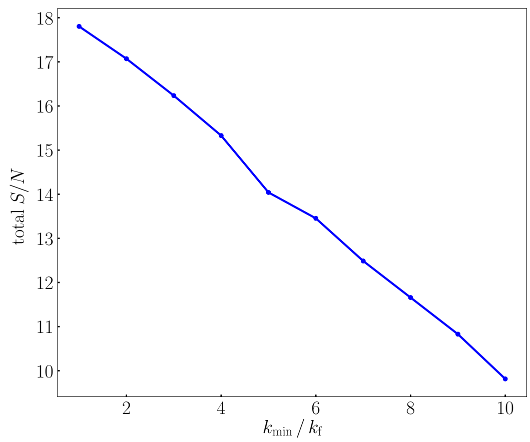

Figure 6.5.: Effect of changing $k_{\rm min}$ on total relativistic SNR.

in (5.8), compared to the first-order contribution, i.e. from terms of the form

$$\Big[\mathcal{K}_{\rm N}^{(1)}(\boldsymbol{k}_1)\mathcal{K}_{\rm D}^{(1)}(\boldsymbol{k}_2)+\mathcal{K}_{\rm D}^{(1)}(\boldsymbol{k}_1)\mathcal{K}_{\rm N}^{(1)}(\boldsymbol{k}_2)\Big]\mathcal{K}_{\rm N}^{(2)}(\boldsymbol{k}_1,\boldsymbol{k}_2,\boldsymbol{k}_3)\,. \tag{6.29}$$

It is conceivable that the first-order Doppler-type contribution in (6.29) to B_g, which couples to first- and second-order Newtonian terms, dominates the SNR. However, we find that the first- and second-order relativistic parts of the bispectrum make comparable contributions to the SNR – see Fig. 6.6. We deduce that the second-order relativistic contribution in (6.28) cannot be neglected. Furthermore, this means that it must be accurately modelled, as we have done.

Recently Jeong & Schmidt (2020) estimated the SNR for the leading relativistic part of the bispectrum. There are significant differences in their analysis compared to ours. In particular, they neglect most of the terms in $\delta_{g\rm D}^{(2)}$ [see our (4.4)] which defines $\mathcal{K}_{\rm D}^{(2)}$ (see the Appendix for further details). In addition they do not use self-consistent models for b_e and $\mathcal{Q}$. These two differences could account for their conclusion that the relativistic signal is not detectable, in contrast to our result.

An interesting feature of the relativistic signal is that there is a significant contribution to the SNR from flattened triangle shapes. This is consistent with the results of Clarkson et al. (2019) for the dipole that is generated by the imaginary part of the bispectrum.

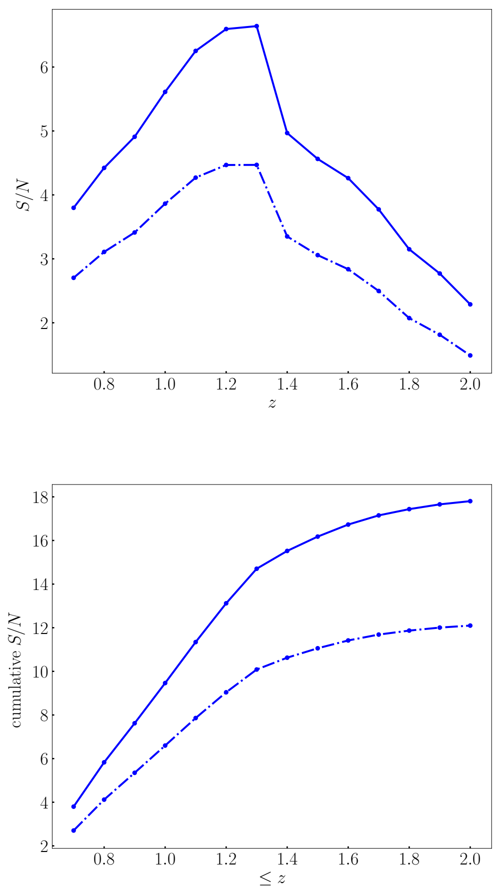

Figure 6.6.: As in Fig. 6.3, but showing the effect of omitting the second-order relativistic contribution (6.28) to the bispectrum (dot-dashed curves).

6.3.3. Including cosmological parameters

A full treatment of cosmological constraints would marginalise over the standard cosmological parameters, together with the Alcock-Paczynski parameters and the clustering bias parameters. The constraints obtained would depend almost entirely on the Newtonian galaxy power spectrum and bispectrum (as analysed in Yankelevich & Porciani (2019)), given that the relativistic contribution to the power spectrum is below leading order, while in the bispectrum the relativistic SNR is an order of magnitude smaller than the Newtonian SNR.

Our focus here is instead on the detectability of the relativistic signal in the bispectrum, assuming that $P_{g\mathrm{N}}$ and $B_{g\mathrm{N}}$ have been used to constrain the standard parameters. We now investigate the effect on this detectability when we include the param-

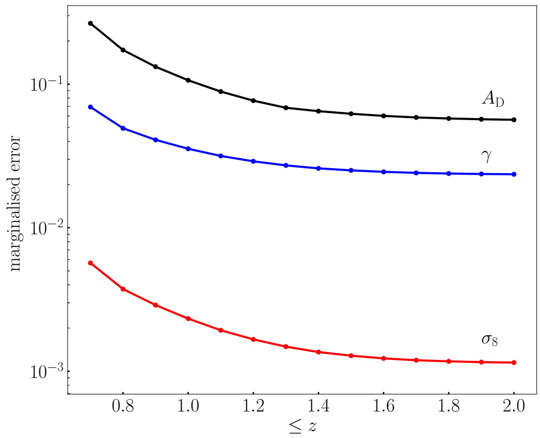

Figure 6.7.: Marginal errors (cumulative) on the relativistic contribution, growth index and clustering amplitude, using the full bispectrum.

eters directly related to redshift-space effects, i.e., the growth index $\gamma = \ln f / \ln \Omega_m$ (with fiducial value 0.545), and the clustering amplitude σ_8 (with Planck 2018 fiducial). For forecasts we use the theoretical values of $b_e, \mathcal{Q}$. In a galaxy survey, they would be measured directly from the observed luminosity function, and their measurement uncertainties would need to be marginalised over.

For the relativistic part of the bispectrum, we introduce a parameter $A_{\rm D}$, with fiducial value 1:

$$B_g = B_{g\rm N} + A_{\rm D}\, B_{g\rm D}\,. \tag{6.30}$$

Then the Fisher matrix for the parameters $\vartheta_\alpha = (A_{\rm D}, \gamma, \sigma_8)$ is

$$F_{\alpha\beta} = \sum_{z, k_a, \mu_1, \varphi} \frac{1}{\mathrm{Var}[B_g]} \frac{\partial B_g}{\partial \vartheta_{(\alpha}} \frac{\partial B_g^*}{\partial \vartheta_{\beta)}}\,, \tag{6.31}$$

where the round brackets denote symmetrisation. The cumulative marginal errors $\sigma_\alpha = [(F^{-1})_{\alpha\alpha}]^{1/2}$ are shown in Fig. 6.7. The fact that $\sigma_{A_{\rm D}} \lesssim 0.1$ means that the relativistic effects remain detectable when the two additional cosmological parameters are marginalised over.

6.4. Conclusions

As shown by Clarkson et al. (2019), the tree-level galaxy bispectrum in Fourier space has an imaginary part which is a unique signal of the leading-order relativistic corrections in redshift space. These corrections arise from Doppler and other line-of-sight effects on the past lightcone [see (5.6), (4.4)]. In the galaxy bispectrum, the corrections scale as i $(\mathcal{H}/k)P^2$, where P is the linear matter power spectrum [see (5.8)–(5.10)]. By contrast, at leading order in the galaxy power spectrum, the relativistic correction is real and scales as $(\mathcal{H}/k)^2P$ – i.e., it is suppressed by a further factor of $\mathcal{H}/k$. Only the cross-power spectrum of two different tracers produces an imaginary contribution that scales as i $(\mathcal{H}/k)P$ McDonald (2009). [1]

For a single tracer, the $(\mathcal{H}/k)^2$ relativistic signal in the galaxy *power* spectrum is not detectable, even for a cosmic-variance limited survey Alonso et al. (2015). The galaxy bispectrum of a single tracer, with its i $(\mathcal{H}/k)$ relativistic contribution, improves the chances of detectability. In addition, the relativistic contribution in the bispectrum couples to short-scale Newtonian terms – which means that the signal is not confined to very large scales, unlike the case of the power spectrum. We confirmed the expectations of detectability by showing that the signal to noise on the imaginary relativistic part is $\mathcal{O}(10)$ for a Stage IV $H\alpha$ spectroscopic survey similar to Euclid [see Fig. 6.3]. We checked that detectability is not compromised by including the uncertainties on two cosmological growth parameters, σ_8 and γ [Fig. 6.7], assuming that other cosmological and nuisance parameters are determined by the Newtonian power spectrum and bispectrum.

The relativistic SNR depends on the $k_{\rm max}(z)$ assumed, because of the coupling of relativistic effects to short-scale Newtonian terms [Fig. 6.4], and we made a conservative choice (6.11), which includes a redshift dependence to reflect the weakening of nonlinearity at higher z. Accurate modelling of nonlinear effects would allow us to increase the SNR – this is not at all specific to the relativistic signal, but is required for the standard analysis of RSD.

The relativistic SNR also relies on the largest available scales, but very little signal is lost if $k_{\rm min}/k_{\rm f}$ is increased by a factor up to 5, and even a factor of 10 increase leaves a detectable SNR [Fig. 6.5].

By contrast, the SNR depends strongly on accurate modelling of the second-order part of the relativistic correction [Fig. 6.6]. This includes both the theoretical form (4.4), and the two astrophysical parameters that do not appear in the Newtonian

[1]See also Bonvin et al. (2014, 2016); Gaztanaga et al. (2017); Iršič et al. (2016); Hall & Bonvin (2017); Lepori et al. (2018); Bonvin & Fleury (2018); Lepori et al. (2020) for the corresponding effect in the two-point correlation function, and see Okoli et al. (2017) for an imaginary short-scale contribution from neutrino drag on haloes.

approximation of the galaxy bispectrum: the evolution bias b_e (measuring the deviation from comoving number conservation) and the magnification bias $\mathcal{Q}$ (which is brought into play by a Doppler correction to standard lensing magnification). A key feature of our analysis is a physically self-consistent derivation of these quantities from the luminosity function [Fig. 6.2 and (6.25), (6.26)]. We showed that the SNR is very sensitive to these parameters [Fig. G.2], which underlines the need for accurate physical modelling.

We assumed a Gaussian covariance in our computations, but we used the approximation of Chan & Blot (2017) to include non-Gaussian corrections.

Further work should include the window function which we have neglected. The imaginary part of the galaxy bispectrum generates a dipole, as shown in Clarkson et al. (2019). This suggests a multipole analysis that uses the relativistic dipole in addition to the monopole and quadrupole, which are unaffected by relativistic effects at leading order. The window function can also have an imaginary part Beutler et al. (2019), which will need to be corrected for. The dipole from the imaginary part of the bispectrum vanishes in equilateral configurations Clarkson et al. (2019), which may help to disentangle the relativistic dipole from that of the window function.

Our analysis, in common with other works on the Fourier bispectrum, implicitly uses the plane-parallel approximation, since the line-of-sight direction $\boldsymbol{n}$ is fixed. At the cost of significant complexity, the approximation can be avoided, for example by using a Fourier-Bessel analysis of bispectrum multipoles Castorina & White (2018). Further work is needed to address this, but we note that errors from the approximation are mitigated in high redshift surveys such as the one considered here.

Finally, further work also needs to include the effects of lensing magnification, which are excluded in the standard Fourier analysis, but have been included in the galaxy angular bispectrum Kehagias et al. (2015); Di Dio et al. (2016, 2017, 2019) and in a spherical Bessel analysis Bertacca et al. (2018).

7. Multipoles of the Bispectrum

7.1. Background theory

Galaxy number count fluctuations are distorted due to the fact that we observe on the past lightcone. A well-known effect is the Kaiser redshift-space distortion (RSD) effect (Verde et al., 1998; Scoccimarro et al., 1999). Further distortions are due to lensing convergence, as well as due to Doppler, Sachs-Wolfe, Integrated Sachs-Wolfe (ISW), and time delay effects; all of which are suppressed on sub-equality scales. There are also couplings between these effects when one goes up to non-linear order.

The observed galaxy power spectrum at tree level involves only the projection effects at first order. However, the bispectrum, even at tree level, involves both first- and second-order relativistic projection effects.

7.1.1. Galaxy number counts in General Relativity

what do galaxy surveys measure? > measure the observed density of galaxies compared to some background number

Let an observer look down the past light cone in observed direction $\boldsymbol{n}$ and count a number of galaxies dN, which are above some threshold luminosity L, within a redshift interval $\mathrm{d}z$ about the observed redshift z, and within a solid angle element $\mathrm{d}\Omega_o$,

$$\mathrm{d}N(z, \boldsymbol{n}, > \ln L) = \mathcal{N}(z, \boldsymbol{n}, > \ln L) D_A^2(z, \boldsymbol{n}) k_\mu u^\mu \frac{\mathrm{d}\lambda}{\mathrm{d}z}\, \mathrm{d}z\, \mathrm{d}\Omega_o. \tag{7.1}$$

Here, D_A is the angular diameter distance, u^μ is the source 4-velocity, $k^\mu = \frac{\mathrm{d}x^\mu}{\mathrm{d}\lambda}$ is the geodesic photon 4-momentum, and $\mathcal{N}$ is the flux-limited number density of sources,

$$\mathcal{N}(z, \boldsymbol{n}, > \ln L) = \int_0^\infty \mathrm{d}\, \ln \tilde{L} n \tag{7.2}$$

introduction to the full theory : sheeans papers

Above the equality scale the galaxy bispectrum will be a key probe for measuring primordial non-Gaussianity which can help differentiate between different inflationary models and other theories of the early universe. On these scales a variety of relativistic effects come into play once the galaxy number-count fluctuation is projected onto our past lightcone. By decomposing the Fourier-space bispectrum into invariant multipoles about the observer's line of sight we examine in detail how the relativistic effects contribute to these. We show how to perform this decomposition analytically, which is significantly faster for subsequent computations. While all multipoles receive a contribution from the relativistic part, odd multipoles arising from the imaginary part of the bispectrum have no Newtonian contribution, making the odd multipoles a smoking gun for a relativistic signature in the bispectrum for single tracers. The dipole and the octopole are significant on equality scales and above where the Newtonian approximation breaks down. This breakdown is further signified by the fact that the even multipoles receive a significant correction on very large scales.

7.2. Introduction

The bispectrum will play a key role in future galaxy surveys as an important probe of large-scale structure and for measuring primordial non-Gaussianity and galaxy bias Jeong & Komatsu (2009); Baldauf et al. (2011); Celoria & Matarrese (2020). It can help discriminate between different inflationary models and other theories of the early universe, and contains information that is complementary and additional to what is contained in the power spectrum. On super-equality scales, a variety of relativistic effects come into play once the galaxy number-count fluctuation is projected onto the past light cone. In the density contrast up to second order, relativistic effects arise from observing on the past lightcone, and they include all redshift, volume and lensing distortions and couplings between these. In Poisson gauge, these effects can be attributed to velocities (Doppler), gravitational potentials (Sachs-Wolfe, integrated SW, time delay) and lensing magnification and shear. In addition, there are corrections arising from a GR definition of galaxy bias Bertacca et al. (2014b). These effects generate corrections to the Newtonian approximation at order $\mathcal{O}(\mathcal{H}/k)$ and higher. Non-Gaussianity generated by these relativistic projection effects could closely mimic the signature of $f_{\rm NL}$ on large scales which gives a correction in the halo bias $\mathcal{O}((\mathcal{H}/k)^2)$, indicating the importance of precisely including all $\mathcal{O}(\mathcal{H}/k)$ and higher effects in theoretical modelling. So far, a variety of relativistic effects in the galaxy Fourier bispectrum has been taken into account, see Umeh et al. (2017); Jolicoeur et al. (2017, 2018, 2019); Clarkson et al. (2019); Maartens et al. (2020) under the assumption of the plane parallel approximation, and neglecting integrated effects. Other groups are working on this from different angles and approaches, for example by a spherical-Fourier formalism Bertacca et al. (2018), and calculating the angular galaxy bispectrum Di Dio et al. (2017, 2019). Crucially, we have shown that the relativistic part should be detectable in a survey like Euclid without resorting to the multi-tracer technique, which is needed for the power spectrum Maartens et al. (2020) .

Once an observable like the galaxy number-count fluctuation is projected onto the past lightcone the orientation of the triangle in the Fourier space bispectrum becomes important. Analogously to how the Legendre multipole expansion is used for power spectrum analysis, one can expand the galaxy bispectrum in spherical harmonics, thus isolating the different invariant multipoles with respect to the observer's line of sight $\boldsymbol{n}$. We use the full spherical harmonics for the bispectrum rather than the Legendre polynomial expansion usually adopted for the power spectrum because of the azimuthal degrees of freedom associated with the orientation of the triangle with respect to the line of sight direction vector in Fourier space. In the power spectrum limit, there is only one angular degree of freedom after ensemble averaging. For the bispectrum, we have one angular and one azimuthal degree of freedom which when expanded in spherical harmonics leads to $(2\ell + 1)$ independent harmonics for each multipole value ℓ.

This has been done for the Newtonian bispectrum, which generates non-zero multipoles only for even ℓ (up to $\ell = 8$) due to redshift-space distortions Scoccimarro et al. (1999); Nan et al. (2018). Contrary to the Newtonian bispectrum, the relativistic galaxy bispectrum generates non-zero multipoles for both even and odd ℓ up to $\ell = 8$ and $m = 6$ where the odd multipoles are induced by the general relativistic effects only. This means that these multipoles are a crucial signature of relativistic projection effects. We provide, for the first time, a multipole decomposition of the Fourier space galaxy bispectrum with relativistic effects included. Additionally we show that the coefficients of this expansion can be worked out analytically. We provide an exact analytic formula for this multipole expansion of the galaxy bispectrum. Previously, we examined for the first time the dipole of the galaxy bispectrum in detail, showing that its amplitude can be more than 10% of that of the monopole even at equality scales Clarkson et al. (2019). In order to eliminate possible biases when analysing large scale structure data, it is important to include the relativistic effects. In addition to this, a variety of the effects that appear in the bispectrum are relativistic effects that have not been measured elsewhere and hence are interesting to study. By analysing the non-zero multipoles of the galaxy bispectrum both for a Euclid-like galaxy survey, and for an SKA-like HI intensity mapping survey, we show the behaviour of the higher multipoles and their corrections to the Newtonian bispectrum. In follow-up work, we are investigating possibilities of detecting the higher multipoles of the bispectrum. See for example Maartens et al. (2020) for detection prospects of the leading order relativistic effects; the dipole is expected to have the strongest GR signature.

The paper is organised as follows. We introduce the relativistic Fourier space bispectrum in section 7.3, and present the multipole expansion of the relativistic bispectrum in section 7.4. An analysis of the multipoles can be found in section 7.5. Finally, we summarise our conclusions in section 7.6.

7.3. The relativistic bispectrum

In Fourier space, the observed galaxy bispectrum B_g at a fixed redshift z is given by Jolicoeur et al. (2017, 2018)

$$\langle \Delta_g(z, \boldsymbol{k}_1)\Delta_g(z, \boldsymbol{k}_2)\Delta_g(z, \boldsymbol{k}_3)\rangle = (2\pi)^3 B_g(z, \boldsymbol{k}_1, \boldsymbol{k}_2, \boldsymbol{k}_3)\delta^D(\boldsymbol{k}_1 + \boldsymbol{k}_2 + \boldsymbol{k}_3), \tag{7.3}$$

where $\Delta_g(z, \boldsymbol{k}_1)$ is the number count contrast at redshift z (see Jolicoeur et al. (2017) for the full expression). Here we work in the Poisson gauge; note that $\Delta_g = \delta_g + \text{RSD} + \text{GR}$ projection effects, where the RSD term is the Kaiser RSD up to second order, which is part of the Newtonian approximation. Since redshift is fixed, in what follows we drop redshift dependence for brevity. Furthermore, since the observed direction $\boldsymbol{n}$ is fixed in what follows, the plane-parallel approximation is necessarily assumed. Then, at tree level, and for Gaussian initial conditions, the following combinations of terms contribute,

$$\langle \Delta_g(\boldsymbol{k}_1)\Delta_g(\boldsymbol{k}_2)\Delta_g(\boldsymbol{k}_3)\rangle = \frac{1}{2}\langle \Delta_g^{(1)}(\boldsymbol{k}_1)\Delta_g^{(1)}(\boldsymbol{k}_2)\Delta_g^{(2)}(\boldsymbol{k}_3)\rangle + 2 \text{ cyclic permutations.} \tag{7.4}$$

Using Wick's theorem, this gives an expression for the galaxy bispectrum Jolicoeur et al. (2017)

$$B_g(\boldsymbol{k}_1, \boldsymbol{k}_2, \boldsymbol{k}_3) = \mathcal{K}^{(1)}(\boldsymbol{k}_1)\mathcal{K}^{(1)}(\boldsymbol{k}_2)\mathcal{K}^{(2)}(\boldsymbol{k}_1, \boldsymbol{k}_2, \boldsymbol{k}_3)P(\boldsymbol{k}_1)P(\boldsymbol{k}_2) + 2 \text{ cyclic permutations}, \tag{7.5}$$

where P is the power spectrum of $\delta_{\mathrm{T}}^{(1)}$, the first order dark matter density contrast in the total-matter gauge, which corresponds to an Eulerian frame. The first order kernel can be split into a Newtonian and a relativistic part as Jeong et al. (2012)

$$\mathcal{K}^{(1)} = \mathcal{K}_{\mathrm{N}}^{(1)} + \mathcal{K}_{\mathrm{GR}}^{(1)}, \qquad \mathcal{K}_{\mathrm{N}}^{(1)} = b_1 + f\mu^2, \qquad \mathcal{K}_{\mathrm{GR}}^{(1)} = \mathrm{i}\,\mu\frac{\gamma_1}{k} + \frac{\gamma_2}{k^2}, \tag{7.6}$$

with $\mu = \hat{\boldsymbol{k}} \cdot \boldsymbol{n}$ ($\hat{\boldsymbol{k}} = \boldsymbol{k}/k$), b_1 is the first-order Eulerian galaxy bias coefficient, f is the linear growth rate of matter perturbations, and redshift-dependent coefficients γ_i are Jeong et al. (2012),

$$\frac{\gamma_1}{\mathcal{H}} = f\left[b_e - 2\mathcal{Q} - \frac{2(1-\mathcal{Q})}{\chi\mathcal{H}} - \frac{\mathcal{H}'}{\mathcal{H}^2}\right], \tag{7.7}$$

$$\frac{\gamma_2}{\mathcal{H}^2} = f(3-b_e) + \frac{3}{2}\Omega_m\left[2 + b_e - f - 4\mathcal{Q} - \frac{2(1-\mathcal{Q})}{\chi\mathcal{H}} - \frac{\mathcal{H}'}{\mathcal{H}^2}\right]. \tag{7.8}$$

In equations (7.7) and (7.8), $\mathcal{H}$ is the conformal Hubble rate $(\ln a)'$, where a prime denotes a derivative with respect to conformal time; b_e and $\mathcal{Q}$ are the galaxy evolution and magnification biases respectively, χ is the line-of-sight comoving distance and $\Omega_m = \Omega_{m0}(1+z)H_0^2/\mathcal{H}^2$ is the matter density parameter. At first order, the gauge-independent GR definition of galaxy bias is made in the common comoving frame of galaxies and matter,

$$\delta_{g\mathrm{C}}^{(1)} = b_1\delta_{\mathrm{C}}^{(1)} = b_1\delta_{\mathrm{T}}^{(1)}\,, \tag{7.9}$$

where subscript C is for the comoving gauge and T is for total matter gauge, which is a gauge corresponding to standard Newtonian perturbation theory. The bias relation in Poisson gauge is then obtained by transforming (7.9) to Poisson gauge Bertacca et al. (2014b); Jolicoeur et al. (2018):

$$\delta_g^{(1)} = \delta_{g\mathrm{C}}^{(1)} + (3-b_e)\mathcal{H}v^{(1)} = b_1\delta_{\mathrm{T}}^{(1)} + (3-b_e)\mathcal{H}v^{(1)}, \tag{7.10}$$

where $v^{(1)}$ is the velocity potential. Since $v^{(1)} = f\mathcal{H}\delta_T^{(1)}/k^2$, the last term on the right of equation (7.10) leads to the $f(3-b_e)$ term in $\gamma_2/\mathcal{H}^2$, equation (7.8).

Similarly to the first order kernel, the second order kernel can be split into a Newtonian and a relativistic part. The second order part of the Newtonian kernel is well studied and is given as Bernardeau et al. (2002); Karagiannis et al. (2018); Scoccimarro et al. (1999); Verde et al. (1998)

$$\mathcal{K}^{(2)}_{\mathrm{N}}(\boldsymbol{k}_1, \boldsymbol{k}_2, \boldsymbol{k}_3) = b_1 F_2(\boldsymbol{k}_1, \boldsymbol{k}_2) + b_2 + f\mu_3^2 G_2(\boldsymbol{k}_1, \boldsymbol{k}_2) + f Z_2(\boldsymbol{k}_1, \boldsymbol{k}_2) + b_{s^2} S_2(\boldsymbol{k}_1, \boldsymbol{k}_2), \tag{7.11}$$

where $\mu_i = \hat{\boldsymbol{k}}_i \cdot \boldsymbol{n}$, b_2 is the second-order Eulerian bias parameter, and b_{s^2} is the tidal bias. F_2 and G_2 are the Fourier-space Eulerian kernels for second-order density contrast and velocity respectively Jolicoeur et al. (2017); Villa & Rampf (2016);

$$\begin{aligned} F_2(\boldsymbol{k}_1, \boldsymbol{k}_2) &= 1 + \frac{F}{D^2} + \left(\hat{\boldsymbol{k}}_1 \cdot \hat{\boldsymbol{k}}_2\right)\left(\frac{k_1}{k_2} + \frac{k_2}{k_1}\right) + \left(1 - \frac{F}{D^2}\right)\left(\hat{\boldsymbol{k}}_1 \cdot \hat{\boldsymbol{k}}_2\right)^2, \\ G_2(\boldsymbol{k}_1, \boldsymbol{k}_2) &= \frac{F'}{DD'} + \left(\hat{\boldsymbol{k}}_1 \cdot \hat{\boldsymbol{k}}_2\right)\left(\frac{k_1}{k_2} + \frac{k_2}{k_1}\right) + \left(2 - \frac{F'}{DD'}\right)\left(\hat{\boldsymbol{k}}_1 \cdot \hat{\boldsymbol{k}}_2\right)^2, \end{aligned} \tag{7.12}$$

where F is a second-order growth factor, which is given by the growing mode solution of,

$$F'' + \mathcal{H}F' - \frac{3}{2}\frac{H_0^2\Omega_{m0}}{a}F = \frac{3}{2}\frac{H_0^2\Omega_{m0}}{a}D^2. \tag{7.13}$$

In an Einstein-de Sitter background, $F = 3D^2/7$, which is a very good approximation for ΛCDM which we use here. The second-order RSD part of the Newtonian kernel is comprised of G_2 above and the kernel Z_2 Verde et al. (1998); Scoccimarro et al. (1999),

$$Z_2(\boldsymbol{k}_1, \boldsymbol{k}_2) = f\frac{\mu_1\mu_2}{k_1k_2}\left(\mu_1k_1 + \mu_2k_2\right)^2 + \frac{b_1}{k_1k_2}\left[\left(\mu_1^2 + \mu_2^2\right)k_1k_2 + \mu_1\mu_2\left(k_1^2 + k_2^2\right)\right]. \tag{7.14}$$

Finally, $S_2(\boldsymbol{k}_1, \boldsymbol{k}_2)$ is the kernel for the tidal bias,

$$S_2(\boldsymbol{k}_1, \boldsymbol{k}_2) = (\hat{\boldsymbol{k}}_1 \cdot \hat{\boldsymbol{k}}_2)^2 - \frac{1}{3}. \tag{7.15}$$

The Newtonian bias model is

$$\delta^{(2)}_{g\mathrm{T}} = b_1\delta^{(2)}_{\mathrm{T}} + b_2\left[\delta^{(1)}_{\mathrm{T}}\right]^2 + b_{s^2}s^2, \tag{7.16}$$

where $s^2 = s_{ij}s^{ij}$, and $s_{ij} = \Phi_{,ij} - \delta_{ij}\nabla^2\Phi/3$.

The relativistic part of the second order kernel was first derived in Umeh et al. (2017)

in the simplest case and extended in Jolicoeur et al. (2017, 2018, 2019). Neglecting sub-dominant vector and tensor contributions, we have

$$\begin{aligned}\mathcal{K}^{(2)}_{\mathrm{GR}}(\boldsymbol{k}_1,\boldsymbol{k}_2,\boldsymbol{k}_3) = \frac{1}{k_1^2k_2^2}\Big\{&\beta_1 + E_2(\boldsymbol{k}_1,\boldsymbol{k}_2,\boldsymbol{k}_3)\beta_2 + \mathrm{i}\,(\mu_1k_1+\mu_2k_2)\beta_3 + \mathrm{i}\,\mu_3k_3\left[\beta_4 + E_2(\boldsymbol{k}_1,\boldsymbol{k}_2,\boldsymbol{k}_3)\beta\right.\\ &+\frac{k_1^2k_2^2}{k_3^2}\left[F_2(\boldsymbol{k}_1,\boldsymbol{k}_2)\beta_6 + G_2(\boldsymbol{k}_1,\boldsymbol{k}_2)\beta_7\right] + (\mu_1k_1\mu_2k_2)\,\beta_8 + \mu_3^2k_3^2\left(\beta_9 + E_2(\boldsymbol{k}_1,\boldsymbol{k}_2,\boldsymbol{k}_3\right.\\ &+(\boldsymbol{k}_1\cdot\boldsymbol{k}_2)\,\beta_{11} + \left(k_1^2+k_2^2\right)\beta_{12} + \left(\mu_1^2k_1^2+\mu_2^2k_2^2\right)\beta_{13}\\ &+\mathrm{i}\Big[\left(\mu_1k_1^3+\mu_2k_2^3\right)\beta_{14} + (\mu_1k_1+\mu_2k_2)\,(\boldsymbol{k}_1\cdot\boldsymbol{k}_2)\,\beta_{15} + k_1k_2\,(\mu_1k_2+\mu_2k_1)\,\beta_{16}\\ &+\left(\mu_1^3k_1^3+\mu_2^3k_2^3\right)\beta_{17} + \mu_1\mu_2k_1k_2\,(\mu_1k_1+\mu_2k_2)\,\beta_{18} + \mu_3\frac{k_1^2k_2^2}{k_3}G_2(\boldsymbol{k}_1,\boldsymbol{k}_2)\beta_{19}\Big]\Big\}\,.\end{aligned} \tag{7.17}$$

We have collected terms according to the overall powers of k involved. The β_i here are redshift- and bias-dependent coefficients, given in full in appendix REF BETA APPENDIX, which updates expressions in previous papers. We have defined the kernel E_2 which scales as k^0 (like F_2, G_2, and Z_2 do),

$$E_2(\boldsymbol{k}_1,\boldsymbol{k}_2,\boldsymbol{k}_3) = \frac{k_1^2k_2^2}{k_3^4}\left[3 + 2\left(\hat{\boldsymbol{k}}_1\cdot\hat{\boldsymbol{k}}_2\right)\left(\frac{k_1}{k_2}+\frac{k_2}{k_1}\right) + \left(\hat{\boldsymbol{k}}_1\cdot\hat{\boldsymbol{k}}_2\right)^2\right], \tag{7.18}$$

which incorporates some of the relativistic dynamical corrections to the intrinsic second-order terms.

At second order, the GR bias model, which corrects the Newtonian bias model (7.16) is given by Umeh et al. (2019),

$$\delta^{(2)}_{g\mathrm{T}} = b_1\delta^{(2)}_{\mathrm{T}} + b_2\left[\delta^{(1)}_{\mathrm{T}}\right]^2 + b_{s^2}s^2 + \delta^{(2)}_{\mathrm{C,GR}}\,, \tag{7.19}$$

where the last term maintains gauge invariance on ultra-large scales, and is given by (using $\delta^{(1)}_{\mathrm{C}} = \delta^{(1)}_{\mathrm{T}}$)

$$\delta^{(2)}_{\mathrm{C,GR}} = 2\mathcal{H}^2(3\Omega_m + 2f)\left[\delta^{(1)}_{\mathrm{T}}\nabla^{-2}\delta^{(1)}_{\mathrm{T}} - \frac{1}{4}\partial_i\nabla^{-2}\delta^{(1)}_{\mathrm{T}}\partial^i\nabla^{-2}\delta^{(1)}_{\mathrm{T}}\right]. \tag{7.20}$$

The GR correction (7.20) to the Newtonian bias model is contained in the GR kernel (7.17). Then, we also need to transform $\delta^{(2)}_{g\mathrm{T}}$ to the Poisson gauge $\delta^{(2)}_g$, the expression for this is given in Jolicoeur et al. (2017),

$$\delta^{(2)}_g = \delta^{(2)}_{g\mathrm{T}} + (3-b_e)\mathcal{H}v^{(2)} + \left[(b_e-3)\mathcal{H}' + b_e'\mathcal{H} + (b_e-3)^2\mathcal{H}^2\right]\left[v^{(1)}\right]^2 + (b_e-3)\mathcal{H}v^{(1)}v^{(1)\prime}$$

$$+ 2(3 - b_e)\mathcal{H}v^{(1)}\delta_{g\mathrm{T}}^{(1)} - 2v^{(1)}\delta_{g\mathrm{T}}^{(1)\prime} + 3\,(b_e - 3)\,\mathcal{H}v^{(1)}\Phi^{(1)}\,. \tag{7.21}$$

All of the terms after $\delta_{g\mathrm{T}}^{(2)}$ on the right of equation (7.21) scale as $(\mathcal{H}/k)^n \left[\delta_{\mathrm{T}}^{(1)}\right]^2$, where $n = 2, 4$. Therefore they are omitted in the Newtonian approximation. These GR correction terms maintain gauge-independence on ultra-large scales, and they are included in the GR kernel (7.17).

7.4. Extracting the multipoles

Our goal is to extract the spherical harmonic multipoles of B_g with respect to the observer's line of sight. That is, for a fixed line of sight and triangle shape, the rotation of the plane of the triangle about $\boldsymbol{n}$ generates invariant moments, the sum of which add up to the full bispectrum. This means that

$$B_g = \sum_{\ell m} B_{\ell m} Y_{\ell m}(\boldsymbol{n})\,, \tag{7.22}$$

where we follow Scoccimarro et al. (1999); Nan et al. (2018) in our choice of decomposition of the bispectrum (an alternative basis can be found in Sugiyama et al. (2018)). To define the $B_{\ell m}$ we need to define an orientation for the $Y_{\ell m}$ to give the polar and azimuthal angles over which to integrate. We choose a coordinate basis for the vectors that span the triangle as follows:

$$\boldsymbol{k}_1 = (0, 0, k_1) \tag{7.23}$$

$$\boldsymbol{k}_2 = (0, k_2 \sin\theta, k_2 \cos\theta)\,, \tag{7.24}$$

$$\boldsymbol{k}_3 = (0, -k_2 \sin\theta, -k_1 - k_2\cos\theta)\,, \tag{7.25}$$

$$\boldsymbol{n} = (\sin\theta_1 \cos\varphi, \sin\theta_1 \sin\varphi, \cos\theta_1)\,. \tag{7.26}$$

That is, we fix $\boldsymbol{k}_1$ along the z-axis, and require the other triangle vectors to lie in the y-z plane, see figure 7.1 for a sketch of the relevant vectors. Then we define $\mu_1 = \cos\theta_1$ and use φ, which is the azimuthal angle giving the orientation of the triangle relative to $\boldsymbol{n}$. $\theta_{12} = \theta$ is the angle between vectors $\boldsymbol{k}_1$ and $\boldsymbol{k}_2$, and we define $\mu = \cos\theta = \hat{\boldsymbol{k}}_1 \cdot \hat{\boldsymbol{k}}_2$.

The bispectrum can then be expressed in terms of five variables, φ, μ_1, θ, k_1 and

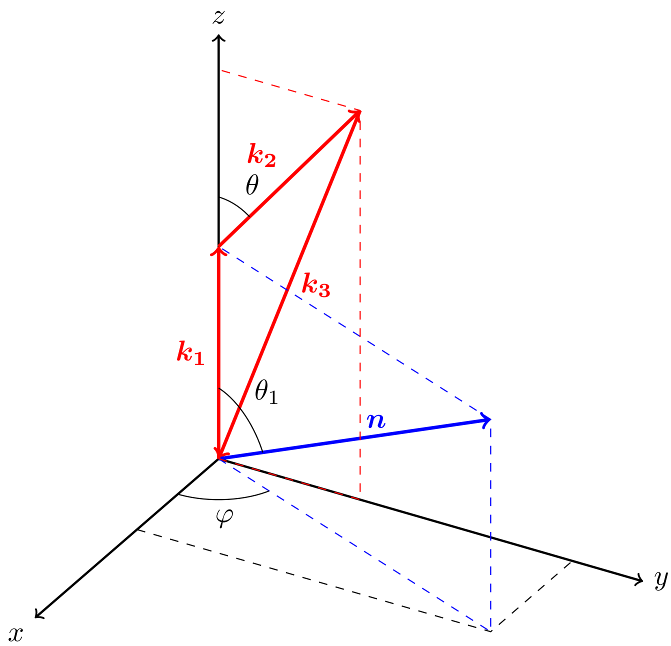

Figure 7.1.: Overview of the relevant vectors and angles for the Fourier-space bispectrum.

k_2, by using

$$\mu_2 = \sqrt{1-\mu_1^2}\sin\theta\sin\varphi + \mu_1\cos\theta\,, \tag{7.27}$$

$$\mu_3 = -\frac{k_1}{k_3}\mu_1 - \frac{k_2}{k_3}\mu_2. \tag{7.28}$$

Then

$$B_g(\theta, k_1, k_2, \mu_1, \varphi) = \sum_{\ell m} B_{\ell m}(\theta, k_1, k_2) Y_{\ell m}(\mu_1, \varphi)\,, \tag{7.29}$$

where we use standard orthonormal spherical harmonics,

$$Y_{\ell m}(\mu_1, \varphi) = \sqrt{\frac{2\ell+1}{4\pi}}\sqrt{\frac{(\ell-m)!}{(\ell+m)!}} P_\ell^m(\mu_1) e^{\mathrm{i}m\varphi}, \tag{7.30}$$

where the P_ℓ^m are the associated Legendre polynomials,

$$P_\ell^m(\mu_1) = \frac{(-1)^m}{2^\ell\,\ell!}(1-\mu_1^2)^{m/2}\frac{\mathrm{d}^{\ell+m}}{\mathrm{d}\mu_1^{\ell+m}}(\mu_1^2-1)^\ell. \tag{7.31}$$

At this stage we can extract the multipoles numerically once a bias model and cosmological parameters are given. It is actually significantly quicker to perform this extraction algebraically however, as we now explain.

The bispectrum in general can be considered as a function of $k_1, k_2, k_3, \mu, \mu_1, \mu_2, \mu_3$ and φ. An alternative to the expansion (7.29) is

$$B_g(\mu, k_1, k_2; \mu_1, \mu_2) = \sum_{a=0}^{6} \sum_{b=0}^{6} \mathcal{B}_{ab}(\mu, k_1, k_2)(\mathrm{i}\,\mu_1)^a (\mathrm{i}\,\mu_2)^b \,, \tag{7.32}$$

where we used μ_2 instead of φ and $a, b = 0 \ldots 6$, which is the maximum power of μ_1, μ_2 that can arise. This factors out all the angular dependence from the functions $\mathcal{B}_{ab}(\mu, k_1, k_2)$, where $\mu = \cos\theta$, which just depend on the triangle shape (and the cosmology). Note that by explicitly including factors of i in the sum, we have only real coefficients $\mathcal{B}_{ab}$. Schematically we can visualise $\mathcal{B}_{ab}$ in matrix form, split into Newtonian and relativistic contributions as (a bullet denotes a non-zero entry, open circles denote zero entries, and dots are non-existent entries; here that means $a + b > 8$ as higher powers don't occur):

$$\mathcal{B}_{ab} \sim \underbrace{\begin{pmatrix} \bullet & \circ & \bullet & \circ & \bullet & \circ & \circ \\ \circ & \bullet & \circ & \bullet & \circ & \bullet & \circ \\ \bullet & \circ & \bullet & \circ & \bullet & \circ & \bullet \\ \circ & \bullet & \circ & \bullet & \circ & \bullet & \cdot \\ \bullet & \circ & \bullet & \circ & \bullet & \cdot & \cdot \\ \circ & \bullet & \circ & \bullet & \cdot & \cdot & \cdot \\ \circ & \circ & \bullet & \cdot & \cdot & \cdot & \cdot \end{pmatrix}}_{\text{Newtonian}} + \underbrace{\begin{pmatrix} \bullet & \bullet & \bullet & \bullet & \bullet & \bullet & \bullet \\ \bullet & \bullet & \bullet & \bullet & \bullet & \bullet & \bullet \\ \bullet & \bullet & \bullet & \bullet & \bullet & \bullet & \circ \\ \bullet & \bullet & \bullet & \bullet & \bullet & \circ & \cdot \\ \bullet & \bullet & \bullet & \bullet & \circ & \cdot & \cdot \\ \bullet & \bullet & \bullet & \circ & \cdot & \cdot & \cdot \\ \bullet & \bullet & \circ & \cdot & \cdot & \cdot & \cdot \end{pmatrix}}_{\text{Relativistic}} . \tag{7.33}$$

(Note that the matrix row and column labelling start at $a, b = 0, 0$ for the top left element.) Thus, the Newtonian contributions always have $a + b = \text{even} \leq 8$, contributing only to the real part of B_g, while there are relativistic contributions present for all $a + b \leq 7$. When $a + b$ is odd, this implies an imaginary component to the full bispectrum.

In terms of the powers of $\mathcal{H}/k$ involved, we can visualise the maximum powers that appear in matrix form as follows:

$$\mathcal{B}_{ab} \sim \begin{pmatrix} k^{-8} & k^{-7} & k^{-6} & k^{-5} & k^{-4} & k^{-3} & k^{-2} \\ k^{-7} & k^{-6} & k^{-5} & k^{-4} & k^{-3} & k^{-2} & k^{-1} \\ k^{-6} & k^{-5} & k^{-4} & k^{-3} & k^{-2} & k^{-1} & k^{0} \\ k^{-5} & k^{-4} & k^{-3} & k^{-2} & k^{-1} & k^{0} & \cdot \\ k^{-4} & k^{-3} & k^{-2} & k^{-1} & k^{0} & \cdot & \cdot \\ k^{-3} & k^{-2} & k^{-1} & k^{0} & \cdot & \cdot & \cdot \\ k^{-2} & k^{-1} & k^{0} & \cdot & \cdot & \cdot & \cdot \end{pmatrix} . \tag{7.34}$$

As in the matrix (7.33), the matrix row and column labelling in (7.34) starts at $(a, b) = (0, 0)$. We see that higher powers n of $(\mathcal{H}/k)^n$ appear for lower $a + b$. Newtonian contributions are all $(\mathcal{H}/k)^0$. Each element has only odd powers of $\mathcal{H}/k$ if $a + b$ is odd, and similarly only even powers if $a + b$ is even.

The advantage of writing the bispectrum in this form is that we can derive analytic formulas for the multipoles. We need to find

$$\begin{aligned} B_{\ell m} &= \int \mathrm{d}\Omega \; B_g Y^*_{\ell m} \\ &= \sum_{a,b} \mathcal{B}_{ab} X^{ab}_{\ell m} \, , \end{aligned} \tag{7.35}$$

where

$$X^{ab}_{\ell m} = \int_0^{2\pi} \mathrm{d}\varphi \int_{-1}^{1} \mathrm{d}\mu_1 \, (\mathrm{i}\,\mu_1)^a (\mathrm{i}\,\mu_2)^b \, Y^*_{\ell m}(\mu_1, \varphi). \tag{7.36}$$

To do this we use the identity, derived in appendix REF APPENDIX WITH SUM DERIVATION, for $m \geq 0$,

$$\begin{aligned} X^{ab}_{\ell m} &= 2^{\ell+m-1} \mathrm{i}^{\,a+b+m} \sqrt{\frac{\pi(2\ell+1)(\ell-m)!}{(\ell+m)!}} \\ &\times \sum_{p=m}^{\frac{1}{2}(b+m)} \sum_{q=m}^{\ell} \frac{[1+(-1)^{a+b+q}]\, b! \, \cos^{b+m-2p}\theta \sin^{2p-m}\theta}{4^p (b+m-2p)!(\ell-q)!(p-m)!(q-m)!} \frac{\Gamma[\frac{1}{2}(q+\ell+1)]}{\Gamma[\frac{1}{2}(q-\ell+1)]} \frac{\Gamma[\frac{1}{2}(a+b+q-2p+ \ldots}{\Gamma[\frac{1}{2}(a+b+q+3)] \ldots} \end{aligned} \tag{7.37}$$

for $m \leq b$ and zero otherwise. For $m < 0$, the result follows a similar pattern, using the simple relation $X^{ab}_{\ell -m} = (-1)^{a+b+m} X^{ax`'b*}_{\ell m}$, see appendix REF DERIVATION SUM APPENDIX.

The resulting expressions for $B_{\ell m}$ are rather massive, in part because the cyclic permutations become mixed together, so we do not present them here. We can visualise these in matrix form split into their Newtonian and relativistic contributions:

$$B_{\ell m} = \underbrace{\begin{pmatrix} \bullet & \cdot & \cdot & \cdot & \cdot & \cdot & \cdot & \cdot & \cdot \\ \circ & \circ & \cdot & \cdot & \cdot & \cdot & \cdot & \cdot & \cdot \\ \bullet & \bullet & \bullet & \cdot & \cdot & \cdot & \cdot & \cdot & \cdot \\ \circ & \circ & \circ & \circ & \cdot & \cdot & \cdot & \cdot & \cdot \\ \bullet & \bullet & \bullet & \bullet & \bullet & \cdot & \cdot & \cdot & \cdot \\ \circ & \circ & \circ & \circ & \circ & \circ & \cdot & \cdot & \cdot \\ \bullet & \bullet & \bullet & \bullet & \bullet & \bullet & \bullet & \cdot & \cdot \\ \circ & \circ & \circ & \circ & \circ & \circ & \circ & \circ & \cdot \\ \bullet & \bullet & \bullet & \bullet & \bullet & \bullet & \bullet & \circ & \circ \end{pmatrix}}_{\text{Newtonian}} + \underbrace{\begin{pmatrix} \bullet & \cdot & \cdot & \cdot & \cdot & \cdot & \cdot & \cdot & \cdot \\ \bullet & \bullet & \cdot & \cdot & \cdot & \cdot & \cdot & \cdot & \cdot \\ \bullet & \bullet & \bullet & \cdot & \cdot & \cdot & \cdot & \cdot & \cdot \\ \bullet & \bullet & \bullet & \bullet & \cdot & \cdot & \cdot & \cdot & \cdot \\ \bullet & \bullet & \bullet & \bullet & \bullet & \cdot & \cdot & \cdot & \cdot \\ \bullet & \bullet & \bullet & \bullet & \bullet & \bullet & \cdot & \cdot & \cdot \\ \bullet & \bullet & \bullet & \bullet & \bullet & \bullet & \bullet & \cdot & \cdot \\ \bullet & \bullet & \bullet & \bullet & \bullet & \bullet & \bullet & \circ & \cdot \\ \circ & \circ & \circ & \circ & \circ & \circ & \circ & \circ & \circ \end{pmatrix}}_{\text{Relativistic}} . \tag{7.38}$$

Again, the matrix indices start at $(0, 0)$ in the top left, $(\ell, m) = (0, 0)$. In the matrix (7.38), consistent with previous matrix visualisations, a closed bullet represents a non-zero entry, while an open circle denotes a vanishing entry. The dots denote the non-existent elements of the matrix, here they are matrix elements where $m > \ell$ and hence do not exist. So, the Newtonian bispectrum only induces even multipoles up to and including $\ell = 8$, while the relativistic part induces even and odd multipoles up to $\ell = 7$ with multipoles higher than $\ell = 8$ vanishing exactly. Both the Newtonian and the relativistic part terminate at $m = \pm 6$, because $m \leq b \leq 6$, as can be seen from (7.37). Note that for $m < 0$ the pattern is the same. In terms of $(\mathcal{H}/k)$ powers, the highest that appear for each ℓ is $(\mathcal{H}/k)^{8-\ell}$, while the leading contribution is $(\mathcal{H}/k)^{0 \text{ or } 1}$ if the leading contribution is Newtonian or relativistic. These powers are even (odd) if ℓ is even (odd), as explained previously along with the visualisation of the powers $\mathcal{H}/k$ in equation (7.34).

Presentation of the matrix $\mathcal{B}_{ab}$

Here we describe in more detail how to calculate the matrix of coefficients $\mathcal{B}_{ab}$. These are far too large to write down, but most of the complexity comes from the k_i permutations and the fact that they are made irreducible from substituting for μ_3. However, the core part can be shown from which they can easily be calculated. First we note that once μ_3 is substituted for, we can write the first cyclic permutation of the product of the kernels as

$$\mathcal{K}_{123} = \mathcal{K}^{(1)}(k_1,\mu_1)\mathcal{K}^{(1)}(k_2,\mu_2)\mathcal{K}^{(2)}(k_1,k_2,k_3,\mu_1,\mu_2) = \sum_{a=0}^{5}\sum_{b=0}^{5}(\mathrm{i}\,\mu_1)^a(\mathrm{i}\,\mu_2)^b\mathcal{K}_{ab}(k_1,k_2,k_3)\,, \tag{7.39}$$

where $\mathcal{K}_{ab}(k_1,k_2,k_3) = \mathcal{K}_{ab}(k_2,k_1,k_3)$ is a set of real μ-independent coefficients which we give below, and here the maximum value of a, $b = 5$. Given $\mathcal{K}_{123}$ we can derive the permutations $\mathcal{K}_{321}$ and $\mathcal{K}_{312}$ as

$$\mathcal{K}_{321} = \sum_{a,b}\sum_{c=0}^{a}\binom{a}{c}\frac{k_1^{a-c}k_2^c}{k_3^a}(-1)^a(\mathrm{i}\,\mu_1)^{a-c}(\mathrm{i}\,\mu_2)^{b+c}\mathcal{K}_{ab}(k_3,k_2,k_1), \tag{7.40}$$

$$\mathcal{K}_{312} = \sum_{a,b}\sum_{c=0}^{a}\binom{a}{c}\frac{k_1^{a-c}k_2^c}{k_3^a}(-1)^a(\mathrm{i}\,\mu_1)^{a+b-c}(\mathrm{i}\,\mu_2)^{c}\mathcal{K}_{ab}(k_3,k_1,k_2), \tag{7.41}$$

where, as in general, the range of a, $b = 0\ldots6$. Given these, the full bispectrum is just $B_g = \mathcal{K}_{123}P_1P_2 + 2\,$permutations, but now explicitly written in terms of sums over powers of μ_1, μ_2. From this $\mathcal{B}_{ab}$ can be found by inspection. The difference in dimension between the permutations originates from the other cyclic permutations being added, where one substitutes $\mu_3 = -\left(k_1\mu_1 + k_2\mu_2\right)/k_3$. In (7.40) the largest power of μ_2 is 6, and (7.41) has the largest power of μ_1 as 6.

To present $\mathcal{K}_{ab}(k_1,k_2,k_3)$ we will show powers of $\mathcal{H}/k$ separately, and write $\mathcal{K}_{ab}(k_1,k_2,k_3) = \sum_{n=0}^{8}\mathcal{K}_{ab}^{(n)}(k_1,k_2,k_3)$ where n represents the power of $\mathcal{H}/k$. Then the Newtonian and leading GR correction part look like (again, a bullet denotes a non-zero entry)

$$\mathcal{K}_{ab}^{(0)} = \begin{pmatrix} \bullet & \circ & \bullet & \circ & \bullet & \circ \\ \circ & \bullet & \circ & \bullet & \circ & \bullet \\ \bullet & \circ & \bullet & \circ & \bullet & \circ \\ \circ & \bullet & \circ & \bullet & \circ & \bullet \\ \bullet & \circ & \bullet & \circ & \bullet & \circ \\ \circ & \bullet & \circ & \bullet & \circ & \circ \end{pmatrix} \qquad \mathcal{K}_{ab}^{(1)} = \begin{pmatrix} \circ & \bullet & \circ & \bullet & \circ & \bullet \\ \bullet & \circ & \bullet & \circ & \bullet & \circ \\ \circ & \bullet & \circ & \bullet & \circ & \bullet \\ \bullet & \circ & \bullet & \circ & \bullet & \circ \\ \circ & \bullet & \circ & \bullet & \circ & \circ \\ \bullet & \circ & \bullet & \circ & \circ & \circ \end{pmatrix} \tag{7.42}$$

where, writing $F = F_2(\boldsymbol{k}_1,\boldsymbol{k}_2)$, $G = G_2(\boldsymbol{k}_1,\boldsymbol{k}_2)$, $S = S_2(\boldsymbol{k}_1,\boldsymbol{k}_2)$,

$$\mathcal{K}_{00}^{(0)} = b_1^2\left(b_{s^2}S + b_2\right) + Fb_1^3 \tag{7.43}$$

$$\mathcal{K}_{02}^{(0)} = -b_1 f\left[b_1^2 + b_{s^2}S + b_2 + \left(F + \frac{Gk_2^2}{k_3^2}\right)b_1\right] \tag{7.44}$$

$$\mathcal{K}_{04}^{(0)} = b_1 f^2\left(\frac{Gk_2^2}{k_3^2} + b_1\right) \tag{7.45}$$

$$\mathcal{K}_{11}^{(0)} = -b_1^2 f \left[\frac{\left(k_1^2+k_2^2\right) b_1}{k_1 k_2} + \frac{2Gk_1k_2}{k_3^2}\right] \tag{7.46}$$

$$\mathcal{K}_{13}^{(0)} = b_1 f^2 \left[\frac{\left(k_1^2+2k_2^2\right) b_1}{k_1 k_2} + \frac{2Gk_1k_2}{k_3^2}\right] \tag{7.47}$$

$$\mathcal{K}_{15}^{(0)} = -\frac{b_1 f^3 k_2}{k_1} \tag{7.48}$$

$$\mathcal{K}_{20}^{(0)} = -b_1 f \left[b_1^2 + b_{s^2} S + b_2 + \left(F + \frac{Gk_1^2}{k_3^2}\right) b_1\right] \tag{7.49}$$

$$\mathcal{K}_{22}^{(0)} = f^2 \left[4b_1^2 + b_{s^2} S + b_2 + \left(F + \frac{G\left(k_1^2+k_2^2\right)}{k_3^2}\right) b_1\right] \tag{7.50}$$

$$\mathcal{K}_{24}^{(0)} = -f^3 \left(\frac{Gk_2^2}{k_3^2} + 3b_1\right) \tag{7.51}$$

$$\mathcal{K}_{31}^{(0)} = b_1 f^2 \left[\frac{b_1\left(2k_1^2+k_2^2\right)}{k_1 k_2} + \frac{2Gk_1k_2}{k_3^2}\right] \tag{7.52}$$

$$\mathcal{K}_{33}^{(0)} = -f^3 \left[\frac{2b_1\left(k_1^2+k_2^2\right)}{k_1 k_2} + \frac{2Gk_1k_2}{k_3^2}\right] \tag{7.53}$$

$$\mathcal{K}_{35}^{(0)} = \frac{f^4 k_2}{k_1} \tag{7.54}$$

$$\mathcal{K}_{40}^{(0)} = b_1 f^2 \left(b_1 + \frac{Gk_1^2}{k_3^2}\right) \tag{7.55}$$

$$\mathcal{K}_{42}^{(0)} = -f^3 \left(3b_1 + \frac{Gk_1^2}{k_3^2}\right) \tag{7.56}$$

$$\mathcal{K}_{44}^{(0)} = 2f^4 \tag{7.57}$$

$$\mathcal{K}_{51}^{(0)} = -\frac{b_1 f^3 k_1}{k_2} \tag{7.58}$$

$$\mathcal{K}_{53}^{(0)} = \frac{f^4 k_1}{k_2}. \tag{7.59}$$

Similarly, the leading GR correction $\mathcal{O}(\mathcal{H}/k)$ coefficients are,

$$\mathcal{K}_{01}^{(1)} = b_1\gamma_1 \frac{\left(b_2 + b_{s^2} S\right)}{k_2} + b_1^2 \left(\frac{F\gamma_1 + \beta_{16}}{k_2} + \frac{\beta_{15}\mu}{k_1} + \frac{\beta_{14} k_2}{k_1^2} - \frac{\beta_{19} G k_2}{k_3^2}\right) \tag{7.60}$$

$$\mathcal{K}_{03}^{(1)} = b_1 f \left[\frac{\left(\beta_{19} - \gamma_1\right) G k_2}{k_3^2} - \frac{\beta_{16}}{k_2} - \frac{\beta_{15}\mu}{k_1} - \frac{\beta_{14} k_2}{k_1^2}\right] - b_1^2 \left(\frac{f\gamma_1}{k_2} + \frac{\beta_{17} k_2}{k_1^2}\right) \tag{7.61}$$

$$\mathcal{K}_{05}^{(1)} = \frac{b_1 f \beta_{17} k_2}{k_1^2} \tag{7.62}$$

$$\mathcal{K}_{10}^{(1)} = b_1\gamma_1 \frac{\left(b_2 + b_{s^2} S\right)}{k_1} + b_1^2 \left[\left(-\frac{G\beta_{19}}{k_3^2} + \frac{\beta_{14}}{k_2^2}\right) k_1 + \frac{\beta_{15}\mu}{k_2} + \frac{F\gamma_1 + \beta_{16}}{k_1}\right] \tag{7.63}$$

$$\mathcal{K}_{12}^{(1)} = -\gamma_1 f \frac{\left(b_{s^2} S + b_2\right)}{k_1} - b_1^2 \left[\gamma_1 f \left(\frac{k_1}{k_2^2} + \frac{2}{k_1}\right) + \frac{\beta_{18}}{k_1}\right] \tag{7.64}$$

$$+ b_1 f \left\{ \left[\left(-\frac{2k_1}{k_3^2} - \frac{k_2^2}{k_1 k_3^2} \right) \gamma_1 + \frac{k_1 \beta_{19}}{k_3^2} \right] G - \frac{F\gamma_1}{k_1} - \frac{\beta_{14} k_1}{k_2^2} - \frac{\beta_{15}\mu}{k_2} - \frac{\beta_{16}}{k_1} \right\} \tag{7.65}$$

$$\mathcal{K}_{14}^{(1)} = b_1 f \frac{2\gamma_1 f + \beta_{18}}{k_1} + \frac{G k_2^2 \gamma_1 f^2}{k_1 k_3^2} \tag{7.66}$$

$$\mathcal{K}_{21}^{(1)} = -\gamma_1 f \frac{(b_{s^2} S + b_2)}{k_2} - b_1^2 \left[\gamma_1 f \left(\frac{2}{k_2} + \frac{k_2}{k_1^2} \right) + \frac{\beta_{18}}{k_2} \right] \tag{7.67}$$

$$+ b_1 f \left\{ \left[\left(-\frac{k_1^2}{k_2 k_3^2} - \frac{2k_2}{k_3^2} \right) \gamma_1 + \frac{k_2 \beta_{19}}{k_3^2} \right] G - \frac{F\gamma_1}{k_2} - \frac{\beta_{16}}{k_2} - \beta_{14} \left(\frac{\mu}{k_1} + \frac{k_2}{k_1^2} \right) \right\} \tag{7.68}$$

$$\mathcal{K}_{23}^{(1)} = b_1 f \left[\left(\frac{4}{k_2} + \frac{2k_2}{k_1^2} \right) \gamma_1 f + \frac{\beta_{18}}{k_2} + \frac{\beta_{17} k_2}{k_1^2} \right] + f^2 \left[G \left(3\gamma_1 - \beta_{19} \right) \frac{k_2}{k_3^2} + \frac{\beta_{16}}{k_2} + \frac{\beta_{15}\mu}{k_1} + \frac{\beta_{14} k_2}{k_1^2} \right] \tag{7.69}$$

$$\mathcal{K}_{25}^{(1)} = -f^2 (\gamma_1 f + \beta_{17}) \frac{k_2}{k_1^2} \tag{7.70}$$

$$\mathcal{K}_{30}^{(1)} = -b_1^2 \left(\frac{f\gamma_1}{k_1} + \frac{\beta_{17} k_1}{k_2^2} \right) + b_1 f \left[G \left(-\gamma_1 + \beta_{19} \right) \frac{k_1}{k_3^2} - \frac{\beta_{14} k_1}{k_2^2} - \frac{\beta_{15}\mu}{k_2} - \frac{\beta_{16}}{k_1} \right] \tag{7.71}$$

$$\mathcal{K}_{32}^{(1)} = b_1 f \left[\left(\frac{2k_1}{k_2^2} + \frac{4}{k_1} \right) \gamma_1 f + \frac{\beta_{17} k_1}{k_2^2} + \frac{\beta_{18}}{k_1} \right] + f^2 \left[G \left(3\gamma_1 - \beta_{19} \right) \frac{k_1}{k_3^2} + \frac{\beta_{14} k_1}{k_2^2} + \frac{\beta_{15}\mu}{k_2} + \frac{\beta_{16}}{k_1} \right] \tag{7.72}$$

$$\mathcal{K}_{34}^{(1)} = -\frac{f^2 \left(3f\gamma_1 + \beta_{18} \right)}{k_1} \tag{7.73}$$

$$\mathcal{K}_{41}^{(1)} = b_1 f \frac{(2\gamma_1 f + \beta_{18})}{k_2} + \frac{G \gamma_1 f^2 k_1^2}{k_2 k_3^2} \tag{7.74}$$

$$\mathcal{K}_{43}^{(1)} = -\frac{f^2 \left(3f\gamma_1 + \beta_{18} \right)}{k_2} \tag{7.75}$$

$$\mathcal{K}_{50}^{(1)} = \frac{b_1 \beta_{17} f k_1}{k_2^2} \tag{7.76}$$

$$\mathcal{K}_{52}^{(1)} = -\frac{f^2 k_1 \left(f\gamma_1 + \beta_{17} \right)}{k_2^2} \,. \tag{7.77}$$

The remaining matrices are of the form

$$\mathcal{K}_{ab}^{(2)} = \begin{pmatrix} \bullet & \circ & \bullet & \circ & \bullet & \circ \\ \circ & \bullet & \circ & \bullet & \circ & \bullet \\ \bullet & \circ & \bullet & \circ & \bullet & \circ \\ \circ & \bullet & \circ & \bullet & \circ & \circ \\ \bullet & \circ & \bullet & \circ & \circ & \circ \\ \circ & \bullet & \circ & \circ & \circ & \circ \end{pmatrix} \quad \mathcal{K}_{ab}^{(3)} = \begin{pmatrix} \circ & \bullet & \circ & \bullet & \circ & \bullet \\ \bullet & \circ & \bullet & \circ & \bullet & \circ \\ \circ & \bullet & \circ & \bullet & \circ & \circ \\ \bullet & \circ & \bullet & \circ & \circ & \circ \\ \circ & \bullet & \circ & \circ & \circ & \circ \\ \bullet & \circ & \circ & \circ & \circ & \circ \end{pmatrix} \quad \mathcal{K}_{ab}^{(4)} = \begin{pmatrix} \bullet & \circ & \bullet & \circ & \bullet & \circ \\ \circ & \bullet & \circ & \bullet & \circ & \circ \\ \bullet & \circ & \bullet & \circ & \circ & \circ \\ \circ & \bullet & \circ & \circ & \circ & \circ \\ \bullet & \circ & \circ & \circ & \circ & \circ \\ \circ & \circ & \circ & \circ & \circ & \circ \end{pmatrix}$$

$$\mathcal{K}_{ab}^{(6)} = \begin{pmatrix} \bullet & \circ & \bullet & \circ & \circ & \circ \\ \circ & \bullet & \circ & \circ & \circ & \circ \\ \bullet & \circ & \circ & \circ & \circ & \circ \\ \circ & \circ & \circ & \circ & \circ & \circ \\ \circ & \circ & \circ & \circ & \circ & \circ \\ \circ & \circ & \circ & \circ & \circ & \circ \end{pmatrix} \quad \mathcal{K}_{ab}^{(7)} = \begin{pmatrix} \circ & \bullet & \circ & \circ & \circ & \circ \\ \bullet & \circ & \circ & \circ & \circ & \circ \\ \circ & \circ & \circ & \circ & \circ & \circ \\ \circ & \circ & \circ & \circ & \circ & \circ \\ \circ & \circ & \circ & \circ & \circ & \circ \\ \circ & \circ & \circ & \circ & \circ & \circ \end{pmatrix} \quad \mathcal{K}_{ab}^{(8)} = \begin{pmatrix} \bullet & \circ & \circ & \circ & \circ & \circ \\ \circ & \circ & \circ & \circ & \circ & \circ \\ \circ & \circ & \circ & \circ & \circ & \circ \\ \circ & \circ & \circ & \circ & \circ & \circ \\ \circ & \circ & \circ & \circ & \circ & \circ \\ \circ & \circ & \circ & \circ & \circ & \circ \end{pmatrix} \tag{7.78}$$

Their coefficients are extracted in similar fashion, and can be found in full in appendix REF APPENDIX Kab COEFF

7.5. Analysis

Here we present an analysis of the behaviour of the multipoles.

Co-linear, squeezed and equilateral limits

To help understand further the multipoles we can evaluate their equilateral ($k_1 = k_2 = k_3$), co-linear ($\theta = 0$ or $\theta = \pi$) and squeezed limits analytically. Non-zero co-linear multipoles exist only for $m = 0$ components. This is the one limit that is easy to evaluate by hand – it follows directly from (7.37). The equilateral case is significantly more complicated to evaluate. Non-zero equilateral multipoles exist for all even m, for any ℓ, the one exception being the $m = 0$ part of the dipole, for which the equilateral configuration is identically zero. These are summarised in Fig. 7.2, together with the powers of k which appear in each multipole.

The squeezed limit was explicitly evaluated in Clarkson et al. (2019) for the leading $\mathcal{O}(\mathcal{H}/k_L)$ contribution, where k_L is the long mode, which we expand further here. Note that in what follows, we have assumed that the small-scale modes are sufficiently sub-equality scale, and that the large-scale modes are larger than the equality scale. The leading corrections in the even multipoles require us going beyond leading order $\mathcal{O}(\mathcal{H}/k_L)$ in the squeezed limit. We let

$$k_1 = k_2 = k_S, \quad k_3 = \epsilon k_S \,, \tag{7.79}$$

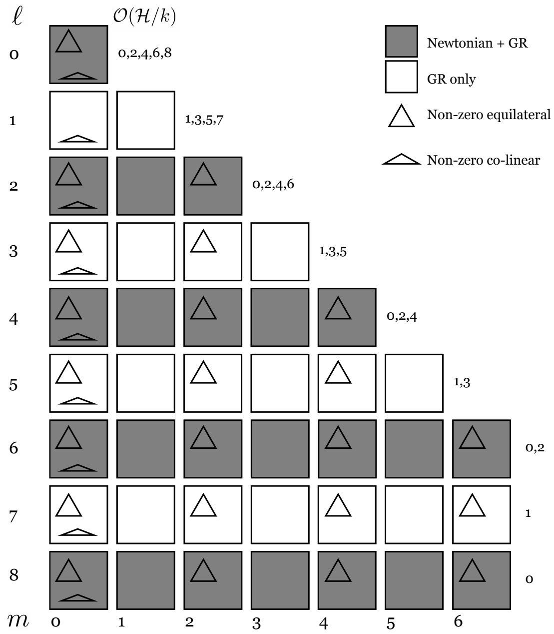

Figure 7.2.: Overview of all non-zero multipoles for the bispectrum, which includes ℓ from 0 to 8, and m from $-\ell$ to ℓ; the pattern here is the same for $m < 0$, so only $m \geq 0$ are displayed. Denoted in the figure are whether components are Newtonian+GR or GR only, triangle shapes indicating whether given components are non-vanishing in flattened (co-linear) or equilateral limits. Note how the dipole is unique in having the equilateral case vanish for every value of m. Also given is which powers of $\mathcal{H}/k$ appear in each of the multipoles.

to write the wavenumber in terms of the short mode $k_S \gg k_L$, which implies

$$\mu = -1 + \frac{\epsilon^2}{2} \,. \tag{7.80}$$

We then take the limit as $\epsilon \to 0$ with the short mode k_S fixed, and keep only the leading terms in $\mathcal{H}/k_L$, neglecting factors of $\mathcal{H}/k_S$ and $P(k_S)^2$. For each multipole we are then left with the squeezed limit as a polynomial in $\mathcal{H}/k_L$. The leading contributions are:

$$
\underbrace{\left(\frac{\mathcal{H}}{k_L}\right)^0
\begin{pmatrix}
\bullet & \cdot & \cdot & \cdot & \cdot & \cdot & \cdot & \cdot & \cdot \\
\circ & \circ & \cdot & \cdot & \cdot & \cdot & \cdot & \cdot & \cdot \\
\bullet & \circ & \bullet & \cdot & \cdot & \cdot & \cdot & \cdot & \cdot \\
\circ & \circ & \circ & \circ & \cdot & \cdot & \cdot & \cdot & \cdot \\
\bullet & \circ & \bullet & \circ & \bullet & \cdot & \cdot & \cdot & \cdot \\
\circ & \circ & \circ & \circ & \circ & \circ & \cdot & \cdot & \cdot \\
\bullet & \circ & \bullet & \circ & \bullet & \circ & \circ & \cdot & \cdot \\
\circ & \circ & \circ & \circ & \circ & \circ & \circ & \circ & \cdot \\
\bullet & \circ & \bullet & \circ & \bullet & \circ & \circ & \circ & \circ
\end{pmatrix}}_{\text{Newtonian part}}
+
\underbrace{\left(\frac{\mathcal{H}}{k_L}\right)^1
\begin{pmatrix}
\circ & \cdot & \cdot & \cdot & \cdot & \cdot & \cdot & \cdot & \cdot \\
\circ & \bullet & \cdot & \cdot & \cdot & \cdot & \cdot & \cdot & \cdot \\
\circ & \circ & \circ & \cdot & \cdot & \cdot & \cdot & \cdot & \cdot \\
\circ & \bullet & \circ & \bullet & \cdot & \cdot & \cdot & \cdot & \cdot \\
\circ & \circ & \circ & \circ & \circ & \cdot & \cdot & \cdot & \cdot \\
\circ & \bullet & \circ & \bullet & \circ & \circ & \cdot & \cdot & \cdot \\
\circ & \circ & \circ & \circ & \circ & \circ & \circ & \cdot & \cdot \\
\circ & \bullet & \circ & \bullet & \circ & \circ & \circ & \circ & \cdot \\
\circ & \circ & \circ & \circ & \circ & \circ & \circ & \circ & \circ
\end{pmatrix}
+ \left(\frac{\mathcal{H}}{k_L}\right)^2}_{\text{GR contributions}}
\tag{7.81}
$$

Here, the matrices represent the ℓ, m values from $\ell = 0, m = 0$ (top left entry). We see that the Newtonian part has non-zero squeezed limits for some even m, terminating at $m = 4$. GR corrections come in up to $m = 3$ for $\ell \leq 7$. For odd m these contributions come in for the leading terms $\mathcal{O}(\mathcal{H}/k)$, while for m even the order is lower, $\mathcal{O}((\mathcal{H}/k)^2)$. Note that we assume primordial Gaussianity. In the presence of primordial non-Gaussianity, the squeezed limit has higher powers of $\mathcal{H}/k$. Current work investigates how primordial non-Gaussianity will change our results. The effect of local primordial non-Gaussianity on the Newtonian galaxy bispectrum is presented in Umeh et al. (2017).

Numerical results

Here we present a numerical analysis of the multipoles of the galaxy bispectrum. We use three different survey models, two of which are appropriate for future surveys; i.e. SKA HI intensity mapping, and a Stage IV $H\alpha$ spectroscopic galaxy survey similar to Euclid. The third model we consider is a simplified 'toy model' for illustrative purposes. The parameters we use are introduced below.

Evolution and magnification bias are defined as Alonso et al. (2015),

$$
b_e = -\frac{\partial \ln n_g}{\partial \ln(1+z)}, \quad \mathcal{Q} = -\frac{\partial \ln n_g}{\partial \ln L}\bigg|_c, \tag{7.82}
$$

where n_g is the comoving galaxy number density, L the luminosity, and $|_c$ denotes evaluation at the flux cut.

For an HI intensity mapping survey, we estimate the bias from the halo model following Umeh et al. (2016). This yields the following fitting formulae for first and second order bias,

$$b_1^{\mathrm{HI}}(z) = 0.754 + 0.0877z + 0.0607z^2 - 0.00274z^3\,, \tag{7.83}$$

$$b_2^{\mathrm{HI}}(z) = -0.308 - 0.0724z - 0.0534z^2 + 0.0247z^3\,. \tag{7.84}$$

For the tidal bias, we assume zero initial tidal bias which relates b_{s^2} to b_1 as,

$$b_{s^2}^{\mathrm{HI}}(z) = -\frac{4}{7}(b_1(z) - 1), \tag{7.85}$$

so that,

$$b_{s^2}^{\mathrm{HI}}(z) = 0.141 - 0.0501z - 0.0347z^2 + 0.00157z^3. \tag{7.86}$$

The HI intensity mapping evolution bias is given by the background HI brightness temperature Fonseca et al. (2018),

$$b_e^{\mathrm{HI}}(z) = -\frac{\mathrm{d}\ln\left[(1+z)^{-1}\mathcal{H}\bar{T}_{\mathrm{HI}}\right]}{\mathrm{d}\ln\left[1+z\right]}\,, \tag{7.87}$$

where $\bar{T}_{\mathrm{HI}}$ is given by the fitting formula,

$$\bar{T}_{\mathrm{HI}}(z) = (5.5919 + 23.242z - 2.4136z^2) \times 10^{-2}\,\mathrm{mK}. \tag{7.88}$$

The effective magnification bias for HI intensity mapping is Fonseca et al. (2018)

$$\mathcal{Q}^{\mathrm{HI}} = 1.0\,, \tag{7.89}$$

and clustering bias is independent of luminosity,

$$\frac{\partial b_1^{\mathrm{HI}}}{\partial \ln L} = 0\,. \tag{7.90}$$

We consider a Stage IV $H\alpha$ spectroscopic survey similar to Euclid, and use the clustering biases given in Maartens et al. (2020),

$$b_1^{H\alpha}(z) = 0.9 + 0.4z, \tag{7.91}$$

$$b_2^{H\alpha}(z) = -0.741 - 0.125z + 0.123z^2 + 0.00637z^3, \tag{7.92}$$

$$b_{s^2}^{H\alpha}(z) = 0.0409 - 0.199z - 0.0166z^2 + 0.00268z^3. \tag{7.93}$$

The magnification bias and evolution bias are Maartens et al. (2020),

$$\mathcal{Q}^{H\alpha}(z) = \frac{y_c(z)^{\alpha+1}\exp\left[-y_c(z)\right]}{\Gamma(\alpha+1, y_c(z))}, \tag{7.94}$$

$$b_e^{H\alpha}(z) = -\frac{\mathrm{d}\ln\Phi_*(z)}{\mathrm{d}\ln(1+z)} + \frac{\mathrm{d}\ln y_c(z)}{\mathrm{d}\ln(1+z)}\mathcal{Q}^{H\alpha}(z)\,, \tag{7.95}$$

where $\alpha = -1.35$, Γ is the upper incomplete gamma function, Φ_* is given in Maartens et al. (2020) and $y_c(z) = \left[\chi(z)/\left(2.97h\times10^3\right)(\mathrm{Mpc}/h)\right]^2$. Table 1 in Maartens et al. (2020) summarises the numerical values of the bias parameters discussed above. Finally, we follow Maartens et al. (2020) and take

$$\left.\frac{\partial b_1^{H\alpha}}{\partial\ln L}\right|_{\mathrm{c}} = 0\,. \tag{7.96}$$

For the simple model of galaxy bias, we use

$$b_1(z) = \sqrt{1+z}, \tag{7.97}$$

$$b_2(z) = -0.3\sqrt{1+z}, \tag{7.98}$$

$$b_{s^2}(z) = -\frac{4}{7}(b_1(z)-1), \tag{7.99}$$

$$b_e = 0, \tag{7.100}$$

$$\mathcal{Q} = 0. \tag{7.101}$$

For cosmological parameters we use Planck 2018 Aghanim et al. (2018), giving the best-fit parameters $h = 0.6766$, $\Omega_{m0} = 0.3111$, $\Omega_{b0}h^2 = 0.02242$, $\Omega_{c0}h^2 = 0.11933$, $n_s = 0.9665$, $\gamma = \ln f/\ln\Omega_m = 0.545$. The linear matter power spectrum is calculated using CAMB Lewis et al. (2000).

We examine numerically three different triangular configurations, the squeezed, co-linear, and equilateral triangles, as a function of triangle size. For our numerical analysis, we choose a moderately squeezed triangle shape with $\theta \approx 178°$, which corresponds to $k_3 = k$, $k_1 = k_2 = 28k$ (such that long mode k_3 is the reference wavevector, and the other vectors are defined in relation to the long mode). For the co-linear case, we use flattened isosceles triangles with $\theta \approx 2.3°$, corresponding to $k_3 = k$, $k_1 = k_2 = 0.5001k$. All plots are at redshift $z = 1$, with the exception of figure 7.9, where we look at the amplitude as a function of redshift.

Firstly, we consider the total amplitude of the different multipoles with respect to the

Newtonian monopole, plotting the total power contained in each of the multipoles and normalising by the Newtonian monopole of the galaxy bispectrum,

$$b_\ell(k_1, k_2, \theta) = \frac{1}{B_{\mathrm{N},00}(k_1, k_2, \theta)} \sqrt{\frac{1}{2\ell + 1} \sum_{m=-\ell}^{\ell} |B_{\ell m}(k_1, k_2, \theta)|^2}. \tag{7.102}$$

We present this for all multipoles $\ell = 0 \dots 8$ and separately for each of the triangle shapes introduced above (i.e. fixing triangle shape, and varying size by varying k), as well as for both bias models which are relevant for future surveys. The results can be viewed in figures 7.3, 7.4 and 7.5.

We have created colour-intensity plots to give an overview of the relative amplitudes of the first few multipoles of the galaxy bispectrum, $\ell = 0 \dots 3$. Because of the simple relationship between $B_{\ell,m}$ and $B_{\ell,-m}$, we do not show plots for negative m. These as well are done for both HI intensity mapping bias and $H\alpha$ bias. The results are shown in figures 7.6 and 7.7 for the Euclid-like survey and for SKA intensity mapping respectively.

To further investigate the dependence on triangle shape we investigate the reduced bispectrum. We define the reduced bispectrum as

$$Q_{\ell m}(k_1, k_2, \theta) = \frac{B_{\ell m}(k_1, k_2, \theta)}{P_0(k_1)P_0(k_2) + P_0(k_2)P_0(k_3) + P_0(k_1)P_0(k_3)}, \tag{7.103}$$

where P_0 is the monopole of the galaxy power spectrum,

$$P_0(k) = \frac{1}{2} \int_{-1}^{1} \mathrm{d}\mu \, P_g(\boldsymbol{k}), \tag{7.104}$$

with the galaxy power spectrum $P_g(\boldsymbol{k}) = (b_1 + f\mu^2)^2 P$, P being the linear dark matter power spectrum. (An alternative definition would be to use the relativistic galaxy power spectrum which would induce small changes $O((\mathcal{H}/k)^2)$ on Hubble scales.) The reduced bispectrum Q is hence dependent on magnitude of wavevectors $\boldsymbol{k}_1$ and $\boldsymbol{k}_2$, and the angle between these $(\pi - \theta)$. We fix $k_1 = 0.1\,\mathrm{Mpc}^{-1}$ and $k_1 = 0.01\,\mathrm{Mpc}^{-1}$, and use differently coloured lines to indicate the ratio of k_2/k_1, which ranges from isosceles triangles in which $k_1 = k_2$, to $k_2/k_1 = 4.5$. The angle θ ranges from $[0, \pi]$, except for the isosceles shape, for which we stop at $\theta = \pi - 0.01$ (for $k_1 = 0.1\,\mathrm{Mpc}^{-1}$), and at $\theta = \pi - 0.02$ (for $k_1 = 0.01\,\mathrm{Mpc}^{-1}$). The reason for this is the inclusion of relativistic $\mathcal{H}/k$ contributions, which cause unobservable divergences as $k \to 0$, occurring here for the isosceles shape when the angle between

$\boldsymbol{k}_1$ and $\boldsymbol{k}_2$ goes to π and $k_3 \to 0$.

The bias used is again that for the Euclid-like $H\alpha$ spectroscopic survey. Results are in figure 7.8. The layout is similar to figures 7.6 and 7.7, with $\ell = 0 \ldots 3$ plotted. Once again, negative m are not shown.

Lastly, we fix triangle shape and size, and plot the relative total power (as defined in (7.102)) as a function of redshift, where redshift ranges from $z = 0.1 \ldots 2.0$. This is done for the toy model for bias only. The three panels in figure 7.9 show the results for $\ell = 0 \ldots 3$, for each of the three wavevector triangles discussed earlier; equilateral, squeezed and flattened shapes. Solid and dashed lines indicate the relative total power for $k_1 = 0.1\,\mathrm{Mpc}^{-1}$ and $k_1 = 0.01\,\mathrm{Mpc}^{-1}$ respectively.

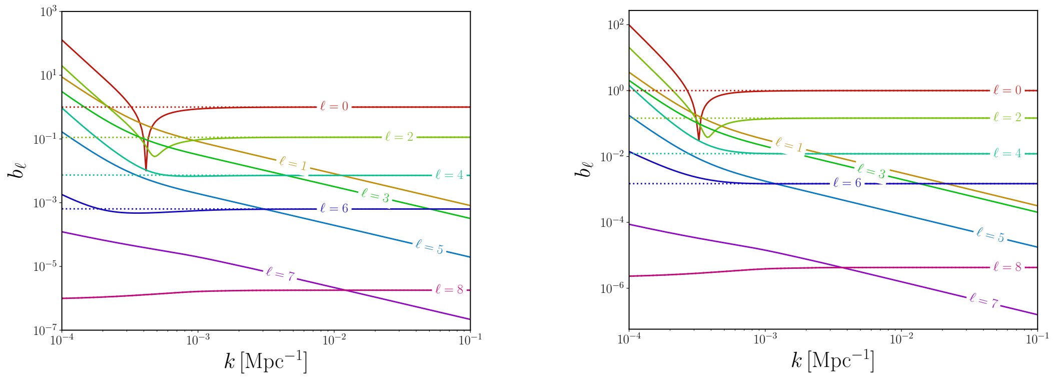

Figure 7.3.: Normalised total power for squeezed configuration for Euclid-like (left) and SKA HI intensity mapping (right) surveys. Long mode k_3 is plotted along the x-axis.

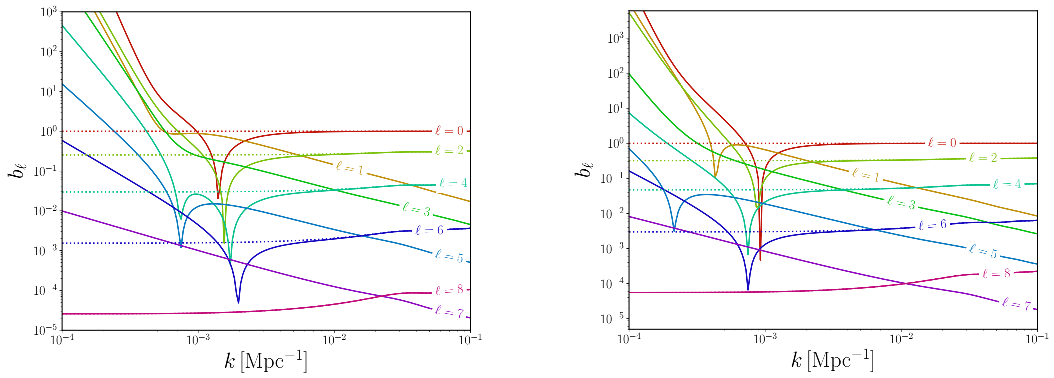

Figure 7.4.: Total power for flattened configuration for Euclid-like (left) and SKA HI intensity mapping (right) surveys. Long mode k_3 is plotted along the x-axis.

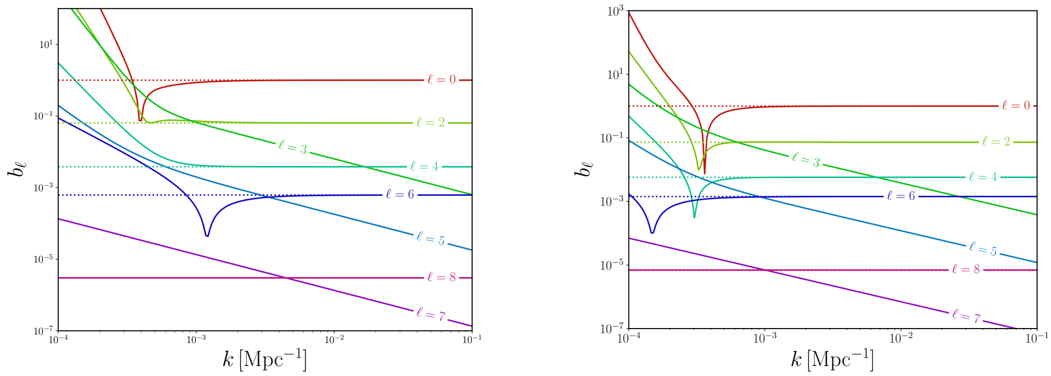

Figure 7.5.: Total power for equilateral configuration for Euclid-like (left) and SKA HI intensity mapping (right) surveys. Since the dipole vanishes in this limit, the $\ell = 1$ line is absent.

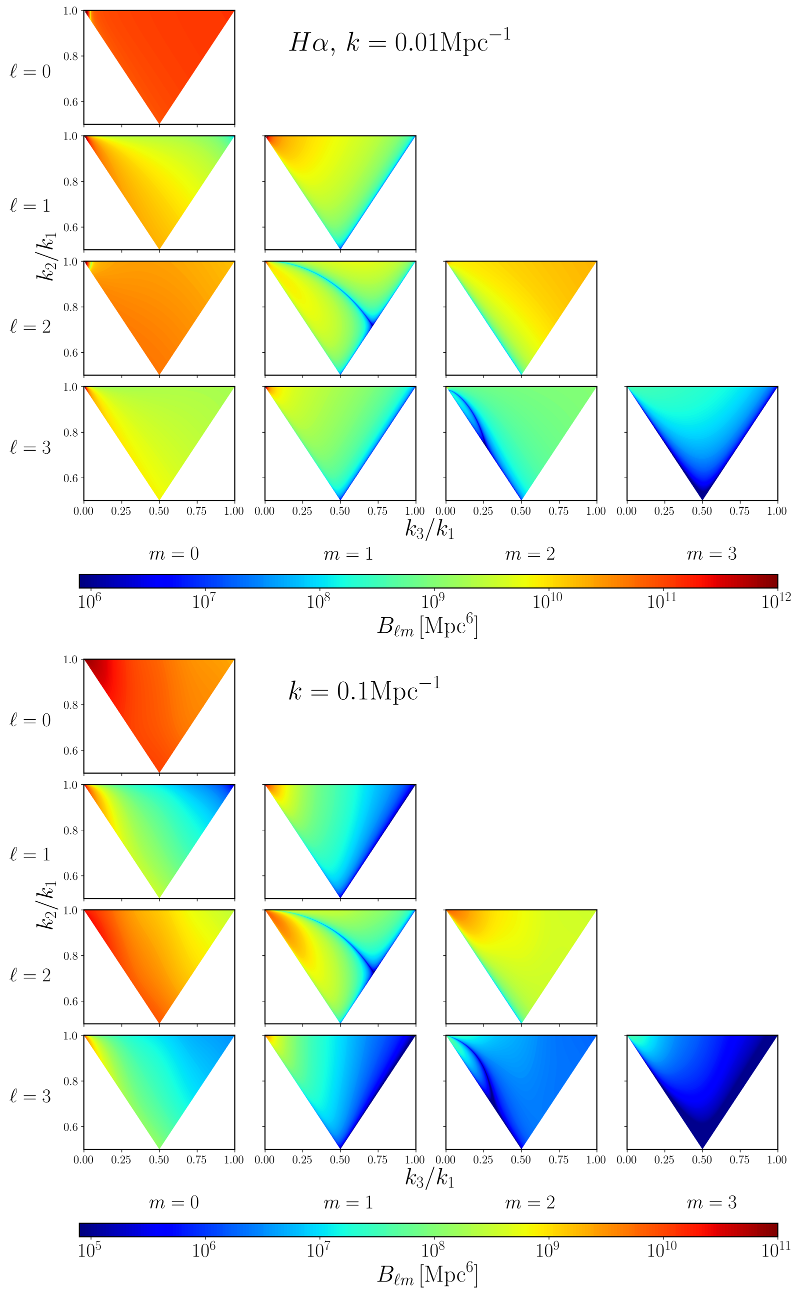

Figure 7.6.: A selection of multipoles of the galaxy bispectrum, $B_{\ell m}$, with $\ell = 0 \ldots 3$ and $m = 0 \ldots \ell$ as indicated in the figure. Bias model used is that for $H\alpha$/Euclid-like survey. k_1 is kept fixed, the value of which is given alongside the plot, and the x and y axes vary respectively k_3 and k_2 with respect to the fixed k_1. The upper left corner of the wedge shape is the squeezed limit, the upper right corner is the equilateral configuration, and the lower corner is the co-linear configuration. Note the difference in range of the colour bars.

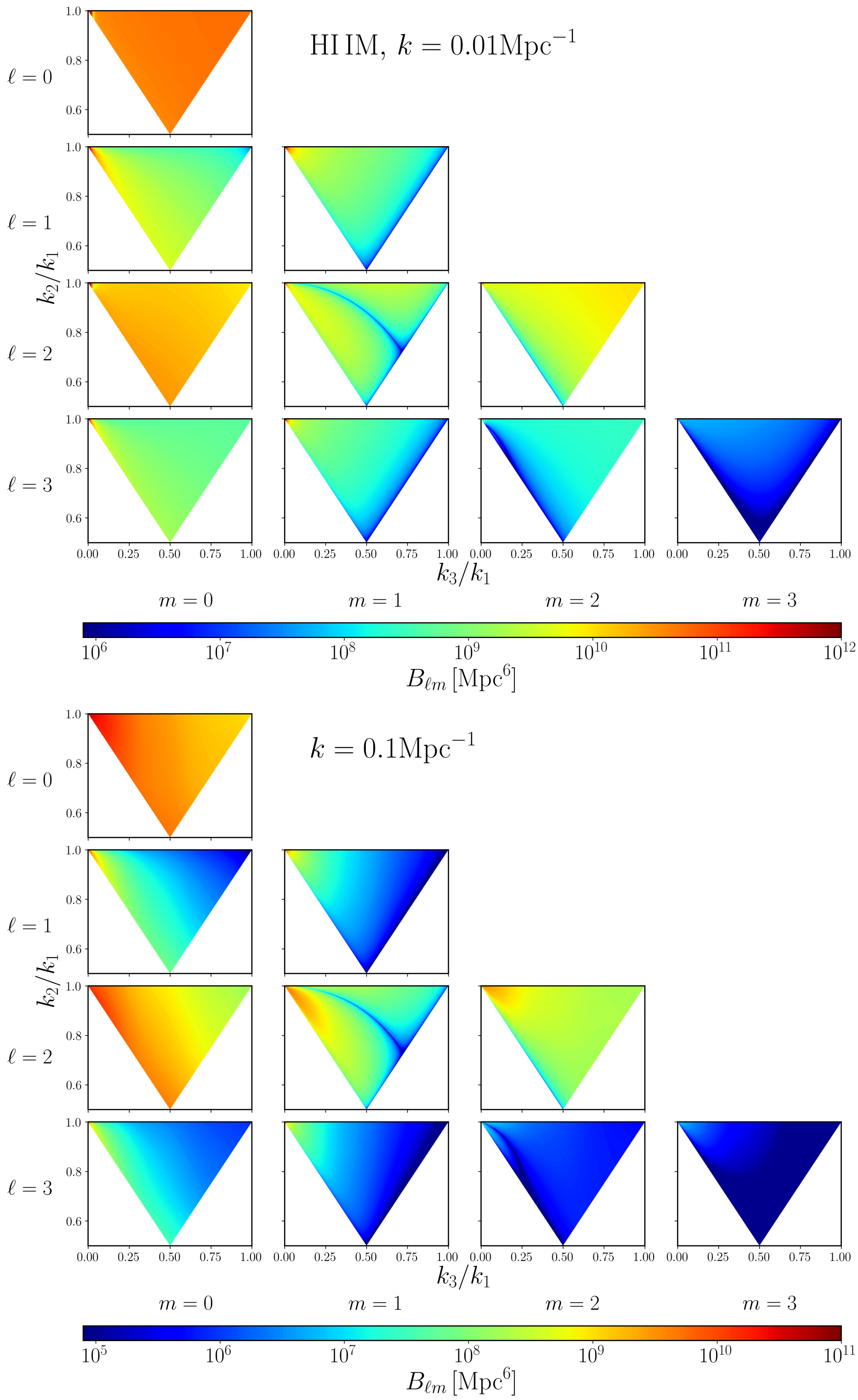

Figure 7.7.: Selected multipoles of the galaxy bispectrum, similar to figure 7.6, but with the bias model appropriate for intensity mapping. The value of fixed k_1 is indicated on the figures. The upper left corner of a wedge shape is the squeezed limit, the upper right corner is the equilateral configuration, and the lower corner is the co-linear configuration.

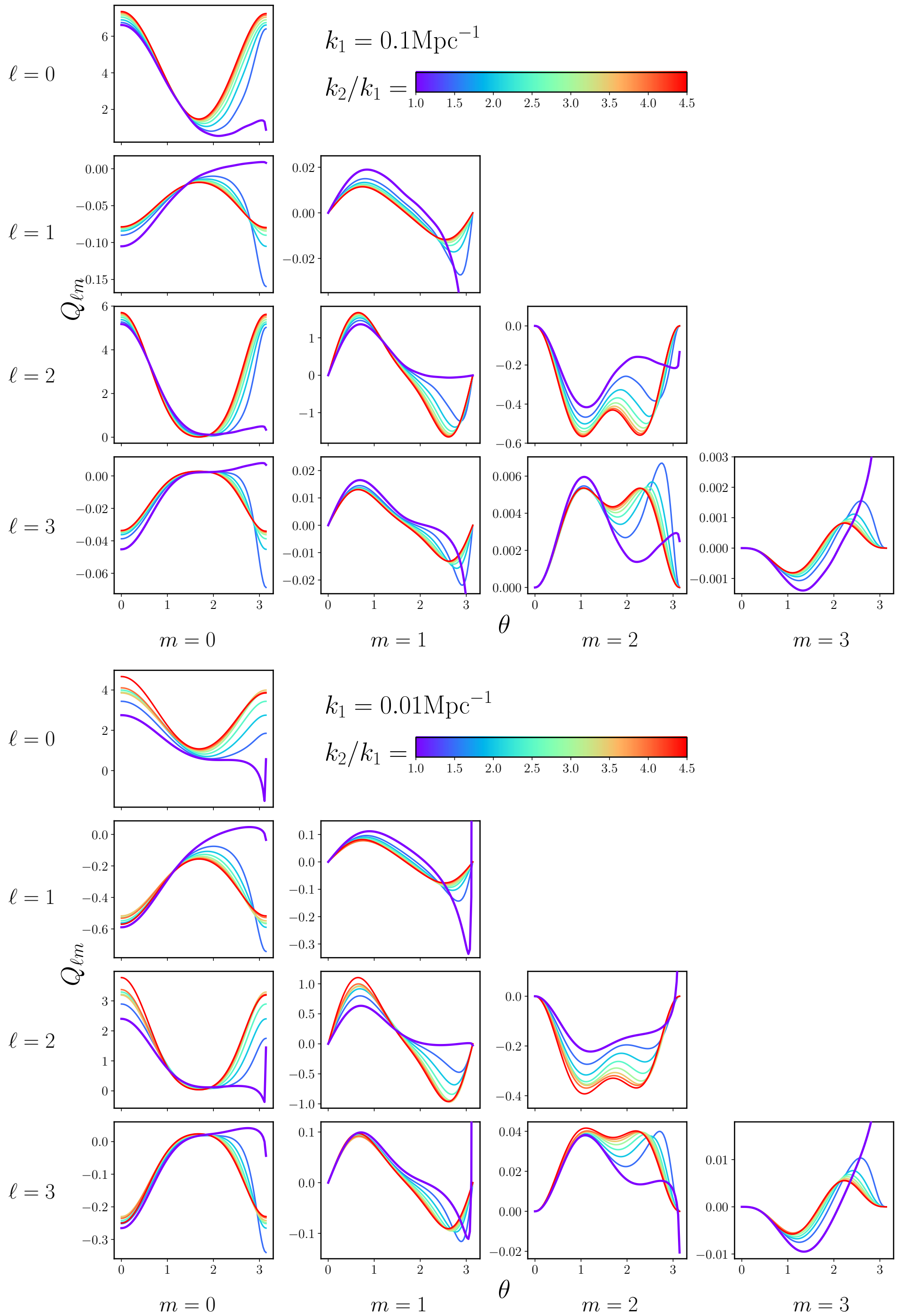

Figure 7.8.: Results for the reduced bispectrum $Q_{\ell m}$, where $\ell = 0 \ldots 3$ and negative m not shown. The multipoles ℓ, m are indicated on the figure, as well as the value of k_1 which is kept fixed. The colourbar and different colours denote the ratio of k_2/k_1, where the slightly thicker purple line is the isosceles triangle, which diverges as $\theta \to \pi$ since there $k_3 \to 0$.

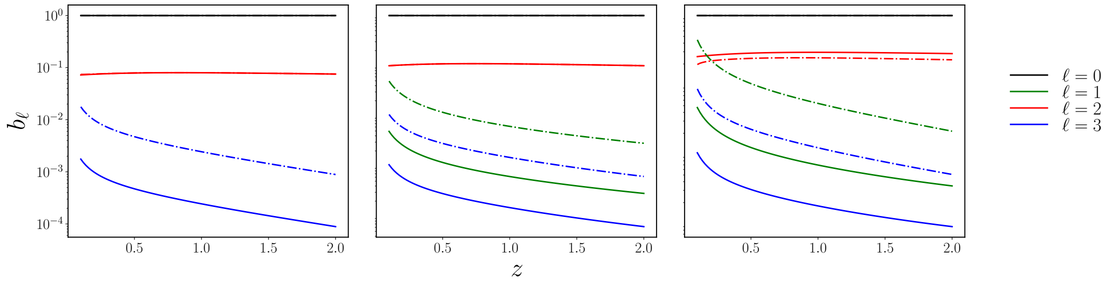

Figure 7.9.: Total power contained in the relativistic bispectrum normalised by the Newtonian monopole as a function of redshift z ranging from 0.1 to 2. The three panels are the equilateral configuration (left, with $\ell = 1$ vanishing), squeezed (middle) and co-linear flattened configuration (right). Solid lines for $k = 0.1\,\mathrm{Mpc}^{-1}$, and dash-dotted for $k = 0.01\,\mathrm{Mpc}^{-1}$.

Figures 7.3,7.4 and 7.5 show the amplitude of the total power as defined in (7.102). For each ℓ this contains all orientations per multipole divided by the amplitude of the Newtonian monopole. Values of ℓ are labelled on the figure, with the dotted lines denoting the Newtonian contribution (for even ℓ only). For small scales (larger wavenumber k), the Newtonian contributions are generally larger than the relativistic b_ℓ (i.e. odd ℓ), however at larger scales, above equality, the relative power contained in relativistic contributions increases. This shows up in the even multipoles as a divergence between the dotted (purely Newtonian) lines and solid (GR-corrected) lines. In the odd multipoles, we see an increase in amplitude, which at the largest scales become larger than the purely Newtonian signal. This is dependent on bias model and triangular configuration.

The colour-intensity maps in figures 7.6 and 7.7 show the amplitude of the relativistic bispectrum over the k_3/k_1, k_2/k_1 plane. The amplitude of the bispectrum signal peaks in the squeezed limit where $k_1 = k_2$, $k_3 \to 0$ which is in the top left corner in these plots. For the odd multipoles $\ell = 1$ and $\ell = 3$, the amplitude of the dipole is higher than the $\ell = 3$ case in most configurations. The amplitude of the relativistic bispectrum is also higher for larger scales (smaller k). For $\ell = 1$, the equilateral configuration, which lies in the upper right corner of the plots, is vanishing as we established analytically. We can also observe from these plots that there is a rough trend that more power is contained in the lower m multipoles.

The reduced bispectrum is plotted in figure 7.8, showing large relativistic contributions to the bispectrum odd-multipoles especially at large scales. This also shows the significant dependence on the triangle shape, depending on the orientation of the harmonic.

Finally figure 7.9 shows the total power divided by the Newtonian monopole, as a function of redshift. The model for bias used here is not physically realistic, but this illustrates the generic behaviour with redshift we can expect. It is interesting to observe how, when going towards lower redshift, the power in the relativistic corrections to the bispectrum grows compared to the Newtonian signal. This is especially noticeable in squeezed and flattened shapes where the dipole approaches or surpasses the $\ell = 2$ line. Of course, at low redshift the plane-parallel assumption that we have used becomes a worse approximation.

7.6. Conclusion

We have considered in detail for the first time the multipole decomposition of the observed relativistic galaxy bispectrum. In section 7.4 we have shown how the multipoles may be derived analytically, with an analytic formula given in equation (7.37), and have illustrated how they behave in the squeezed, equilateral and co-linear limits (which includes the flattened case) in section 7.5. We have shown how the amplitude of the relativistic signals behaves for two types of upcoming surveys – a Euclid-like galaxy survey, and an SKA intensity mapping survey. Our key findings are:

odd multipoles Relativistic effects generate a hierarchy of odd multipoles which are absent in the Newtonian picture, plus an additional contribution to all multipoles up to $\ell = 7$. In particular we find that the octopole is similar in amplitude to the dipole; it is only about a factor of 5 or so smaller than the dipole. These are both larger than the Newtonian hexadecapole on large scales. Higher multipoles are suppressed. This effect can be seen clearly in figures 7.3, 7.4, 7.5.

powers of k The leading power of the relativistic correction in each ℓ harmonic is $(\mathcal{H}/k)^1$ for odd multipoles and $(\mathcal{H}/k)^2$, for even multipoles. Furthermore, all odd multipoles contain the leading $(\mathcal{H}/k)$ correction, while lower values of ℓ contain the higher powers of $\mathcal{H}/k$, going up to $(\mathcal{H}/k)^7$ for $\ell = 1$ (though these are probably unobservable). An overview of occurring powers of k is given in figure 7.2.

special limits the co-linear case ($\theta = 0$ or π) only generates non-zero $m = 0$ multipoles and vanishes for all other values of m. The equilateral case is always zero for m odd, and is always zero for the special case of the dipole. For the squeezed limit we have leading $(\mathcal{H}/k)$ relativistic corrections for ℓ and $m \leq 3$ odd.

multipoles with shape We computed the amplitude of each ℓ, m over the range of triangle shapes in figures 7.6, 7.7. For each ℓ most of the power is contained in the lower m multipoles.

multipoles with scale We analysed the total power in each multipole as a function of scale for 3 triangle shapes at $z = 1$. Roughly speaking the even-ℓ are dominated by the Newtonian part and have little scale dependence relative to the Newtonian monopole, though this changes approaching the Hubble scale. For odd-ℓ the leading relativistic part dominates and the dipole reaches the size of the Newtonian quadrupole around equality scales.

redshift dependence Relative to the Newtonian monopole, all the relativistic multipoles decay with redshift, while the quadrupole is roughly constant. For large squeezed triangles the dipole is comparable in size to the quadrupole for small redshift as shown in figure 7.9.

Of course, the analysis here is limited by the fact we have neglected wide angle effects which will alter the multipoles. Integrated effects will also contribute, but their effect will be suppressed when we analyse the multipoles. We leave these contributions for future work. Also currently under investigation is detectability of the galaxy bispectrum, with the leading order contribution examined in Maartens et al. (2020).

8. Local primordial non-Gaussianity in the bispectrum

Next-generation galaxy and 21cm intensity mapping surveys will rely on a combination of the power spectrum and bispectrum for high-precision measurements of primordial non-Gaussianity. In turn, these measurements will allow us to distinguish between various models of inflation. However, precision observations require theoretical precision at least at the same level. We extend the theoretical understanding of the galaxy bispectrum by incorporating a consistent general relativistic model of galaxy bias at second order, in the presence of local primordial non-Gaussianity. The influence of primordial non-Gaussianity on the bispectrum extends beyond the galaxy bias and the dark matter density, due to redshift-space effects. The standard redshift-space distortions at first and second order produce a well-known primordial non-Gaussian imprint on the bispectrum. Relativistic corrections to redshift-space distortions generate new contributions to this primordial non-Gaussian signal, arising from: (1) a coupling of first-order scale-dependent bias with first-order relativistic observational effects, and (2) linearly evolved non-Gaussianity in the second-order velocity and metric potentials which appear in relativistic observational effects. Our analysis allows for a consistent separation of the relativistic 'contamination' from the primordial signal, in order to avoid biasing the measurements by using an incorrect theoretical model. We show that the bias from using a Newtonian analysis of the squeezed bispectrum could be $\Delta f_{\rm NL} \sim 5$ for a Stage IV Hα survey.

8.1. Introduction

Galaxy number counts are distorted by projection effects that arise from observing on the past lightcone. The dominant perturbative effect on sub-Hubble scales is from redshift-space distortions (RSD) Sargent & Turner (1977); Kaiser (1987), which constitute the standard Newtonian approximation to projection effects. Lensing magnification produces the best-known relativistic correction to RSD Villumsen (1995), but there are further relativistic effects Yoo et al. (2009); Yoo (2010); Challinor & Lewis (2011); Bonvin & Durrer (2011). The basic idea is the following. The number of sources, $\mathrm{d}\mathbb{N}$, above the luminosity threshold that are counted by the observer in a solid angle element about unit direction $\boldsymbol{n}$ and in a redshift interval about a central redshift z, is given by

$$\mathrm{d}\mathbb{N} = N_g\, \mathrm{d}z\, \mathrm{d}\Omega_{\boldsymbol{n}} = n_g\, \mathrm{d}\mathcal{V}\,. \tag{8.1}$$

The second equality relates the observed quantities to those measured in the rest frame of the source. N_g is the number that is counted by the observer per redshift per solid angle, while n_g is the number per proper volume, which is not observed by the observer but is the quantity that would be measured at the source. Similarly, $\mathrm{d}\mathcal{V}$ is not the observed volume element but the corresponding proper volume element at the source.

Then the observed number density contrast, $\Delta_g = (N_g - \bar{N}_g)/\bar{N}_g$, is related to the proper number density contrast at the source, $\delta_g = (n_g - \bar{n}_g)/\bar{n}_g$, by volume, redshift and luminosity perturbations. At first order in Poisson gauge, the gauge-independent relation (8.1) leads to

$$\begin{aligned}\Delta_g &= \delta_g + \text{RSD} + \text{lensing effect} + \text{other relativistic effects}\\ &= \delta_g - \frac{1}{\mathcal{H}}\boldsymbol{n}\cdot\boldsymbol{\nabla}\big(\boldsymbol{v}\cdot\boldsymbol{n}\big) + 2(1-\mathcal{Q})\kappa + A\big(\boldsymbol{v}\cdot\boldsymbol{n}\big) + B\Psi + \int \mathrm{d}\chi\, C\Psi' + \int \mathrm{d}\chi\, E\Psi\,.\end{aligned} \tag{8.2}$$

Here $\mathcal{H} = \mathrm{d}\ln a/\mathrm{d}\eta = (\ln a)'$ is the conformal Hubble rate, $\boldsymbol{v} = \boldsymbol{\nabla}V$ is the peculiar velocity (V is not to be confused with the often-used alternative $v = |\boldsymbol{v}|$), κ is the integrated lensing convergence, $\mathcal{Q}$ is the magnification bias, χ is the comoving line-of-sight distance and the integrals are from source to observer. The perturbed metric is given by

$$a^{-2}\mathrm{d}s^2 = -\big(1+2\Phi\big)\mathrm{d}\eta^2 + \big(1-2\Psi\big)\mathrm{d}\boldsymbol{x}^2\,, \tag{8.3}$$

and we have assumed $\Phi = \Psi$. The time-dependent factors A, B, C, E in (8.2) correspond respectively to Doppler, Sachs-Wolfe, integrated Sachs-Wolfe and time-delay effects. In Fourier space the Doppler term scales as $\partial V \propto (\mathcal{H}/k)\delta_m$, while the remaining terms scale as $\Psi \propto (\mathcal{H}/k)^2\delta_m$. Thus the other relativistic effects are suppressed on sub-Hubble scales, unlike the lensing effect, which scales as $\partial^2\Psi \propto \delta_m$.

The case of 21cm intensity mapping follows from the number count expressions by using the 'dictionary' given in Hall et al. (2013); Alonso et al. (2015); Fonseca et al. (2015) at first order and in Umeh et al. (2016); Di Dio et al. (2016); Jolicoeur et al. (2020) at second order.

The physical definition of linear Gaussian galaxy bias is in the joint matter-galaxy rest frame, which corresponds to the comoving gauge ('C gauge'),[1] so that (omitting luminosity dependence for brevity),

$$\delta_{g\mathrm{C}}(a, \boldsymbol{x}) = b_1(a)\delta_{m\mathrm{C}}(a, \boldsymbol{x})\,. \tag{8.4}$$

This relation is gauge-independent because C gauge corresponds to the physical rest frame. When transforming to other gauges, δ_g is in general no longer proportional to δ_m Challinor & Lewis (2011); Bruni et al. (2012); Jeong et al. (2012). For example, in the Poisson gauge of (8.2) and (8.3),

$$\delta_g = b_1\delta_{m\mathrm{C}} + (3 - b_e)\mathcal{H}V\,, \quad b_e = \frac{\partial \ln(a^3\bar{n}_g)}{\partial \ln a}\,, \tag{8.5}$$

where b_e is known as the evolution bias, which encodes the non-conservation of the background comoving galaxy number density. The velocity potential V scales as Ψ by the Euler equation, $V \propto \Psi \propto (\mathcal{H}/k)^2\delta_m$, and therefore the gauge correction $(3 - b_e)\mathcal{H}V$ is only non-negligible on Hubble scales and may be neglected in a Newtonian approximation.

Local primordial non-Gaussianity (PNG) generates scale-dependent linear bias, with constant parameter $f_{\rm NL}$ Dalal et al. (2008); Matarrese & Verde (2008):

$$b_1(a) \;\to\; b_1(a) + 3\,\delta_{\rm crit}\Omega_{m0}H_0^2\,\frac{\big[b_1(a) - 1\big]}{D(a)}\,g_{\rm in}\,\frac{f_{\rm NL}}{T(k)k^2}\,. \tag{8.6}$$

The threshold density contrast for collapse is usually taken to be $\delta_{\rm crit} = 1.686$, and the growth factor D is normalised to 1 today ($a_0 = 1$), i.e. $\delta_m(a, \boldsymbol{k}) = D(a)\delta_{m0}(\boldsymbol{k})$. The growth suppression factor for the potential Ψ is $g = D/a$, which is thus also normalised as $g_0 = 1$, with initial value $g_{\rm in}$ deep in the matter era, and T is the transfer function. Note that (8.6) follows the CMB convention for $f_{\rm NL}$ Baldauf et al. (2011); Desjacques et al. (2018); $g_{\rm in}$ can be removed from (8.6) if D is normalised as

[1] In the ΛCDM model the comoving and synchronous gauges coincide.

$D_{\rm in} = a_{\rm in}$. In a ΛCDM model we have the useful relation Villa & Rampf (2016)

$$\frac{g_{\rm in}}{g} = \frac{3}{5}\Big(1 + \frac{2f}{3\Omega_m}\Big), \tag{8.7}$$

where the growth rate of linear matter perturbations, $f = {\rm d}\ln D/{\rm d}\ln a$, is very well approximated by $f(a) = \Omega_m(a)^{0.545}$.

The PNG component of galaxy bias in (8.6) scales as H_0^2/k^2 on ultra-large scales, i.e. above the equality scale, $k < k_{\rm eq}$, where $T \approx 1$. It is strongly suppressed on scales $k \gg k_{\rm eq}$ by $T(k)$. PNG has a similar impact on the power spectrum to the impact of ultra-large-scale relativistic effects. This means that relativistic effects contaminate the primordial signal – leading to biases if a Newtonian approximation is used to model the galaxy power spectrum (see Bruni et al. (2012); Jeong et al. (2012); Camera et al. (2015b)). The relativistic galaxy power spectrum has been used to analyse and predict the capability of future galaxy and intensity mapping surveys to measure the local PNG parameter $f_{\rm NL}$, while avoiding the bias that is inherent in a Newtonian analysis (see e.g. Bruni et al. (2012); Jeong et al. (2012); Lopez-Honorez et al. (2012); Yoo et al. (2012); Raccanelli et al. (2014); Camera et al. (2015a,b); Raccanelli et al. (2016); Alonso et al. (2015); Alonso & Ferreira (2015); Fonseca et al. (2015, 2017); Abramo & Bertacca (2017); Lorenz et al. (2018); Fonseca et al. (2018); Ballardini et al. (2019); Grimm et al. (2020); Bernal et al. (2020); Wang et al. (2020)).

The tree-level bispectrum requires the number counts in redshift space up to second order. In the Newtonian approximation, the projection effects are the second-order RSD terms (see e.g. Tellarini et al. (2016)). The relativistic corrections to RSD at second-order are extremely complicated, since they involve quadratic couplings of all the first-order terms, as well as introducing new terms that do not enter at first order, such as the transverse peculiar velocity, the lensing deflection angle and the lensing shear Bertacca et al. (2014a,b); Yoo & Zaldarriaga (2014); Di Dio et al. (2014); Bertacca (2015). There are further relativistic corrections that are not projection effects. Firstly, the Newtonian model of second-order galaxy bias in the comoving frame requires a relativistic correction, unlike the first-order bias (see Section 8.2). Secondly, and similar to the first-order case, the second-order galaxy bias relation needs relativistic gauge corrections when using non-comoving gauges such as the Poisson gauge. These are second-order extensions of equations like (8.5). In summary, the second-order relativistic corrections to the galaxy bispectrum in the Gaussian case are:

- relativistic projection corrections to the Newtonian RSD Bertacca et al. (2014a,b); Yoo & Zaldarriaga (2014); Di Dio et al. (2014); Bertacca (2015);
- relativistic corrections to the Newtonian bias model in the comoving frame at second order, which were only recently derived Umeh et al. (2019); Umeh & Koyama (2019);
- relativistic gauge corrections to the second-order number density when using non-comoving gauges Bertacca et al. (2014a,b).

As in the case of the power spectrum, local PNG affects the bispectrum on very large scales, which is also where the relativistic effects are strongest. This leads again to a contamination of the primordial signal by relativistic effects, necessitating a relativistic analysis. A Gaussian primordial universe could be mistakenly interpreted as non-Gaussian if a Newtonian model is used for the bispectrum in analysis of the data, as shown by Kehagias et al. (2015); Umeh et al. (2017); Jolicoeur et al. (2017); Koyama et al. (2018).

There are important differences between the power spectrum and bispectrum:

- At first order, there is no relativistic correction to the bias model in comoving gauge – the relativistic correction arises at second order Umeh et al. (2019); Umeh & Koyama (2019). Therefore the tree-level bispectrum contains a relativistic correction to the bias model, but the tree-level power spectrum does not.
- There is no PNG signal in the primordial *matter* power spectrum at tree level, so that the local PNG signal in the tree-level galaxy power spectrum is sourced only by scale-dependent bias.
- By contrast, local PNG in the galaxy bispectrum is sourced by scale-dependent bias, by the primordial matter bispectrum and by RSD at second order (see Tellarini et al. (2016) and Section 8.2.4 below).
- Second-order relativistic corrections to RSD induce new local PNG effects in the bispectrum, via (1) a coupling of first-order scale-dependent bias to first-order relativistic projection effects, and (2) the linearly evolved PNG in second-order velocity and metric potentials, which appear in relativistic projection effects (absent in the standard Newtonian analysis).

Since local PNG affects the power spectrum and bispectrum differently, a Newtonian analysis could mistakenly identify inconsistencies between the power spectrum and bispectrum $f_{\rm NL}$ measurements, which could wrongly lead to an inference of hidden systematics or deviations from general relativity.

PNG in the galaxy bispectrum has been extensively investigated in the Newtonian approximation. Most work has used the Fourier bispectrum, implicitly incorporating a plane-parallel assumption (see e.g. Verde et al. (2000); Scoccimarro et al. (2004); Sefusatti et al. (2006); Sefusatti & Komatsu (2007); Giannantonio & Porciani (2010); Baldauf et al. (2011); Tellarini et al. (2015, 2016); Desjacques et al. (2018); Watkinson et al. (2017); Majumdar et al. (2018); Karagiannis et al. (2018); Yankelevich & Porciani (2019); Sarkar et al. (2019); Karagiannis et al. (2020b); Bharadwaj et al. (2020); Karagiannis et al. (2020a); Moradinezhad Dizgah et al. (2020)) and we follow this approximation. Our previous work Umeh et al. (2017) included the local (non-integrated) relativistic effects in the Fourier bispectrum for the first time. This was extended by our work Jolicoeur et al. (2017, 2018, 2019); Clarkson et al. (2019); Maartens et al. (2020); de Weerd et al. (2020); Jolicoeur et al. (2020); Umeh et al. (2020), all in the case of primordial Gaussianity. Here we incorporate local PNG into the relativistic bispectrum. This involves applying the recent results of Umeh et al. (2019); Umeh & Koyama (2019) on relativistic corrections to the second-order galaxy bias model. In addition, we derive the new local PNG terms induced by a coupling of first-order scale-dependent bias and first-order relativistic projection effects and by linearly evolved second-order relativistic projection effects.

The paper is structured as follows. Section 8.2.4 reviews the relativistic correction to the galaxy bias, including the case of local PNG. In addition, we show how the linearly evolved second-order metric and velocity potentials carry a primordial non-Gaussian signal, which is imprinted in the bispectrum by relativistic projection effects. In Section 8.3, after presenting the relativistic correction to the matter bispectrum, we discuss the number density contrast in redshift space, which brings into play the relativistic projection effects. We combine the various results to derive the relativistic galaxy bispectrum, including all local PNG effects, and we show examples of the galaxy bispectrum for a Stage IV Hα spectroscopic survey. We summarise and conclude in Section 8.4.

Conventions used: We assume a flat ΛCDM model, based on general relativity and perturbed up to second order, in which the matter is pressure-free and irrotational on perturbative scales. Generalisations to allow dynamical dark energy and relativistic modified gravity are straightforward, but are not included. For numerical calculations, we use the Planck 2018 best-fit parameters Aghanim et al. (2018). Perturbed quantities are expanded as $X+X^{(2)}/2$, and may be split as $X_{\rm N}+X_{\rm GR}+X_{\rm nG}$, and similarly at second order, where N denotes the Newtonian approximation, GR denotes the relativistic correction and nG denotes the local PNG contribution. GR corrections are highlighted in magenta. Our definition of the metric potentials in (8.3) leads to the first-order Poisson equation

$$\nabla^2\Psi = +\frac{3}{2}\Omega_m\mathcal{H}^2\,\delta_{\rm C}\,, \tag{8.8}$$

where $\Phi = \Psi$ in ΛCDM. Here and in the remainder of the paper, we omit the subscript m on the matter density contrast for brevity. At second order, the perturbed metric in Poisson gauge is given by

$$a^{-2}{\rm d}s^2 = -\big[1+2\Psi+\Phi^{(2)}\big]{\rm d}\eta^2 + \big[1-2\Psi-\Psi^{(2)}\big]{\rm d}\boldsymbol{x}^2\,. \tag{8.9}$$

Here we have neglected the relativistic vector and tensor modes that are generated by scalar mode coupling, so that we only consider the relativistic scalar contribution to the bispectrum. This approximation is justified by the fact that the relativistic vector contribution to the bispectrum is typically 2 orders of magnitude below the relativistic scalar contribution on observable scales, while the relativistic tensor contribution is typically an order of magnitude below that of the vector contribution (see Jolicoeur et al. (2019)).

8.2. Local primordial non-Gaussianity in the galaxy bias

Local PNG is defined as a simple form of nonlinearity in the primordial curvature perturbation, which is local in configuration space. In terms of the gravitational potential deep in the matter era, we have

$$-\Big[\Psi_{\rm in}(\boldsymbol{x}) + \frac{1}{2}\Psi^{(2)}_{\rm in}(\boldsymbol{x})\Big] = \varphi_{\rm in}(\boldsymbol{x}) + f_{\rm NL}\big[\varphi_{\rm in}(\boldsymbol{x})^2 - \big\langle\varphi^2_{\rm in}\big\rangle\big], \tag{8.10}$$

where $\varphi_{\rm in}$ is the first-order Gaussian part. The standard definition of $f_{\rm NL}$ uses a convention for Ψ that is different to ours, with a minus on the right of the Poisson equation (8.8). In order to keep the standard sign of $f_{\rm NL}$, we made a sign change on the left of (8.10). ($f_{\rm NL}$ in Villa & Rampf (2016); Koyama et al. (2018); Umeh & Koyama (2019) is of opposite sign to the standard sign that we use.)

8.2.1. First-order bias

In (8.10), the Gaussian part of the potential deep in the matter era (but after decoupling) is related to the linear primordial potential by the transfer function:

$$\varphi_{\rm in}(\boldsymbol{k}) = T(k)\,\varphi_{\rm p}(\boldsymbol{k}) \quad \text{for} \quad a_{\rm p} \ll a_{\rm eq} \ll a_{\rm in}\,. \tag{8.11}$$

Here $\varphi_{\rm p}(\boldsymbol{k}) = -9\Psi(a_{\rm p}, \boldsymbol{k})/10$, where the factor $9/10$ ensures conservation of the curvature perturbation on super-Hubble scales. After equality, the potential evolves with the growth suppression factor, so that

$$\varphi(a, \boldsymbol{k}) = \frac{g(a)}{g_{\rm in}}\varphi_{\rm in}(\boldsymbol{k}) \quad \text{for} \quad a \geq a_{\rm in} > a_{\rm dec}\,. \tag{8.12}$$

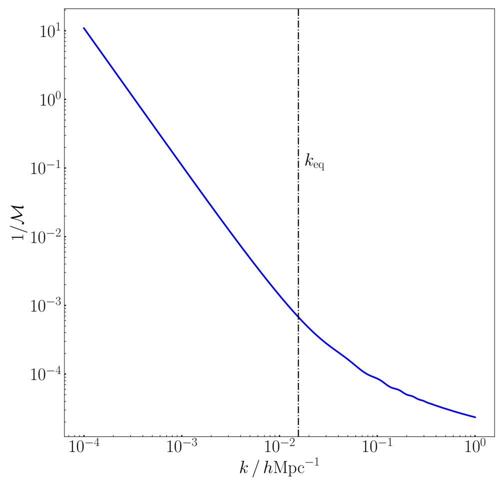

Figure 8.1.: $\mathcal{M}^{-1} = \varphi_{\rm p}/\delta_{\rm C}^{(1)}$ at $z = 1$.

We relate the late-time matter density contrast to the primordial potential via the Poisson equation (8.8), using (8.7), (8.11) and (8.12):

$$\delta_{\rm C}(a, \boldsymbol{k}) = \mathcal{M}(a, k)\varphi_{\rm p}(\boldsymbol{k}) \quad \text{where} \quad \mathcal{M}(a, k) = \frac{10}{3\mathcal{H}(a)^2\big[3\Omega_m(a) + 2f(a)\big]}\,k^2\,T(k)\,. \tag{8.13}$$

This relation is illustrated in Fig. 8.1. The matter and number density contrasts can be written as

$$\delta_{\rm C} = \delta_{\rm C,N} \quad \text{and} \quad \delta_{g\rm C} = \delta_{g\rm C,N} + \delta_{g\rm C,nG}\,. \tag{8.14}$$

This follows since there is no GR correction to either contrast and no PNG in the Gaussian matter density contrast:

$$\delta_{\mathrm{C,GR}} = 0 = \delta_{g\mathrm{C,GR}}\,, \quad \delta_{\mathrm{C,nG}} = 0\,. \tag{8.15}$$

Then it follows that

$$\delta_{g\mathrm{C}} = \delta_{g\mathrm{C,N}} + \delta_{g\mathrm{C,nG}} = b_{10}\,\delta_{\mathrm{C}} + b_{01}\,\varphi_{\mathrm{p}}\,, \tag{8.16}$$

where the Gaussian and non-Gaussian bias coefficients are

$$b_{10} = b_1\,, \quad b_{01} = 2f_{\mathrm{NL}}\delta_{\mathrm{crit}}(b_{10} - 1)\,. \tag{8.17}$$

The relations (8.13)–(8.17) then recover (8.6).

At first order, there is *no* GR correction to the bias relation expressed in the matter-galaxy rest frame. This is no longer true at second order.

The first-order metric potential is Gaussian by (8.10) and has no GR correction by (8.15) and the Poisson equation. From the Euler equation ($V' + \mathcal{H}V = -\Psi$) it follows that the velocity also has no GR and no PNG corrections:

$$\Psi = \Psi_{\mathrm{N}}\,, \qquad V = V_{\mathrm{N}}\,. \tag{8.18}$$

8.2.2. Second-order bias: Newtonian approximation

At second order, the galaxy bias is physically defined in comoving gauge, but any gauge may be used in general relativity. Standard Newtonian perturbation theory is often given in an Eulerian frame, and so it is useful for comparison to express the bias in a suitable Eulerian frame. We use Poisson gauge here, following Umeh et al. (2017); Tram et al. (2016); Jolicoeur et al. (2017, 2018, 2019); Clarkson et al. (2019); Maartens et al. (2020); de Weerd et al. (2020), but with the galaxy and matter density contrasts in total-matter gauge ('T gauge'). The total-matter gauge is a convenient Eulerian choice for the density contrasts, since it has the same spatial coordinates as the Poisson gauge at first order and the same time-slicing as the comoving gauge at first and second orders Bartolo et al. (2016); Villa & Rampf (2016); Tram et al. (2016). As a result, at first order the total-matter density contrasts coincide with those of the comoving gauge: $\delta_{\mathrm{T}} = \delta_{\mathrm{C}}$, $\delta_{g\mathrm{T}} = \delta_{g\mathrm{C}}$, and we can rewrite (8.16) as

$$\delta_{g\mathrm{T}} = \delta_{g\mathrm{T,N}} + \delta_{g\mathrm{T,nG}} \tag{8.19}$$

$$= b_{10}\,\delta_{\mathrm{T}} + b_{01}\,\varphi_{\mathrm{p}} = \Big(b_{10} + \frac{b_{01}}{\mathcal{M}}\Big)\delta_{\mathrm{T}}\,. \tag{8.20}$$

At second order, the total-matter and Poisson matter density contrasts agree in the Newtonian approximation: $\delta^{(2)}_{\mathrm{T,N}} = \delta^{(2)}_{\mathrm{N}}$, while the comoving and total-matter Newtonian density contrasts are related via a purely spatial gauge transformation Bertacca et al. (2015); Villa & Rampf (2016); Jolicoeur et al. (2017); Umeh et al. (2019):

$$\delta^{(2)}_{\mathrm{T,N}} = \delta^{(2)}_{\mathrm{C,N}} + 2\xi^i\partial_i\delta_{\mathrm{C}}\,, \quad \delta^{(2)}_{g\mathrm{T,N}} = \delta^{(2)}_{g\mathrm{C,N}} + 2\xi^i\partial_i\delta_{g\mathrm{C}}\,, \tag{8.21}$$

where

$$\xi^i = \partial^i\nabla^{-2}\delta_{\mathrm{C}} = \partial^i\nabla^{-2}\delta_{\mathrm{T}}\,. \tag{8.22}$$

(The GR parts of the second-order density contrasts in comoving and total-matter gauges are equal; see below.)

For the small scales involved in local clustering of matter density, the Poisson equation at second order has the same Newtonian form as at first order. Then we can extend (8.13) up to second order to define the linearly evolved local PNG part of the density contrast, whose nonlinearity is purely primordial:

$$\delta^{(2)}_{\mathrm{T,nG}} = \mathcal{M}\,\varphi^{(2)}_{\mathrm{p}} = 2f_{\mathrm{NL}}\,\mathcal{M}\,\varphi_{\mathrm{p}} * \varphi_{\mathrm{p}}\,, \tag{8.23}$$

where the $*$ denotes a convolution in Fourier space. This leads to

$$\delta^{(2)}_{\mathrm{T,nG}} = 2f_{\mathrm{NL}}\,\mathcal{M}(a,k)\int\frac{\mathrm{d}\boldsymbol{k}'}{(2\pi)^3}\,\frac{\delta_{\mathrm{T}}(a,\boldsymbol{k}')}{\mathcal{M}(a,k')}\,\frac{\delta_{\mathrm{T}}(a,\boldsymbol{k}-\boldsymbol{k}')}{\mathcal{M}(a,|\boldsymbol{k}-\boldsymbol{k}'|)}\,. \tag{8.24}$$

In order to include the nonlinearity due to gravitational evolution, we add the standard Newtonian contribution for Gaussian initial conditions to the local PNG part:

$$\delta^{(2)}_{\mathrm{T,N}}(a,\boldsymbol{k}) + \delta^{(2)}_{\mathrm{T,nG}}(a,\boldsymbol{k}) \tag{8.25}$$

$$= \int\frac{\mathrm{d}\boldsymbol{k}'}{(2\pi)^3}\left[F_2(a,\boldsymbol{k}',\boldsymbol{k}-\boldsymbol{k}') + 2f_{\mathrm{NL}}\,\frac{\mathcal{M}(a,k)}{\mathcal{M}(a,k')\,\mathcal{M}(a,|\boldsymbol{k}-\boldsymbol{k}'|)}\right]\delta_{\mathrm{T}}(a,\boldsymbol{k}')\,\delta_{\mathrm{T}}(a,\boldsymbol{k}-\boldsymbol{k}')\,.$$

The standard Newtonian mode-coupling kernel for ΛCDM is Villa & Rampf (2016):

$$F_2(a, \boldsymbol{k}_1, \boldsymbol{k}_2) = 1 + \frac{F(a)}{D(a)^2} + \left(\frac{k_1}{k_2} + \frac{k_2}{k_1}\right)\hat{\boldsymbol{k}}_1 \cdot \hat{\boldsymbol{k}}_2 + \left[1 - \frac{F(a)}{D(a)^2}\right]\left(\hat{\boldsymbol{k}}_1 \cdot \hat{\boldsymbol{k}}_2\right)^2 , \quad (8.26)$$

where F is the second-order growth factor. The Einstein–de Sitter relation $F/D^2 = 3/7$ is a very good approximation in ΛCDM. We use this approximation, in which F_2 is effectively time independent.

At second order, the standard Newtonian bias model, including tidal bias in the Gaussian part and all local PNG contributions, is given by (see Desjacques et al. (2018) for a comprehensive treatment):

$$\begin{aligned}\delta^{(2)}_{g\mathrm{T,N}} + \delta^{(2)}_{g\mathrm{T,nG}} = {} & b_{10}\,\delta^{(2)}_{\mathrm{T,N}} + b_{20}\big(\delta_{\mathrm{T}}\big)^2 + b_s\, s^2 \\ & + b_{10}\,\delta^{(2)}_{\mathrm{T,nG}} + b_{11}\,\delta_{\mathrm{T}}\,\varphi_{\mathrm{p}} + b_n\,\xi^i\,\partial_i\,\varphi_{\mathrm{p}} + b_{02}\big(\varphi_{\mathrm{p}}\big)^2 . \end{aligned} \quad (8.27)$$

The (Eulerian) bias parameters in the case of Gaussian initial conditions are in the first line on the right-hand side: the linear and quadratic biases, b_{10} and b_{20}, and the tidal bias b_s, where

$$s^2 = s_{ij}s^{ij}\,, \quad s_{ij} = \Big(\partial_i\partial_j - \frac{1}{3}\delta_{ij}\nabla^2\Big)\nabla^{-2}\delta_{\mathrm{T}}\,. \quad (8.28)$$

The second line of (8.27) contains the local PNG contribution, with three new bias parameters b_{11}, b_n, b_{02}. The first term is the primordial dark matter contribution, from (8.25); note that $\tilde{\delta}^{(2)}_{\mathrm{T,N}}$ is proportional to f_{NL}. The b_{11}, b_n terms scale as $(\mathcal{H}^2/k^2)\,(\delta_{\mathrm{T}})^2$, while the b_{02} term is $\mathcal{O}(\mathcal{H}^4/k^4)$. The new bias parameters vanish when $f_{\mathrm{NL}} = 0$; in the presence of local PNG, they are given by Tellarini et al. (2015); Desjacques et al. (2018); Umeh & Koyama (2019):

$$b_{11} = 4f_{\mathrm{NL}}\Big[\delta_{\mathrm{crit}}\, b_{20} + \Big(\frac{13}{21}\delta_{\mathrm{crit}} - 1\Big)(b_{10} - 1) + 1\Big]\,, \quad (8.29)$$

$$b_n = 4f_{\mathrm{NL}}\Big[\delta_{\mathrm{crit}}(1 - b_{10}) + 1\Big]\,, \quad (8.30)$$

$$b_{02} = 4f^2_{\mathrm{NL}}\delta_{\mathrm{crit}}\Big[\delta_{\mathrm{crit}}\, b_{20} - 2\Big(\frac{4}{21}\delta_{\mathrm{crit}} + 1\Big)(b_{10} - 1)\Big]. \quad (8.31)$$

Note that the expressions for the bias coefficients in (8.29)–(8.31), as well as for b_{01} in (8.17), are based on a universal halo mass function. (For recent work on the limits of the universality assumption, see Barreira et al. (2020); Barreira (2020).)

8.2.3. Second-order bias: relativistic corrections

The relativistic second-order galaxy bias model has been derived in Umeh et al. (2019) (Gaussian case) and Umeh & Koyama (2019) (with local PNG). The key feature to bear in mind is the following:

> *GR corrections in the galaxy number density contrast $\delta^{(2)}_{g\mathrm{T}}$ do not change the galaxy bias terms in* (8.27)*, which contain all the local PNG effects.*

This separation between GR effects and local PNG in the number density can be understood as follows.

- The intrinsic nonlinearity of GR modulates the galaxy number density via large-scale modes. However, this does not affect small-scale clustering: GR effects do *not* modulate the variance of small-scale density modes Koyama et al. (2018); Dai et al. (2015); de Putter et al. (2015).
- By contrast, local PNG imprints a primordial long-short coupling that induces a long-mode modulation of the variance and thus changes the galaxy bias.

As a consequence, we expect that relativistic corrections to the bias relation should be independent of non-Gaussianity and apply only on ultra-large scales (for a different view, see Matarrese et al. (2021)). These two features are consistent with the behaviour of (8.27) under change of gauge:

> *The Newtonian bias relation* (8.27) *is gauge-independent only on small scales.*
> *Relativistic corrections to* (8.27) *are needed to enforce gauge-independence of the bias relation on ultra-large scales.*

As shown in Umeh et al. (2019); Umeh & Koyama (2019), gauge-independence requires the addition to (8.27) of the relativistic part of the second-order matter density contrast. The relativistic modes are super-Hubble at equality and arise from nonlinear GR corrections to the Newtonian Poisson equation Bruni et al. (2014); Bartolo et al. (2016); Villa & Rampf (2016); Tram et al. (2016):

$$\delta^{(2)}_{\mathrm{C,GR}} = \delta^{(2)}_{\mathrm{T,GR}} = \frac{20}{3}\,\delta_{\mathrm{T}}\,\varphi_{\mathrm{in}} - \frac{5}{3}\,\xi^i\,\partial_i\,\varphi_{\mathrm{in}} \equiv \delta^{(2)}_{g\mathrm{T,GR}}\,. \tag{8.32}$$

Here φ_{in} is the ultra-large scale potential deep in the matter era,

$$\varphi_{\mathrm{in}}(\boldsymbol{k}) = \varphi_{\mathrm{in}}\big(\boldsymbol{k}\,|\,k < k_{\mathrm{eq}}\big)\,. \tag{8.33}$$

When we relate $\varphi_{\rm in}$ to the density contrast today, via (8.11) and (8.13), we need to impose $T = 1$ on the transfer function, by (8.33).

The relativistic second-order galaxy bias model of Umeh & Koyama (2019) can be written in T-gauge as

$$\delta^{(2)}_{g\mathrm{T}} = \delta^{(2)}_{g\mathrm{T,N}} + \delta^{(2)}_{g\mathrm{T,nG}} + \delta^{(2)}_{g\mathrm{T,GR}}\,, \tag{8.34}$$

where

$$\delta^{(2)}_{g\mathrm{T,N}} = b_{10}\,\delta^{(2)}_{\mathrm{T,N}} + b_{20}\big(\delta_{\mathrm{T}}\big)^2 + b_s\, s^2\,, \tag{8.35}$$

$$\delta^{(2)}_{g\mathrm{T,nG}} = b_{10}\,\delta^{(2)}_{\mathrm{T,nG}} + b_{11}\,\delta_{\mathrm{T}}\,\varphi_{\mathrm{p}} + b_n\,\xi^i\,\partial_i\,\varphi_{\mathrm{p}} + b_{02}\big(\varphi_{\mathrm{p}}\big)^2, \tag{8.36}$$

$$\delta^{(2)}_{g\mathrm{T,GR}} = \frac{20}{3}\,\delta_{\mathrm{T}}\,\varphi_{\rm in} - \frac{5}{3}\,\xi^i\,\partial_i\,\varphi_{\rm in}\,. \tag{8.37}$$

Here (8.35) and (8.36) recover the Newtonian relation (8.27).

Both the local PNG and GR terms scale as $(\mathcal{H}^2/k^2)\,(\delta_{\mathrm{T}})^2$, so that the GR correction *cannot* be neglected. Although they are of the same order of magnitude, there is a key distinction between them: local PNG induces a short-long mode coupling, and thus affects the primordial potential φ_{p} on small scales, while the GR corrections affect only the ultra-large-scale primordial modes. In the absence of local PNG, i.e. for $f_{\mathrm{NL}} = 0$, the GR terms survive and constitute the relativistic bias correction in the case of Gaussian initial conditions, as derived in Umeh et al. (2019).

Finally, we transform (8.20) and (8.34) to Poisson gauge:

$$\delta_g = \delta_{g\mathrm{T}} + (3 - b_e)\mathcal{H}V\,, \tag{8.38}$$

$$\begin{aligned}\delta^{(2)}_g = \delta^{(2)}_{g\mathrm{T}} &+ (3 - b_e)\mathcal{H}V^{(2)} + \Big[(b_e - 3)\mathcal{H}' + (b_e - 3)(b_e - 4)\mathcal{H}^2 + b_e'\mathcal{H}\Big]\big(V\big)^2 \\ &+ 2(3 - b_e)\mathcal{H}V\,\delta_{g\mathrm{T}} - 2V\,\delta'_{g\mathrm{T}} + 2(3 - b_e)\mathcal{H}V\,\Psi\,,\end{aligned} \tag{8.39}$$

where the GR corrections in magenta scale as $(\mathcal{H}^2/k^2)\,\delta_{\mathrm{T}}$ at first order, and as $(\mathcal{H}^2/k^2)\,(\delta_{\mathrm{T}})^2$ or $(\mathcal{H}^4/k^4)\,(\delta_{\mathrm{T}})^2$ at second order. For (8.39) we followed Bertacca et al. (2014b); Jolicoeur et al. (2017); de Weerd et al. (2020), but we significantly simplified their expressions, using the first-order Euler equation $V' + \mathcal{H}V = -\Psi$ and the relation

$$V = -\frac{2f}{3\Omega_m\mathcal{H}}\,\Psi\,, \tag{8.40}$$

which follows from the continuity equation, $\delta'_{\mathrm{T}} = -\nabla^2 V$, and the Poisson equation. We also included the evolution bias terms that are omitted in Umeh & Koyama (2019).

8.2.4. Second-order metric and velocity potentials

At second order, the number density contrast has a GR correction in addition to a PNG correction, as shown in (8.34). Unlike the first-order case, the metric and velocity potentials at second order also have nonzero GR and PNG corrections:

$$\Psi^{(2)} = \Psi^{(2)}_{\rm N} + \Psi^{(2)}_{\rm GR} + \Psi^{(2)}_{\rm nG}\,, \tag{8.41}$$
$$\Phi^{(2)} = \Psi^{(2)}_{\rm N} + \Phi^{(2)}_{\rm GR} + \Psi^{(2)}_{\rm nG}\,, \tag{8.42}$$
$$V^{(2)} = V^{(2)}_{\rm N} + V^{(2)}_{\rm GR} + V^{(2)}_{\rm nG}\,, \tag{8.43}$$

where we note that

$$\Phi^{(2)}_{\rm N} = \Psi^{(2)}_{\rm N} \quad \text{and} \quad \Phi^{(2)}_{\rm nG} = \Psi^{(2)}_{\rm nG}\,. \tag{8.44}$$

The GR corrections are derived in (Villa & Rampf, 2016) (which only considers modes $k < k_{\rm eq}$). Here we derive the PNG contributions, which include modes $k > k_{\rm eq}$.

The PNG corrections to metric and velocity potentials are linearly evolved, i.e., their nonlinearity is purely primordial, the same as in the case of the density contrast. They follow from constraint and energy conservation equations applied to the linearly evolved PNG part of the matter density contrast, $\delta^{(2)}_{\rm T,nG}$. As we argued in deriving (8.24), $\delta^{(2)}_{\rm T,nG}$ obeys the linear Newtonian Poisson equation. The same applies to the linearly evolved $\Psi^{(2)}_{\rm nG}$. From the Newtonian Poisson equation we find that

$$\begin{aligned}\Psi^{(2)}_{\rm nG}(a,\boldsymbol{k}) &= -\frac{3\Omega_m(a)\mathcal{H}(a)^2}{2k^2}\,\delta^{(2)}_{\rm T,nG}(a,\boldsymbol{k})\\ &= -\frac{10}{3}f_{\rm NL}\left[1+\frac{2f(a)}{3\Omega_m(a)}\right]^{-1} T(k)\,\big(\varphi_{\rm p}*\varphi_{\rm p}\big)(\boldsymbol{k})\,,\end{aligned} \tag{8.45}$$

where we used (8.13) and (8.24).

By (8.45), $\Psi^{(2)}_{\rm nG}$ grows as $(1+2f/3\Omega_m)^{-1}$, and thus

$$\Psi^{(2)\prime}_{\rm nG} = -\frac{2f}{\big(3\Omega_m+2f\big)}\left(\frac{f'}{f}+\mathcal{H}+2\frac{\mathcal{H}'}{\mathcal{H}}\right)\Psi^{(2)}_{\rm nG}\,. \tag{8.46}$$

The first-order linear equation (8.40), based on energy conservation and the Poisson equation, extends to second order for the linearly evolved PNG parts of the velocity and the potential. This determines the PNG part of the velocity:

$$V_{\rm nG}^{(2)} = -\frac{2f}{3\Omega_m \mathcal{H}}\,\Psi_{\rm nG}^{(2)}\,. \tag{8.47}$$

The linearly evolved PNG part of the second-order RSD term then follows as

$$\partial_\parallel^2 V_{\rm nG}^{(2)}(a,\boldsymbol{k}) = -2f_{\rm NL}\,\mathcal{H}(a)f(a)\mu^2\,\mathcal{M}(a,k)\,\big(\varphi_{\rm p}*\varphi_{\rm p}\big)(\boldsymbol{k})\,, \tag{8.48}$$

where $\partial_\parallel = \boldsymbol{n}\cdot\boldsymbol{\nabla}$ and $\mu = \hat{\boldsymbol{k}}\cdot\boldsymbol{n}$. Finally, the first-order linear relation $\Phi = \Psi$ extends to second order for the linearly evolved PNG part of $\Phi^{(2)}$, giving the second equality of (8.44).

8.3. Local primordial non-Gaussianity in the relativistic bispectrum

8.3.1. Matter bispectrum

The primordial contribution of matter, independent of halo formation, is given by the Newtonian approximation (8.25), corrected by the GR contribution in (8.32):

$$\delta_{\rm T}^{(2)} = \delta_{\rm T,N}^{(2)} + \delta_{\rm T,nG}^{(2)} + \frac{20}{3}\,\delta_{\rm T}\,\hat{\varphi}_{\rm in} - \frac{5}{3}\,\xi^i\,\partial_i\,\hat{\varphi}_{\rm in}\,. \tag{8.49}$$

The kernels in Fourier space corresponding to the GR terms in (8.49) are:

$$\delta_{\rm T}\,\hat{\varphi}_{\rm in} \;\to\; -\frac{\left(k_1^2+k_2^2\right)}{2k_1^2k_2^2}\,, \qquad \xi^i\,\partial_i\hat{\varphi}_{\rm in} \;\to\; -\frac{\boldsymbol{k}_1\cdot\boldsymbol{k}_2}{k_1^2k_2^2}\,. \tag{8.50}$$

Then the tree-level matter bispectrum $\langle\delta_{\rm T}\,\delta_{\rm T}\,\delta_{\rm T}^{(2)}\rangle$ at equal times is given by

$$\begin{aligned} B_m(\boldsymbol{k}_1,\boldsymbol{k}_2,\boldsymbol{k}_3) = \Bigg\{ & F_2(\boldsymbol{k}_1,\boldsymbol{k}_2) + 2f_{\rm NL}\frac{\mathcal{M}(k_3)}{\mathcal{M}(k_1)\mathcal{M}(k_2)} \\ & - \big(3\Omega_m + 2f\big)\mathcal{H}^2\,\frac{\left[2\left(k_1^2+k_2^2\right) - \boldsymbol{k}_1\cdot\boldsymbol{k}_2\right]}{2k_1^2k_2^2}\Bigg\} P(k_1)P(k_2) + 2\ {\rm cp}\,, \end{aligned} \tag{8.51}$$

where we omit the time dependence for brevity, and ‘cp’ denotes cyclic permutation.

Here $P \equiv P_{\rm T}$ is the linear matter power spectrum and

$$\frac{\mathcal{M}(k_3)}{\mathcal{M}(k_1)\mathcal{M}(k_2)} = \frac{3}{10}\big(3\Omega_m + 2f\big)\mathcal{H}^2 \,\frac{T(k_3)}{T(k_1)T(k_2)}\,\frac{k_3^2}{k_1^2 k_2^2}\,. \tag{8.52}$$

The standard Newtonian result (see e.g. Tellarini et al. (2015)) is modified in GR by the magenta terms in (8.51). For Gaussian initial conditions, the GR correction is suppressed by $\mathcal{H}^2/k^2$ relative to the Newtonian approximation, but *in the non-Gaussian case, the GR correction is of the same order of magnitude as the local PNG term.*

8.3.2. Observed number density

The observed number density contrast is $\Delta_g + \Delta_g^{(2)}/2$, which modifies the source quantity $\delta_g + \delta_g^{(2)}/2$ by RSD and other redshift space effects. It can be split into Newtonian, relativistic and non-Gaussian parts as follows.

- The **first order** parts are:

$$\Delta_{g\rm N} = b_{10}\delta_{\rm T,N} - \frac{1}{\mathcal{H}}\partial_\|^2 V\,, \tag{8.53}$$

$$\Delta_{g\rm nG} = b_{01}\varphi_{\rm p}\,, \tag{8.54}$$

$$\begin{aligned}\Delta_{g\rm GR} =& \Big[b_e - 2\mathcal{Q} + \frac{2\,(\mathcal{Q}-1)}{\chi\mathcal{H}} - \frac{\mathcal{H}'}{\mathcal{H}^2}\Big]\big(\partial_\| V - \Psi\big)\\ &+ (2\mathcal{Q}-1)\Psi + \frac{1}{\mathcal{H}}\Psi' + (3-b_e)\mathcal{H}V\,.\end{aligned} \tag{8.55}$$

  Recall that $\delta_{\rm T}$, V and Ψ have no GR and no PNG corrections, by (8.15) and (8.18).

- The **second-order Newtonian** part of the observed number density contrast is formed from the density contrast and RSD terms and their couplings:

$$\begin{aligned}\Delta_{g\rm N}^{(2)} =& \,\delta_{g\rm T,N}^{(2)} - \frac{1}{\mathcal{H}}\partial_\|^2 V_{\rm N}^{(2)}\\ &- 2\frac{b_{10}}{\mathcal{H}}\Big[\delta_{\rm T}\,\partial_\|^2 V + \partial_\| V\,\partial_\|\delta_{\rm T}\Big] + \frac{2}{\mathcal{H}^2}\Big[\big(\partial_\|^2 V\big)^2 + \partial_\| V\,\partial_\|^3 V\Big].\end{aligned} \tag{8.56}$$

- The **second-order relativistic** part is Jolicoeur et al. (2017, 2018):

$$\Delta_{g\rm GR}^{(2)} = \delta_{g\rm T,GR}^{(2)} - \frac{1}{\mathcal{H}}\partial_\|^2 V_{\rm GR}^{(2)} + \Big[b_e - 2\mathcal{Q} + \frac{2(\mathcal{Q}-1)}{\chi\mathcal{H}} - \frac{\mathcal{H}'}{\mathcal{H}^2}\Big]\Big[\partial_\| V_{\rm N+GR}^{(2)} - \Phi_{\rm N+GR}^{(2)}\Big]$$

$$+\,2(\mathcal{Q}-1)\Psi^{(2)}_{\rm N+GR} + \Phi^{(2)}_{\rm N+GR} + \frac{1}{\mathcal{H}}\Psi^{(2)\prime}_{\rm N+GR} + (3-b_e)\mathcal{H}V^{(2)}_{\rm N+GR}$$
$$+\,\text{very many terms quadratic in first-order quantities,} \tag{8.57}$$

where

$$V^{(2)}_{\rm N+GR} \equiv V^{(2)}_{\rm N} + V^{(2)}_{\rm GR}\,, \tag{8.58}$$

and similarly for the metric potentials.

The Newtonian parts of the metric potentials $\Psi^{(2)}, \Phi^{(2)}$ appear in the GR part of $\Delta^{(2)}_g$ because there is *no Newtonian projection effect involving these potentials*. For the velocity potential, the Newtonian part $V^{(2)}_{\rm N}$ is present only in the RSD term in (8.56); the remaining velocity terms occur *only in the GR part* of $\Delta^{(2)}_g$ and therefore $V^{(2)}_{\rm N}$ is included in the GR terms.

The quadratic terms in (8.57) are given in full by Jolicoeur et al. (2017). For convenience, Appendix REFERENCE APPENDIX presents all of the terms in (8.57), correcting some errors in Jolicoeur et al. (2017).

- The **second-order local PNG** part is

$$\Delta^{(2)}_{g\rm nG} = \delta^{(2)}_{g\rm T,nG} - \frac{1}{\mathcal{H}}\partial^2_\parallel V^{(2)}_{\rm nG}$$
$$+\left[b_e - 2\mathcal{Q} + \frac{2(\mathcal{Q}-1)}{\chi\mathcal{H}} - \frac{\mathcal{H}'}{\mathcal{H}^2}\right]\left[\partial_\parallel V^{(2)}_{\rm nG} - \Psi^{(2)}_{\rm nG}\right] + (2\mathcal{Q}-1)\Psi^{(2)}_{\rm nG} + \frac{1}{\mathcal{H}}\Psi^{(2)\prime}_{\rm nG} + (3-b_e)\mathcal{H}$$
$$-\,2\frac{b_{01}}{\mathcal{H}}\Big(\varphi_{\rm p}\,\partial^2_\parallel V + \partial_\parallel V\,\partial_\parallel\varphi_{\rm p}\Big)$$
$$+\,b_{01}\Big(c_1\Psi\varphi_{\rm p} + c_2 V\varphi_{\rm p} + c_3\varphi_{\rm p}\partial_\parallel V + c_4\Psi\partial_\parallel\varphi_{\rm p}\Big)\,. \tag{8.59}$$

In this expression, lines 1 and 2 contain the linearly evolved second-order terms whose nonlinearity is purely primordial. Lines 3 and 4 contain the quadratic coupling terms.

Line 1 is the Newtonian density + RSD part, given by (8.27) and (8.48).

Line 2 arises from *GR projection terms that are absent in the Newtonian approximation:* these terms are given by (8.44)–(8.48).

Line 3 arises from the first quadratic RSD term in line 2 of (8.56), given by the coupling of $\delta_{\rm T,nG}$ to velocity gradients.

Line 4 arises from the *coupling of* $\delta_{\rm T,nG}$ *to first-order GR projection terms.* The coefficients $c_I(a)$ are explicitly given below and in Appendix REFERENCE

APPENDIX.

Apart from the b_{02} term in $\delta^{(2)}_{g\mathrm{T,nG}}$, the Newtonian terms in (8.59) scale as $(\mathcal{H}^2/k^2)\,(\delta_\mathrm{T})^2$ and dominate the GR correction terms, which scale as $\mathrm{i}(\mathcal{H}^3/k^3)\,(\delta_\mathrm{T})^2$ or $(\mathcal{H}^4/k^4)\,(\delta_\mathrm{T})^2$.

In summary the local PNG part at second order has the following origins:

* the primordial matter density contrast;
* the scale-dependent bias;
* the linearly evolved second-order projection effects in velocity and metric potentials – from RSD and from GR corrections;
* the coupling of first-order scale-dependent bias with first-order projection effects – from RSD and from GR corrections.

8.3.3. Galaxy bispectrum

At leading order the observed galaxy bispectrum is defined by (Umeh et al., 2017)

$$2\big\langle \Delta_g(\boldsymbol{k}_1)\Delta_g(\boldsymbol{k}_2)\Delta_g^{(2)}(\boldsymbol{k}_3)\big\rangle + 2\ \mathrm{cp} = (2\pi)^3 B_g(\boldsymbol{k}_1,\boldsymbol{k}_2,\boldsymbol{k}_3)\delta^{\mathrm{Dirac}}(\boldsymbol{k}_1+\boldsymbol{k}_2+\boldsymbol{k}_3)\,, \tag{8.60}$$

where here, and below, we omit the time dependence for brevity and we assume equal-time correlations. The bispectrum can be written in terms of Fourier kernels as

$$B_g(\boldsymbol{k}_1,\boldsymbol{k}_2,\boldsymbol{k}_3) = \mathcal{K}(\boldsymbol{k}_1)\,\mathcal{K}(\boldsymbol{k}_2)\,\mathcal{K}^{(2)}(\boldsymbol{k}_1,\boldsymbol{k}_2,\boldsymbol{k}_3)\,P(k_1)P(k_2) + 2\ \mathrm{cp}, \tag{8.61}$$

where

$$\Delta_g(\boldsymbol{k}) = \mathcal{K}(\boldsymbol{k})\,\delta_\mathrm{T}(\boldsymbol{k})\,, \tag{8.62}$$

$$\Delta_g^{(2)}(\boldsymbol{k}_3) = \int \frac{\mathrm{d}\boldsymbol{k}_1}{(2\pi)^3}\,\mathrm{d}\boldsymbol{k}_2\,\delta^{\mathrm{Dirac}}(\boldsymbol{k}_1+\boldsymbol{k}_2-\boldsymbol{k}_3)\,\mathcal{K}^{(2)}(\boldsymbol{k}_1,\boldsymbol{k}_2,\boldsymbol{k}_3)\,\delta_\mathrm{T}(\boldsymbol{k}_1)\,\delta_\mathrm{T}(\boldsymbol{k}_2). \tag{8.63}$$

In (Jolicoeur et al., 2018), the Newtonian and GR kernels are presented, including all local relativistic effects, from projection, evolution and bias, but in the case of Gaussian initial conditions. Here we have updated these results and extended them to include the effects of local PNG. From Section 8.3.2, we find the following kernels.

- At **first order**, using (8.53)–(8.55) and (8.62):

$$\mathcal{K}_{\rm N}(\boldsymbol{k}_a) = b_{10} + f\mu_a^2\,, \tag{8.64}$$
$$\mathcal{K}_{\rm GR}(\boldsymbol{k}_a) = {\rm i}\,\mu_a\frac{\gamma_1}{k_a} + \frac{\gamma_2}{k_a^2}\,, \tag{8.65}$$
$$\mathcal{K}_{\rm nG}(\boldsymbol{k}_a) = \frac{b_{01}}{\mathcal{M}(k_a)}\,, \tag{8.66}$$

where $\mu_a = \hat{\boldsymbol{k}}_a \cdot \boldsymbol{n}$ and

$$\frac{\gamma_1}{\mathcal{H}} = f\left[b_e - 2\mathcal{Q} - \frac{2(1-\mathcal{Q})}{\chi\mathcal{H}} - \frac{\mathcal{H}'}{\mathcal{H}^2}\right], \tag{8.67}$$
$$\frac{\gamma_2}{\mathcal{H}^2} = f(3-b_e) + \frac{3}{2}\Omega_m\left[2 + b_e - f - 4\mathcal{Q} - \frac{2(1-\mathcal{Q})}{\chi\mathcal{H}} - \frac{\mathcal{H}'}{\mathcal{H}^2}\right]. \tag{8.68}$$

- The **second-order Newtonian part** follows from (8.56) and (8.63) (see e.g. Tellarini et al. (2016)):

$$\begin{aligned}\mathcal{K}_{\rm N}^{(2)}(\boldsymbol{k}_1,\boldsymbol{k}_2,\boldsymbol{k}_3) &= b_{10}F_2(\boldsymbol{k}_1,\boldsymbol{k}_2) + b_{20} + f\mu_3^2 G_2(\boldsymbol{k}_1,\boldsymbol{k}_2) + b_s S_2(\boldsymbol{k}_1,\boldsymbol{k}_2) \\ &\quad + b_{10} f\left(\mu_1 k_1 + \mu_2 k_2\right)\left(\frac{\mu_1}{k_1} + \frac{\mu_2}{k_2}\right) + f^2\frac{\mu_1\mu_2}{k_1k_2}\left(\mu_1 k_1 + \mu_2 k_2\right)^2,\end{aligned} \tag{8.69}$$

where

$$G_2(\boldsymbol{k}_1,\boldsymbol{k}_2) = \frac{F'}{DD'} + \left(\frac{k_1}{k_2} + \frac{k_2}{k_1}\right)\hat{\boldsymbol{k}}_1\cdot\hat{\boldsymbol{k}}_2 + \left(2 - \frac{F'}{DD'}\right)\left(\hat{\boldsymbol{k}}_1\cdot\hat{\boldsymbol{k}}_2\right)^2, \tag{8.70}$$
$$S_2(\boldsymbol{k}_1,\boldsymbol{k}_2) = \left(\hat{\boldsymbol{k}}_1\cdot\hat{\boldsymbol{k}}_2\right)^2 - \frac{1}{3}\,. \tag{8.71}$$

Since we use the approximation $F/D^2 = 3/7$ in F_2, we have $F'/(DD') = 6/7$ in G_2.

- The **second-order relativistic part** follows from (8.57) and (8.63) (see (Jolicoeur et al., 2018), with some errors that are corrected here):

$$\begin{aligned}\mathcal{K}_{\rm GR}^{(2)}(\boldsymbol{k}_1,\boldsymbol{k}_2,\boldsymbol{k}_3) = \frac{1}{k_1^2k_2^2}\Bigg\{&\beta_1 + E_2(\boldsymbol{k}_1,\boldsymbol{k}_2,\boldsymbol{k}_3)\,\beta_2 \\ &+ {\rm i}\left[\left(\mu_1k_1+\mu_2k_2\right)\beta_3 + \mu_3k_3\left(\beta_4 + E_2(\boldsymbol{k}_1,\boldsymbol{k}_2,\boldsymbol{k}_3)\,\beta_5\right)\right] \\ &+ \frac{k_1^2k_2^2}{k_3^2}\left[F_2(\boldsymbol{k}_1,\boldsymbol{k}_2)\,\beta_6 + G_2(\boldsymbol{k}_1,\boldsymbol{k}_2)\,\beta_7\right] + \left(\mu_1k_1\mu_2k_2\right)\beta_8\end{aligned} \tag{8.72}$$

$$
\begin{aligned}
&+\mu_3^2k_3^2\Big[\beta_9+E_2(\boldsymbol{k}_1,\boldsymbol{k}_2,\boldsymbol{k}_3)\,\beta_{10}\Big]+(\boldsymbol{k}_1\cdot\boldsymbol{k}_2)\,\beta_{11}\\
&+\left(k_1^2+k_2^2\right)\beta_{12}+\left(\mu_1^2k_1^2+\mu_2^2k_2^2\right)\beta_{13}\\
&+\mathrm{i}\,\Bigg[\left(\mu_1k_1^3+\mu_2k_2^3\right)\beta_{14}+(\mu_1k_1+\mu_2k_2)\,(\boldsymbol{k}_1\cdot\boldsymbol{k}_2)\,\beta_{15}\\
&+k_1k_2\,(\mu_1k_2+\mu_2k_1)\,\beta_{16}+\left(\mu_1^3k_1^3+\mu_2^3k_2^3\right)\beta_{17}\\
&+\mu_1\mu_2k_1k_2\,(\mu_1k_1+\mu_2k_2)\,\beta_{18}+\mu_3\frac{k_1^2k_2^2}{k_3}\,G_2(\boldsymbol{k}_1,\boldsymbol{k}_2)\,\beta_{19}\Bigg]\Bigg\},
\end{aligned}
$$

where

$$
E_2(\boldsymbol{k}_1,\boldsymbol{k}_2,\boldsymbol{k}_3)=\frac{k_1^2k_2^2}{k_3^4}\left[3+2\left(\frac{k_1}{k_2}+\frac{k_2}{k_1}\right)\hat{\boldsymbol{k}}_1\cdot\hat{\boldsymbol{k}}_2+\left(\hat{\boldsymbol{k}}_1\cdot\hat{\boldsymbol{k}}_2\right)^2\right]. \tag{8.73}
$$

The kernel (8.72) is derived from the many terms in $\Delta_g^{(2)}(\boldsymbol{x})$, as given in Bertacca et al. (2014a); Bertacca (2015) (we neglect the integrated terms). For convenience, in Table B.1, Appendix B, we summarise which terms in $\Delta_g^{(2)}(\boldsymbol{x})$ contribute to which of the terms in (8.72). The time-dependent functions β_I are also given in Appendix REF APPENDIX.

- The **second-order local PNG part** follows from (8.59):

$$
\begin{aligned}
\mathcal{K}^{(2)}_{\mathrm{nG}}(\boldsymbol{k}_1,\boldsymbol{k}_2,\boldsymbol{k}_3)&=2\,f_{\mathrm{NL}}\big(b_{10}+f\mu_3^2\big)\frac{\mathcal{M}_3}{\mathcal{M}_1\mathcal{M}_2}+fb_{01}\big(\mu_1k_1+\mu_2k_2\big)\left(\frac{\mu_1}{k_1\mathcal{M}_2}+\frac{\mu_2}{k_2\mathcal{M}_1}\right)\\
&+b_nN_2(\boldsymbol{k}_1,\boldsymbol{k}_2)+\frac{b_{11}}{2}\left(\frac{1}{\mathcal{M}_1}+\frac{1}{\mathcal{M}_2}\right)+\frac{b_{02}}{\mathcal{M}_1\mathcal{M}_2}\\
&+\frac{\mathcal{M}_3}{\mathcal{M}_1\mathcal{M}_2}\left(\frac{\Upsilon_1}{k_3^2}+\mathrm{i}\,\frac{\mu_3}{k_3}\,\Upsilon_2\right)+\Upsilon_3\left(\frac{1}{k_1^2\mathcal{M}_2}+\frac{1}{k_2^2\mathcal{M}_1}\right)\\
&+\mathrm{i}\,\left[\Upsilon_4\left(\frac{\mu_1k_1}{k_2^2\mathcal{M}_1}+\frac{\mu_2k_2}{k_1^2\mathcal{M}_2}\right)+\Upsilon_5\left(\frac{\mu_1}{k_1\mathcal{M}_2}+\frac{\mu_2}{k_2\mathcal{M}_1}\right)\right],
\end{aligned} \tag{8.74}
$$

where $\mathcal{M}_a\equiv\mathcal{M}(k_a)$ and

$$
N_2(\boldsymbol{k}_1,\boldsymbol{k}_2)=\frac{1}{2}\left(\frac{k_1}{k_2\mathcal{M}_1}+\frac{k_2}{k_1\mathcal{M}_2}\right)\hat{\boldsymbol{k}}_1\cdot\hat{\boldsymbol{k}}_2. \tag{8.75}
$$

In the first line of (8.74), the first term is a sum of the matter density term in line 2 of (8.27) and the linearly evolved PNG part of the second-order RSD term [line 1 of (8.59)]. The second term is the quadratic RSD term from line 3 of (8.59).

The second line gives the scale-dependent bias contribution from (8.27). The first two lines recover the Newtonian approximation (see Tellarini et al. (2015)).

Lines 3 and 4 in magenta are the PNG contributions that arise from relativistic projection effects, as explained in Section 8.3.2. These projection terms in the non-Gaussian kernel involve new time-dependent functions Υ_I, which are given in Appendix REFERENCE APPENDIX. The terms in $\Delta_g^{(2)}(\boldsymbol{x})$ corresponding to those in (8.74), lines 3 and 4, are summarised in Table C.1, Appendix REFERENCE APPENDIX.

The Newtonian terms scale as $(\mathcal{H}^2/k^2)\,(\delta_{\rm T})^2$ except for the b_{02} term which scales as $(\mathcal{H}^4/k^4)\,(\delta_{\rm T})^2$. The relativistic Υ_1, Υ_3 terms scale as $(\mathcal{H}^4/k^4)\,(\delta_{\rm T})^2$, while the $\Upsilon_2, \Upsilon_4, \Upsilon_5$ terms are $\mathcal{O}(\mathcal{H}^3/k^3)$.

Note that Υ_1, Υ_2 are proportional to $f_{\rm NL}$, and $\Upsilon_3, \Upsilon_4, \Upsilon_5$ are proportional to b_{01} (which itself is proportional to $f_{\rm NL}$).

For Gaussian initial conditions, $\mathcal{K}_{\rm nG}^{(2)}$ vanishes:

$$f_{\rm NL} = 0 \;\; \Rightarrow \;\; b_{01} = b_n = b_{11} = b_{02} = \Upsilon_I = 0 \;\; \Rightarrow \;\; \mathcal{K}_{\rm nG}^{(2)}(\boldsymbol{k}_1, \boldsymbol{k}_2, \boldsymbol{k}_3) = 0\,. \quad (8.76)$$

8.3.4. Numerical examples

The GR corrections to the Newtonian bispectrum, for both Gaussian and local PNG cases, are sensitive to the following astrophysical parameters of the tracer: Gaussian bias b_{10}, PNG bias b_{01}, and magnification bias $\mathcal{Q}$, together with their first derivatives in time and luminosity; evolution bias b_e and its first time derivative. This can be seen from the kernels presented above, with the details given in Appendices B and C.

In order to illustrate the GR corrections, we need to use physically self-consistent values for these parameters, as well as for the second-order Newtonian clustering bias parameters b_{20} and b_s. For a Stage IV Hα spectroscopic survey, similar to Euclid, we use Maartens et al. (2020) for the clustering biases, evolution bias and magnification bias. We neglect the luminosity derivatives of first-order clustering bias and magnification bias. For the PNG biases b_{11}, b_n, b_{02} we use (8.29)–(8.31).

We start by showing the contribution of GR corrections to the monopole of the reduced bispectrum,

$$Q_g^{00}(k_1, k_2, k_3) = \frac{B_g^{00}(k_1, k_2, k_3)}{P(k_1)P(k_2) + P(k_3)P(k_1) + P(k_2)P(k_3)}\,, \tag{8.77}$$

where de Weerd et al. (2020)

$$B_g^{\ell m}(k_1, k_2, k_3) = \int_0^{2\pi} \mathrm{d}\phi \int_{-1}^{1} \mathrm{d}\mu_1 B_g(k_1, k_2, k_3, \mu_1, \phi)\, Y_{\ell m}^*(\mu_1, \phi)\,. \tag{8.78}$$

Here ϕ, μ_1 determine the orientation of the triangle relative to the line of sight. Figure 8.2 shows the monopole for squeezed configurations. We use fixed equal sides $k_1 = k_2 = 0.1\,h/\text{Mpc}$ and varying long mode $k_3 < k_1 = k_2$. The isosceles triangle is increasingly squeezed as k_3 decreases. The left panel shows the Newtonian approximation (dash-dot lines) and the right panel shows the monopole without the GR bias correction (8.37).

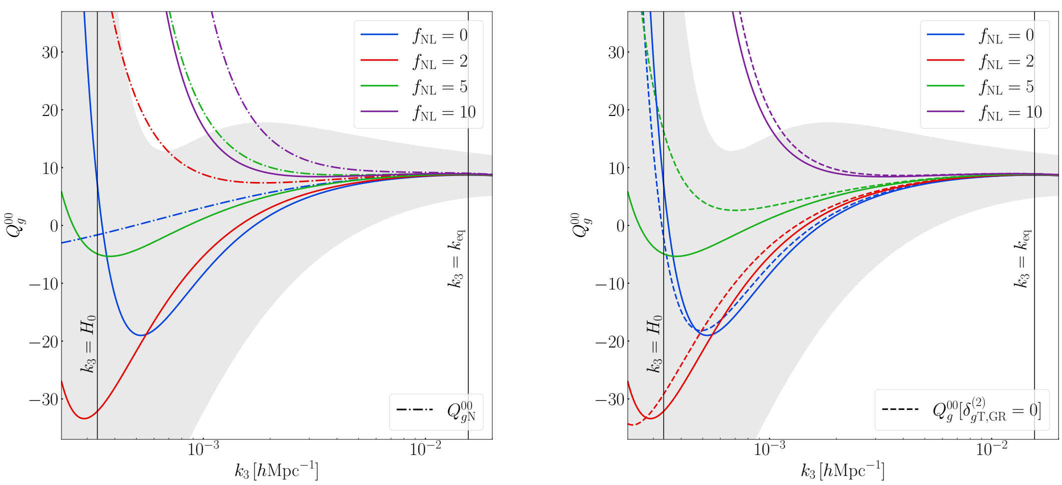

Figure 8.2.: Monopole of the reduced bispectrum for a Stage IV Hα survey at $z = 1$, for various $f_{\rm NL}$, with $k_1 = k_2 = 0.1\,h/\text{Mpc}$. Shading indicates the 1σ uncertainty (neglecting shot noise) for the $f_{\rm NL} = 0$ case (solid blue curve). *Left:* Comparing the full relativistic monopole to the Newtonian approximation (dash-dot curves). *Right:* Comparing the full relativistic monopole to the monopole without the GR correction to second-order galaxy bias, (8.32) (dashed curves).

The shading in Figure 8.2 is defined by the cosmic variance limited error σ_B on the

$f_{\rm NL}=0$ monopole, given by Gagrani & Samushia (2017):

$$\left(\sigma_B\right)^2=\frac{\mathcal{V}^{\,\rm com}}{\pi k_1k_2k_3\,\Delta k}\int \mathrm{d}\mu_1\,\mathrm{d}\phi\,P_g(k_1,\mu_1)\,P_g(k_2,\mu_2)\,P_g(k_3,\mu_3)\,, \tag{8.79}$$

where the galaxy power spectrum, from (8.64)–(8.66), is

$$P_g(k_a,\mu_a)=\left|b_{10}+f\mu_a^2+\frac{\gamma_2}{k_a^2}+\mathrm{i}\;\mu_a\frac{\gamma_1}{k_a}\right|^2P(k_a)\,. \tag{8.80}$$

In (8.79), $\mathcal{V}^{\,\rm com}$ is the comoving volume of the redshift bin, Δk is chosen as the fundamental mode, $2\pi(\mathcal{V}^{\,\rm com})^{-1/3}$, $k_1=k_2=0.1\,h/\mathrm{Mpc}$, and Clarkson et al. (2019) $\mu_2=\mu_1\cos\theta_{12}+\sqrt{1-\mu_1^2}\sin\theta_{12}\,\cos\phi,\ \mu_3=-(k_1\mu_1+k_2\mu_2)/k_3$. Here θ_{12} is the tail-to-tail angle between $\boldsymbol{k}_1$ and $\boldsymbol{k}_2$, so that the squeezed limit is $\theta_{12}=\pi$.

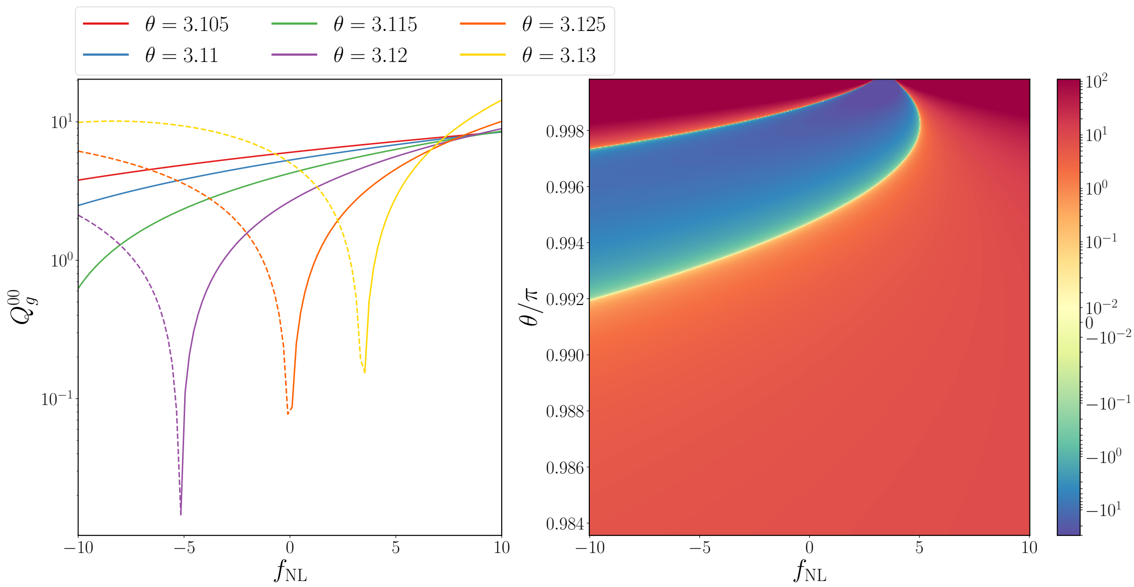

Figure 8.3.: Monopole of reduced bispectrum for isosceles triangles, as in Figure 8.2. *Left:* As a function of $f_{\rm NL}$, for various values of $\theta\equiv\theta_{12}$, where $\theta=\pi$ is the squeezed limit. Dashed curves indicate negative values. *Right:* 2D colour map as a function of $f_{\rm NL}$ and θ/π.

The effect of $f_{\rm NL}$ is strongest in the monopole and competes with the GR contribution on ultra-large scales, since they both affect the Newtonian Gaussian bispectrum at $\mathcal{O}(\mathcal{H}^2/k^2)$. We see this in Figure 8.2 left panel, which shows the monopole of the reduced bispectrum for an increasingly squeezed isosceles triangle. In the Gaussian case (blue) we see that the Newtonian reduced monopole (dot-dash blue) becomes negative when the long mode is close to the Hubble scale, due to the effects of second-order galaxy bias. The Gaussian GR correction to the Newtonian approx-

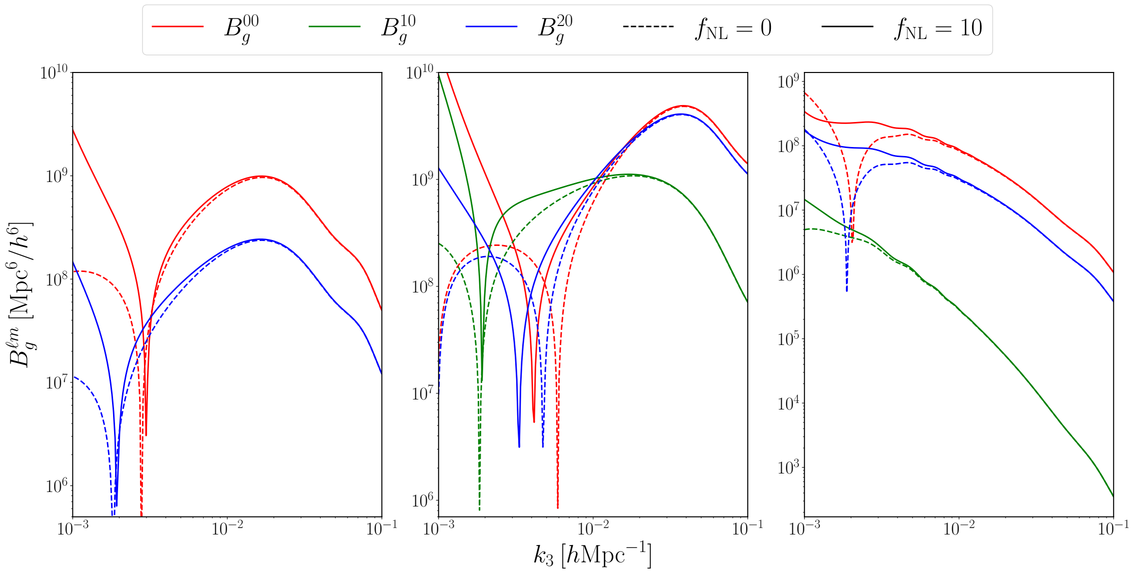

Figure 8.4.: First few nonzero multipoles for fixed triangle shape as a function of k_3, with $f_{\rm NL} = 10$ (solid) and $f_{\rm NL} = 0$ (dashed). *Left:* Equilateral configuration, $k_1 = k_2 = k_3$. *Middle:* Flattened configuration, $k_1 = k_2 \approx k_3/2$, with $\theta_{12} = 2°$. *Right:* Squeezed configuration with $\theta_{12} = 178°$ and $k_1 = k_2 = k_3/(2\sin\theta_{12}) \approx 14\, k_3$.

imation is negative for super-equality long modes until close to the Hubble scale (this was pointed out in Jolicoeur et al. (2019)). GR effects drive the reduced monopole (solid blue) below zero for $H_0 \lesssim k_3 \lesssim 0.002\, h/\text{Mpc}$ (the locations of the zero-crossings are dependent on the Gaussian bias parameters, evolution bias and magnification bias).

As $f_{\rm NL}$ is increased above zero, the amplitude of the Newtonian reduced monopole (dot-dash curves) increases monotonically. When GR effects are taken into account, the reduced monopole is pushed upwards, but remains negative on observable scales for $f_{\rm NL} \lesssim 5$, until it becomes always positive for $f_{\rm NL} > 5$ – the precise turnaround value of $f_{\rm NL}$ depends on astrophysical parameters. This means that for $f_{\rm NL} \lesssim 5$, local PNG *decreases* the amplitude of the reduced monopole on observable scales, in contrast to the Newtonian approximation. Comparing the green solid and blue dot-dash curves shows that *the Newtonian approximation is very close to the true reduced monopole with $f_{NL} \sim 5$*. For a universe with $f_{\rm NL} \sim 5$, a Newtonian analysis of the squeezed bispectrum would conclude that the primordial universe is Gaussian. Similarly, a universe with $f_{\rm NL} \sim 10$ would appear to have $f_{\rm NL} \sim 5$ in a Newtonian approximation.

The GR contribution to the monopole is made up of: $\mathcal{O}(\mathcal{H}^2/k^2)$ Gaussian projection terms, $\mathcal{O}(\mathcal{H}^2/k^2)$ second-order galaxy bias correction (the same for Gaussian and PNG cases) and $\mathcal{O}(\mathcal{H}^4/k^4)$ second-order local PNG contributions from GR projection effects. The last contribution is effectively negligible on observable scales. In the right panel of Figure 8.2 we show that the GR bias correction is dominated by the Gaussian GR projection terms: the effect of removing the GR correction to second-order galaxy bias is small. Note that the GR bias correction has a similar effect to a small negative value of $f_{\rm NL}$.

In Figure 8.3 we include negative $f_{\rm NL}$ and explore how local PNG changes the monopole of the reduced bispectrum as we approach the squeezed limit, $\theta_{12} \to \pi$. For $f_{\rm NL} \geq 0$, the results provide a different perspective on Figure 8.2 left panel. For negative $f_{\rm NL}$, local PNG and GR effects act together to drive the monopole negative, so that the zero-crossing of the monopole occurs for smaller θ_{12}, equivalently larger k_3.

Figure 8.4 shows the effect of $f_{\rm NL}$ on the first three multipoles of the relativistic galaxy bispectrum, also including equilateral and flattened triangle shapes. In general, the Newtonian RSD effect induces only even multipoles, while the GR corrections modify the even multipoles and induce new odd multipoles. We show here the $m = 0$ dipole (absent without GR corrections) and quadrupole (mainly Newtonian), compared to the monopole.

For the equilateral shape (left panel), the dipole vanishes exactly in the Gaussian case Clarkson et al. (2019); de Weerd et al. (2020) and nonzero $f_{\rm NL}$ does not changes this result. The effect of $f_{\rm NL}$ on the quadrupole is very similar to the case of the monopole.

For the flattened shape (middle panel), the dipole is the dominant part of the bispectrum for $0.002 \lesssim k_3/(h\mathrm{Mpc}^{-1}) \lesssim 0.01$, and we see that $f_{\rm NL} > 0$ increases this effect further. The dipole B_g^{1m} is purely relativistic: it vanishes in the Newtonian approximation Clarkson et al. (2019); Maartens et al. (2020); Jolicoeur et al. (2020).

Finally, in the squeezed case (right panel), the effect on the monopole of $f_{\rm NL} = 10$ is consistent with Figure 8.2. The quadrupole has a similar behaviour, and dominates the dipole. It is interesting that the three multipoles are approximately equal at scales near $k = 0.002\,h/\mathrm{Mpc}$. Once again, this value is sensitive to astrophysical parameters.

8.4. Conclusions

Upcoming galaxy surveys and 21cm intensity mapping surveys will deliver high-precision cosmological measurements and constraints, based on a combination of the power spectrum and bispectrum. This advance demands a commensurate advance in theoretical precision. Here we contribute to the development of theoretical precision by deriving for the first time the local relativistic corrections to the tree-level redshift-space bispectrum in the presence of local primordial non-Gaussianity (PNG).

At first order in perturbations, there are no relativistic corrections to the comoving matter and galaxy density contrasts – and therefore no correction to the galaxy clustering bias relation. There are also no relativistic corrections to the velocity and metric potentials. Consequently, there is no relativistic contribution to local PNG. The only relativistic correction is to the Newtonian projection effect, i.e. standard redshift-space distortions (RSD).

At second-order, relativistic corrections go beyond projection effects to alter the galaxy bias relation and local PNG in the galaxy bispectrum. In summary, there are:

- relativistic projection corrections to the Newtonian RSD at first and second order;
- relativistic corrections to the Newtonian bias model in the comoving frame at second order;
- second-order relativistic projection corrections to the local PNG carried by Newtonian RSD – from a coupling of first-order scale-dependent bias to first-order relativistic projection effects, and from the linearly evolved local PNG in second-order velocity and metric potentials.

Our previous work Umeh et al. (2017); Jolicoeur et al. (2017, 2018, 2019); Clarkson et al. (2019); Maartens et al. (2020); de Weerd et al. (2020); Jolicoeur et al. (2020) presented local (non-integrated) relativistic effects in the case of primordial Gaussianity and without the relativistic correction to galaxy bias. We have made corrections to these earlier results. In addition, we have presented for the first time the galaxy bispectrum with relativistic corrections to galaxy clustering bias and new local PNG contributions that are encoded in relativistic projection effects. Our main results are given in Fourier space in (8.69)–(8.74), with further details in Appendices B and C.

In Figures 8.2 and 8.3 we show examples of the squeezed monopole of the reduced relativistic bispectrum for a Stage IV Hα survey similar to Euclid, using physical models for the astrophysical parameters (clustering biases, evolution bias, magnification bias). These figures reveal various interesting relativistic features. In particular, they show the bias in the estimate of $f_{\rm NL}$ from using a Newtonian analysis. This bias is given by

$$f_{\rm NL}^{\rm Newt} = f_{\rm NL} + \Delta f_{\rm NL}\,. \tag{8.81}$$

For the Stage IV survey at $z = 1$, the bias can be roughly estimated by eye as $\Delta f_{\rm NL} \sim 5$, for the long mode above the equality scale. Although the precise level of bias is sensitive to astrophysical parameters and redshift, the point is that next-generation precision demands that relativistic corrections are included in the bispectrum.

In common with nearly all work on the Fourier-space bispectrum with RSD and PNG, we implicitly make a flat-sky assumption, based on the fixed global direction $\boldsymbol{n}$. As a consequence, wide-angle correlations are not included, so that the flat-sky analysis loses accuracy as θ increases, where θ is the maximum opening angle to the three-point correlations at the given redshift. This leads to a systematic bias in the separation of observational effects from the PNG signal, and therefore in the best-fit value of $f_{\rm NL}$. Including wide-angle effects is a key target for future work. Corrections to the global flat-sky analysis of the Fourier bispectrum can be made by using a local or 'moving' line of sight Scoccimarro (2015); Sugiyama et al. (2018); Shirasaki et al. (2021). However, corrections of this type are approximate and do not incorporate all the wide-angle effects. Ultimately, one needs to use the full-sky 3-point correlation function or the full-sky angular bispectrum (see e.g. Kehagias et al. (2015); Di Dio et al. (2017, 2019); Durrer et al. (2020)) to properly include all wide-angle correlations. A major problem is that both of these alternatives are computationally more intensive.

9. Fisher Forecasts

Fisher forecast chapter

10. Summary

summary

mortuus in anima
curam gero cutis

A. Beta coefficients

$$
\begin{aligned}
\frac{\beta_1}{\mathcal{H}^4} = \frac{9}{4}\Omega_m^2\Bigg[& 6 - 2f\left(2b_e - 4\mathcal{Q} - \frac{4(1-\mathcal{Q})}{\chi\mathcal{H}} - \frac{2\mathcal{H}'}{\mathcal{H}^2}\right) - \frac{2f'}{\mathcal{H}} + b_e^2 + 5b_e - 8b_e\mathcal{Q} + 4\mathcal{Q} + 16\mathcal{Q}^2 \\
& - 16\frac{\partial\mathcal{Q}}{\partial\ln\bar{L}} - 8\frac{\mathcal{Q}'}{\mathcal{H}} + \frac{b_e'}{\mathcal{H}} + \frac{2}{\chi^2\mathcal{H}^2}\left(1 - \mathcal{Q} + 2\mathcal{Q}^2 - 2\frac{\partial\mathcal{Q}}{\partial\ln\bar{L}}\right) \\
& - \frac{2}{\chi\mathcal{H}}\left(3 + 2b_e - 2b_e\mathcal{Q} - 3\mathcal{Q} + 8\mathcal{Q}^2 - \frac{3\mathcal{H}'}{\mathcal{H}^2}(1-\mathcal{Q}) - 8\frac{\partial\mathcal{Q}}{\partial\ln\bar{L}} - 2\frac{\mathcal{Q}'}{\mathcal{H}}\right) \\
& + \frac{\mathcal{H}'}{\mathcal{H}^2}\left(-7 - 2b_e + 8\mathcal{Q} + \frac{3\mathcal{H}'}{\mathcal{H}^2}\right) - \frac{\mathcal{H}''}{\mathcal{H}^3}\Bigg] \\
& + \frac{3}{2}\Omega_m f\Bigg[5 - 2f(4 - b_e) + \frac{2f'}{\mathcal{H}} + 2b_e\left(5 + \frac{2(1-\mathcal{Q})}{\chi\mathcal{H}}\right) - \frac{2b_e'}{\mathcal{H}} - 2b_e^2 + 8b_e\mathcal{Q} - 28\mathcal{Q} \\
& - \frac{14(1-\mathcal{Q})}{\chi\mathcal{H}} - \frac{3\mathcal{H}'}{\mathcal{H}^2} + 4\left(2 - \frac{1}{\chi\mathcal{H}}\right)\frac{\mathcal{Q}'}{\mathcal{H}}\Bigg] \\
& + \frac{3}{2}\Omega_m f^2\left[-2 + 2f - b_e + 4\mathcal{Q} + \frac{2(1-\mathcal{Q})}{\chi\mathcal{H}} + \frac{3\mathcal{H}'}{\mathcal{H}^2}\right] \\
& + f^2\left[12 - 7b_e + b_e^2 + \frac{b_e'}{\mathcal{H}} + (b_e - 3)\frac{\mathcal{H}'}{\mathcal{H}^2}\right] - \frac{3}{2}\Omega_m\frac{f'}{\mathcal{H}}
\end{aligned}
\tag{A.1}
$$

$$
\begin{aligned}
\frac{\beta_2}{\mathcal{H}^4} = & \frac{9}{2}\Omega_m^2\left[-1 + b_e - 2\mathcal{Q} - \frac{2(1-\mathcal{Q})}{\chi\mathcal{H}} - \frac{\mathcal{H}'}{\mathcal{H}^2}\right] + 3\Omega_m f\left[-1 + 2f - b_e + 4\mathcal{Q} + \frac{2(1-\mathcal{Q})}{\chi\mathcal{H}} + 3\ldots\right. \\
& + 3\Omega_m f^2\left[-1 + b_e - 2\mathcal{Q} - \frac{2(1-\mathcal{Q})}{\chi\mathcal{H}} - \frac{\mathcal{H}'}{\mathcal{H}^2}\right] + 3\Omega_m\frac{f'}{\mathcal{H}}
\end{aligned}
\tag{A.2}
$$

$$
\begin{aligned}
\frac{\beta_3}{\mathcal{H}^3} = & \frac{9}{4}\Omega_m^2(f - 2 + 2\mathcal{Q}) \\
& + \frac{3}{2}\Omega_m f\Bigg[-2 - f\left(-3 + f + 2b_e - 3\mathcal{Q} - \frac{4(1-\mathcal{Q})}{\chi\mathcal{H}} - \frac{2\mathcal{H}'}{\mathcal{H}^2}\right) - \frac{f'}{\mathcal{H}} \\
& + 3b_e + b_e^2 - 6b_e\mathcal{Q} + 4\mathcal{Q} + 8\mathcal{Q}^2 - 8\frac{\partial\mathcal{Q}}{\partial\ln\bar{L}} - 6\frac{\mathcal{Q}'}{\mathcal{H}} + \frac{b_e'}{\mathcal{H}} \\
& + \frac{2}{\chi^2\mathcal{H}^2}\left(1 - \mathcal{Q} + 2\mathcal{Q}^2 - 2\frac{\partial\mathcal{Q}}{\partial\ln\bar{L}}\right) + \frac{2}{\chi\mathcal{H}}\Bigg(-1 - 2b_e + 2b_e\mathcal{Q} + \mathcal{Q} - 6\mathcal{Q}^2
\end{aligned}
$$

$$
\begin{aligned}
&+\frac{3\mathcal{H}'}{\mathcal{H}^2}(1-\mathcal{Q})+6\frac{\partial\mathcal{Q}}{\partial\ln\bar{L}}+2\frac{\mathcal{Q}'}{\mathcal{H}}\bigg)-\frac{\mathcal{H}'}{\mathcal{H}^2}\bigg(3+2b_e-6\mathcal{Q}-\frac{3\mathcal{H}'}{\mathcal{H}^2}\bigg)-\frac{\mathcal{H}''}{\mathcal{H}^3}\bigg]\\
&+f^2\bigg[-3+2b_e\bigg(2+\frac{(1-\mathcal{Q})}{\chi\mathcal{H}}\bigg)-b_e^2+2b_e\mathcal{Q}-6\mathcal{Q}-\frac{b_e'}{\mathcal{H}}-\frac{6(1-\mathcal{Q})}{\chi\mathcal{H}}\\
&+2\bigg(1-\frac{1}{\chi\mathcal{H}}\bigg)\frac{\mathcal{Q}'}{\mathcal{H}}\bigg]
\end{aligned}
\tag{A.3}
$$

$$
\frac{\beta_4}{\mathcal{H}^3}=\frac{9}{2}\Omega_m f\bigg[-b_e+2\mathcal{Q}+\frac{2(1-\mathcal{Q})}{\chi\mathcal{H}}+\frac{\mathcal{H}'}{\mathcal{H}^2}\bigg] \tag{A.4}
$$

$$
\frac{\beta_5}{\mathcal{H}^3}=3\Omega_m f\bigg[b_e-2\mathcal{Q}-\frac{2(1-\mathcal{Q})}{\chi\mathcal{H}}-\frac{\mathcal{H}'}{\mathcal{H}^2}\bigg] \tag{A.5}
$$

$$
\frac{\beta_6}{\mathcal{H}^2}=\frac{3}{2}\Omega_m\bigg[2-2f+b_e-4\mathcal{Q}-\frac{2(1-\mathcal{Q})}{\chi\mathcal{H}}-\frac{\mathcal{H}'}{\mathcal{H}^2}\bigg] \tag{A.6}
$$

$$
\frac{\beta_7}{\mathcal{H}^2}=f(3-b_e) \tag{A.7}
$$

$$
\begin{aligned}
\frac{\beta_8}{\mathcal{H}^2}&=3\Omega_m f(2-f-2\mathcal{Q})+f^2\bigg[4+b_e-b_e^2+4b_e\mathcal{Q}-6\mathcal{Q}-4\mathcal{Q}^2+4\frac{\partial\mathcal{Q}}{\partial\ln\bar{L}}+4\frac{\mathcal{Q}'}{\mathcal{H}}-\frac{b_e'}{\mathcal{H}}\\
&-\frac{2}{\chi^2\mathcal{H}^2}\bigg(1-\mathcal{Q}+2\mathcal{Q}^2-2\frac{\partial\mathcal{Q}}{\partial\ln\bar{L}}\bigg)-\frac{2}{\chi\mathcal{H}}\bigg(3-2b_e+2b_e\mathcal{Q}-\mathcal{Q}-4\mathcal{Q}^2+\frac{3\mathcal{H}'}{\mathcal{H}^2}(1-\mathcal{Q})\\
&+4\frac{\partial\mathcal{Q}}{\partial\ln\bar{L}}+2\frac{\mathcal{Q}'}{\mathcal{H}}\bigg)-\frac{\mathcal{H}'}{\mathcal{H}^2}\bigg(3-2b_e+4\mathcal{Q}+\frac{3\mathcal{H}'}{\mathcal{H}^2}\bigg)+\frac{\mathcal{H}''}{\mathcal{H}^3}\bigg]
\end{aligned}
\tag{A.8}
$$

$$
\frac{\beta_9}{\mathcal{H}^2}=-\frac{9}{2}\Omega_m f \tag{A.9}
$$

$$
\frac{\beta_{10}}{\mathcal{H}^2}=3\Omega_m f \tag{A.10}
$$

$$
\frac{\beta_{11}}{\mathcal{H}^2}=3\Omega_m\bigg(\frac{1}{2}+f\bigg)+f-f^2\bigg[-1+b_e-2\mathcal{Q}-\frac{2(1+\mathcal{Q})}{\chi\mathcal{H}}-\frac{\mathcal{H}'}{\mathcal{H}^2}\bigg] \tag{A.11}
$$

$$
\begin{aligned}
\frac{\beta_{12}}{\mathcal{H}^2}&=\frac{3}{2}\Omega_m\bigg[-2+b_1\bigg(2+b_e-4\mathcal{Q}-\frac{2(1-\mathcal{Q})}{\chi\mathcal{H}}-\frac{\mathcal{H}'}{\mathcal{H}^2}\bigg)+\frac{b_1'}{\mathcal{H}}+2\bigg(2-\frac{1}{\chi\mathcal{H}}\bigg)\frac{\partial b_1}{\partial\ln\bar{L}}\bigg]\\
&-f\bigg[2+b_1(f-3+b_e)+\frac{b_1'}{\mathcal{H}}\bigg]
\end{aligned}
\tag{A.12}
$$

$$
\frac{\beta_{13}}{\mathcal{H}^2}=\frac{9}{4}\Omega_m^2+\frac{3}{2}\Omega_m f\bigg[1-2f+2b_e-6\mathcal{Q}-\frac{4(1-\mathcal{Q})}{\chi\mathcal{H}}-\frac{3\mathcal{H}'}{\mathcal{H}^2}\bigg]+f^2(3-b_e) \tag{A.13}
$$

$$
\frac{\beta_{14}}{\mathcal{H}}=-\frac{3}{2}\Omega_m b_1 \tag{A.14}
$$

$$
\frac{\beta_{15}}{\mathcal{H}}=2f^2 \tag{A.15}
$$

$$\frac{\beta_{16}}{\mathcal{H}} = f\left[b_1\left(f + b_e - 2\mathcal{Q} - \frac{2(1-\mathcal{Q})}{\chi\mathcal{H}} - \frac{\mathcal{H}'}{\mathcal{H}^2}\right) + \frac{b_1'}{\mathcal{H}} + 2\left(1 - \frac{1}{\chi\mathcal{H}}\right)\frac{\partial b_1}{\partial \ln \bar{L}}\right] \tag{A.16}$$

$$\frac{\beta_{17}}{\mathcal{H}} = -\frac{3}{2}\Omega_m f \tag{A.17}$$

$$\frac{\beta_{18}}{\mathcal{H}} = \frac{3}{2}\Omega_m f - f^2\left[3 - 2b_e + 4\mathcal{Q} + \frac{4(1-\mathcal{Q})}{\chi\mathcal{H}} + \frac{3\mathcal{H}'}{\mathcal{H}^2}\right] \tag{A.18}$$

$$\frac{\beta_{19}}{\mathcal{H}} = f\left[b_e - 2Q - \frac{2(1-\mathcal{Q})}{\chi\mathcal{H}} - \frac{\mathcal{H}'}{\mathcal{H}^2}\right] \tag{A.19}$$

B. Beta coefficient tables

Table B.1.: Individual terms in the observed $\Delta_g^{(2)}(a, \boldsymbol{x})$ [see (8.56), (8.57)] for $f_{\rm NL} = 0$ are shown in column 1. The related β_I functions in (8.72) are listed in column 2. The Fourier-space kernels $\mathcal{F}$ corresponding to column 1, given by $\int \mathrm{d}\boldsymbol{k}'\, \mathcal{F}(\boldsymbol{k}', \boldsymbol{k}-\boldsymbol{k}')\delta_{\rm T}(\boldsymbol{k}')\delta_{\rm T}(\boldsymbol{k}-\boldsymbol{k}')/(2\pi)^3$, are shown in column 3. Column 4 gives the coefficients of the terms in $\Delta_g^{(2)}$ (column 1). The line-of-sight derivative is $\partial_\| = \boldsymbol{n}\cdot\boldsymbol{\nabla}$ and $\Phi = \Psi$. The superscript (1) on first-order quantities has been omitted and N denotes Newtonian. This table updates the one in Jolicoeur et al. (2017).

TERM	β	FOURIER KERNEL	COEFFICIENT
$\delta^{(2)}_{\rm T,N}$	N	$F_2(\boldsymbol{k}_1,\boldsymbol{k}_2)$	b_{10}
$(\delta_{\rm T})^2$	N	1	b_{20}
s^2	N	$S_2(\boldsymbol{k}_1,\boldsymbol{k}_2)$	b_s
$\partial_\|^2 V_{\rm N}^{(2)}$	N	$f^2\mathcal{H}\mu_3^2 G_2(\boldsymbol{k}_1,\boldsymbol{k}_2)$	$-1/\mathcal{H}$
$\delta_{\rm T}\partial_\|^2 V$	N	$-f\mathcal{H}(\mu_1^2+\mu_2^2)/2$	$-2b_{10}/\mathcal{H}$
$\partial_\| V\partial_\|\delta_{\rm T}$	N	$-f\mathcal{H}\mu_1\mu_2(k_1^2+k_2^2)/(2k_1k_2)$	$-2b_{10}/\mathcal{H}$
$\partial_\| V\partial_\|^3 V$	N	$f^2\mathcal{H}^2(\mu_1\mu_2^3k_2^2+\mu_2\mu_1^3k_1^2)/(k_1k_2)$	$2/\mathcal{H}^2$
$[\partial_\|^2 V]^2$	N	$f^2\mathcal{H}^2\,\mu_1^2\mu_2^2$	$2/\mathcal{H}^2$
$(\Psi)^2$	β_1	$9\Omega_m^2\mathcal{H}^4/(4k_1^2k_2^2)$	$\mathcal{A}_1$
ΨV	β_1	$-3\Omega_m\mathcal{H}^3 f/(2k_1^2k_2^2)$	$\mathcal{A}_2$
VV'	β_1	$f\mathcal{H}^3(3\Omega_m-2f)/(2k_1^2k_2^2)$	$(b_e-3)\mathcal{H}$
$(V)^2$	β_1	$f^2\mathcal{H}^2/(k_1^2k_2^2)$	$(b_e-3)^2\mathcal{H}^2+b_e'\mathcal{H}+(b_e-3)\mathcal{H}'$
$V^{(2)}_{\rm GR}$	β_1,β_2	$-3\Omega_m\mathcal{H}^3[3-2E_2(\boldsymbol{k}_1,\boldsymbol{k}_2,\boldsymbol{k}_3)]/(4k_1^2k_2^2)$	$(3-b_e)\mathcal{H}$
$\Phi^{(2)}_{\rm GR}$	β_1,β_2	$3\Omega_m\mathcal{H}^4[f-\mathcal{C}_1+\mathcal{C}_1E_2(\boldsymbol{k}_1,\boldsymbol{k}_2,\boldsymbol{k}_3)]/(2k_1^2k_2^2)$	$1-b_e+2\mathcal{Q}+\mathcal{R}$
$\Psi^{(2)}_{\rm GR}$	β_1,β_2	$3\Omega_m\mathcal{H}^4[\mathcal{C}_1-3f+2f^2+2fE_2(\boldsymbol{k}_1,\boldsymbol{k}_2,\boldsymbol{k}_3)]/(2k_1^2k_2^2)$	$2(\mathcal{Q}-1)$
$\Psi^{(2)\prime}_{\rm GR}$	β_1,β_2	$3\Omega_m\mathcal{H}^5[\mathcal{C}_2+\mathcal{C}_3E_2(\boldsymbol{k}_1,\boldsymbol{k}_2,\boldsymbol{k}_3)]/(2k_1^2k_2^2)$	$1/\mathcal{H}$
$V\partial_\| V$	β_3	$\mathrm{i}\,f^2\mathcal{H}^2(\mu_1k_1+\mu_2k_2)/(2k_1^2k_2^2)$	$\mathcal{A}_3$
$\Psi\partial_\| V$	β_3	$-\mathrm{i}\ 3f\Omega_m\mathcal{H}^3\,(\mu_1k_1+\mu_2k_2)/(4k_1^2k_2^2)$	$\mathcal{A}_4$
$\Psi\partial_\|\Phi$	β_3	$\mathrm{i}\ 9\Omega_m^2\mathcal{H}^4(\mu_1k_1+\mu_2k_2)/(8k_1^2k_2^2)$	$2(f-2+2\mathcal{Q})/\mathcal{H}$

$\partial_\parallel V_{\rm GR}^{(2)}$	β_4, β_5	$-\mathrm{i}\,3\Omega_m \mathcal{H}^3 [3 - 2E_2(\boldsymbol{k}_1,\boldsymbol{k}_2,\boldsymbol{k}_3)]\mu_3 k_3/(4k_1^2k_2^2)$	$b_e - 2\mathcal{Q} - \mathcal{R}$
$\Psi_{\rm N}^{(2)} = \Phi_{\rm N}^{(2)}$ $\Psi_{\rm N}^{(2)\prime} = \Phi_{\rm N}^{(2)\prime}$	β_6 β_6	$-3\Omega_m \mathcal{H}^2 F_2(\boldsymbol{k}_1,\boldsymbol{k}_2)/(2k_3^2)$ $-3\Omega_m \mathcal{H}^3 (2f-1) F_2(\boldsymbol{k}_1,\boldsymbol{k}_2)/(2k_3^2)$	$4\mathcal{Q} - 1 - b_e + \mathcal{R}$ $1/\mathcal{H}$
$V_{\rm N}^{(2)}$	β_7	$f\mathcal{H} G_2(\boldsymbol{k}_1,\boldsymbol{k}_2)/k_3^2$	$(3 - b_e)\mathcal{H}$
$(\partial_\parallel V)^2$ $\partial_\parallel V \partial_\parallel \Psi$	β_8 β_8	$-f^2\mathcal{H}^2 \mu_1\mu_2/(k_1k_2)$ $3f\Omega_m\mathcal{H}^3\mu_1\mu_2/(2k_1k_2)$	$\mathcal{A}_5$ $2(2 - f - 2\mathcal{Q})/\mathcal{H}$
$\partial_\parallel^2 V_{\rm GR}^{(2)}$	β_9, β_{10}	$\mathrm{i}\,3\Omega_m \mathcal{H}^3 [3 - 2E_2(\boldsymbol{k}_1,\boldsymbol{k}_2,\boldsymbol{k}_3)]\mu_3^2 k_3^2/(4k_1^2k_2^2)$	$-1/\mathcal{H}$
$\partial_i V\, \partial^i V$ $\partial_i V \partial^i \Psi$	β_{11} β_{11}	$-f^2\mathcal{H}^2\, \boldsymbol{k}_1\cdot\boldsymbol{k}_2/(k_1^2k_2^2)$ $3f\Omega_m\mathcal{H}^3\, \boldsymbol{k}_1\cdot\boldsymbol{k}_2/(2k_1^2k_2^2)$	$b_e - 1 - 2\mathcal{Q} - \mathcal{R}$ $2/\mathcal{H}$
$\Psi\delta_{\rm T}$ $V\delta_{\rm T}$	β_{12} β_{12}	$-3\Omega_m\mathcal{H}^2(k_1^2+k_2^2)/(4k_1^2k_2^2)$ $f\mathcal{H}(k_1^2+k_2^2)/(2k_1^2k_2^2)$	$2b_{10}(4\mathcal{Q} + \mathcal{R} - 2 - b_e) - \mathcal{S}$ $b_{10}' + 2b_{10}(3 - b_e - f)\mathcal{H}$
$\delta_{g{\rm T,GR}}^{(2)}$	β_{11}, β_{12}	$(3\Omega_m + 2f)\mathcal{H}^2[\boldsymbol{k}_1\cdot\boldsymbol{k}_2 - 2(k_1^2+k_2^2)]/(2k_1k_2)$	1
$\Psi\partial_\parallel^2 V$ $\Psi\partial_\parallel^2\Psi$ $V\partial_\parallel^2 V$ $\Psi\partial_\parallel\delta_{\rm T}$	β_{13} β_{13} β_{13} β_{14}	$3f\Omega_m\mathcal{H}^3(\mu_1^2k_1^2+\mu_2^2k_2^2)/(4k_1^2k_2^2)$ $-9\Omega_m^2\mathcal{H}^4(\mu_1^2k_1^2+\mu_2^2k_2^2)/(4k_1^2k_2^2)$ $-f^2\mathcal{H}^3(\mu_1^2k_1^2+\mu_2^2k_2^2)/(2k_1^2k_2^2)$ $-\mathrm{i}\;3\Omega_m\mathcal{H}^2(\mu_1k_1^3+\mu_2k_2^3)/(4k_1^2k_2^2)$	$2[1 - 2f + 2b_e - 6\mathcal{Q} - 2\mathcal{R} - (\mathcal{H}'/\mathcal{H}^2)]/\mathcal{H}$ $-2/\mathcal{H}^2$ $2(b_e - 3)/\mathcal{H}$ $2b_{10}/\mathcal{H}$
$\partial_i V\partial_\parallel\partial^i V$	β_{15}	$-\mathrm{i}\,f^2\mathcal{H}^2\boldsymbol{k}_1\cdot\boldsymbol{k}_2(\mu_1k_1+\mu_2k_2)/(2k_1^2k_2^2)$	$-4/\mathcal{H}$
$\delta_{\rm T}\partial_\parallel V$	β_{16}	$\mathrm{i}\,f\mathcal{H}(\mu_1k_2+\mu_2k_1)/(2k_1k_2)$	$2b_{10}(f + b_e - 2\mathcal{Q} - \mathcal{R}) + \mathcal{S}$
$\Phi\partial_\parallel^3 V$	β_{17}	$\mathrm{i}\;3f\Omega_m\mathcal{H}^3(\mu_1^3k_1^3+\mu_2^3k_2^3)/(4k_1^2k_2^2)$	$-2/\mathcal{H}^2$
$\partial_\parallel V\partial_\parallel^2 V$ $\partial_\parallel V\partial_\parallel^2\Psi$	β_{18} β_{18}	$-\mathrm{i}\,f^2\mathcal{H}^2(\mu_1\mu_2^2k_2+\mu_2\mu_1^2k_1)/(2k_1k_2)$ $\mathrm{i}\;3f\Omega_m\mathcal{H}^3(\mu_1\mu_2^2k_2+\mu_2\mu_1^2k_1)/(4k_1k_2)$	$2[3 - 2b_e + 4\mathcal{Q} + 2\mathcal{R} + (\mathcal{H}'/\mathcal{H}^2)]/\mathcal{H}$ $2/\mathcal{H}^2$
$\partial_\parallel V_{\rm N}^{(2)}$	β_{19}	$\mathrm{i}\,f\mathcal{H}\,\mu_3 G_2(\boldsymbol{k}_1,\boldsymbol{k}_2)/k_3$	$b_e - 2\mathcal{Q} - \mathcal{R}$

Here the $\mathcal{C}$ functions in the Fourier kernels are

$$\mathcal{C}_1 = 2f - f^2 - 3\Omega_m\;, \tag{B.1}$$

$$\mathcal{C}_2 = 2f - 1 + \big(1-f\big)\left[6\Omega_m + f\big(1-2f\big) - 2f\frac{\mathcal{H}'}{\mathcal{H}^2}\right]\;, \tag{B.2}$$

$$\mathcal{C}_3 = 2f\left(2f - 1 + \frac{\mathcal{H}'}{\mathcal{H}^2}\right) + 2\frac{f'}{\mathcal{H}}\,, \tag{B.3}$$

the $\mathcal{A}$ functions in the coefficients are

$$\begin{aligned}\mathcal{A}_1 = {}& -3 + 2f\left(2 - 2b_e + 4\mathcal{Q} + \frac{4(1-\mathcal{Q})}{\chi\mathcal{H}} + \frac{2\mathcal{H}'}{\mathcal{H}^2}\right) - \frac{2f'}{\mathcal{H}} + b_e^2 + 6b_e - 8b_e\mathcal{Q} + 4\mathcal{Q} \\ & + 16\mathcal{Q}^2 - 16\frac{\partial\mathcal{Q}}{\partial\ln L} - 8\frac{\mathcal{Q}'}{\mathcal{H}} + \frac{b_e'}{\mathcal{H}} + \frac{2}{\chi^2\mathcal{H}^2}\left(1 - \mathcal{Q} + 2\mathcal{Q}^2 - 2\frac{\partial\mathcal{Q}}{\partial\ln L}\right) \\ & - \frac{2}{\chi\mathcal{H}}\left[4 + 2b_e - 2b_e\mathcal{Q} - 4\mathcal{Q} + 8\mathcal{Q}^2 - \frac{3\mathcal{H}'}{\mathcal{H}^2}(1-\mathcal{Q}) - 8\frac{\partial\mathcal{Q}}{\partial\ln L} - 2\frac{\mathcal{Q}'}{\mathcal{H}}\right] \\ & + \frac{\mathcal{H}'}{\mathcal{H}^2}\left(-8 - 2b_e + 8\mathcal{Q} + \frac{3\mathcal{H}'}{\mathcal{H}^2}\right) - \frac{\mathcal{H}''}{\mathcal{H}^3}\,,\end{aligned} \tag{B.4}$$

$$\mathcal{A}_2 = 2\mathcal{H}\left[-\frac{15}{2} + f(3 - b_e) - \frac{3}{2}b_e - 2b_e\frac{(1-\mathcal{Q})}{\chi\mathcal{H}} + \frac{b_e'}{\mathcal{H}} + b_e^2 - 4b_e\mathcal{Q} + 12\mathcal{Q} + \frac{6(1-\mathcal{Q})}{\chi\mathcal{H}}\right. \tag{B.5}$$

$$\begin{aligned}\mathcal{A}_3 = {}& 2\mathcal{H}\left[-3 + 4b_e + \frac{2b_e(1-\mathcal{Q})}{\chi\mathcal{H}} - b_e^2 + 2b_e\mathcal{Q} - 6\mathcal{Q} - \frac{b_e'}{\mathcal{H}} - \frac{6(1-\mathcal{Q})}{\chi\mathcal{H}}\right. \\ & \left. + 2\left(1 - \frac{1}{\chi\mathcal{H}}\right)\frac{\mathcal{Q}'}{\mathcal{H}}\right]\,,\end{aligned} \tag{B.6}$$

$$\begin{aligned}\mathcal{A}_4 = {}& 4 + 2f\left[-3 + f + 2b_e - 3\mathcal{Q} - \frac{4(1-\mathcal{Q})}{\chi\mathcal{H}} - \frac{2\mathcal{H}'}{\mathcal{H}^2}\right] + \frac{2f'}{\mathcal{H}} - 6b_e - 2b_e^2 + 12b_e\mathcal{Q} - 8\mathcal{Q} \\ & - 16\mathcal{Q}^2 + 16\frac{\partial\mathcal{Q}}{\partial\ln L} + 12\frac{\mathcal{Q}'}{\mathcal{H}} - 2\frac{b_e'}{\mathcal{H}} - \frac{4}{\chi^2\mathcal{H}^2}\left(1 - \mathcal{Q} + 2\mathcal{Q}^2 - 2\frac{\partial\mathcal{Q}}{\partial\ln L}\right) \\ & - \frac{4}{\chi\mathcal{H}}\left(-1 - 2b_e + 2b_e\mathcal{Q} + \mathcal{Q} - 6\mathcal{Q}^2 + \frac{3\mathcal{H}'}{\mathcal{H}^2}(1-\mathcal{Q}) + 6\frac{\partial\mathcal{Q}}{\partial\ln L} + 2\frac{\mathcal{Q}'}{\mathcal{H}}\right) \\ & + \frac{2\mathcal{H}'}{\mathcal{H}^2}\left(3 + 2b_e - 6\mathcal{Q} - \frac{3\mathcal{H}'}{\mathcal{H}^2}\right) + \frac{2\mathcal{H}''}{\mathcal{H}^3}\,,\end{aligned} \tag{B.7}$$

$$\begin{aligned}\mathcal{A}_5 = {}& -4 - b_e + b_e^2 - 4b_e\mathcal{Q} + 6\mathcal{Q} + 4\mathcal{Q}^2 - 4\frac{\partial\mathcal{Q}}{\partial\ln L} - 4\frac{\mathcal{Q}'}{\mathcal{H}} + \frac{b_e'}{\mathcal{H}} \\ & + \frac{2}{\chi^2\mathcal{H}^2}\left(1 - \mathcal{Q} + 2\mathcal{Q}^2 - 2\frac{\partial\mathcal{Q}}{\partial\ln L}\right) \\ & + \frac{2}{\chi\mathcal{H}}\left[3 - 2b_e + 2b_e\mathcal{Q} - 3\mathcal{Q} - 4\mathcal{Q}^2 + \frac{3\mathcal{H}'}{\mathcal{H}^2}(1-\mathcal{Q}) + 4\frac{\partial\mathcal{Q}}{\partial\ln L} + 2\frac{\mathcal{Q}'}{\mathcal{H}}\right] \\ & + \frac{\mathcal{H}'}{\mathcal{H}^2}\left(3 - 2b_e + 4\mathcal{Q} + \frac{3\mathcal{H}'}{\mathcal{H}^2}\right) - \frac{\mathcal{H}''}{\mathcal{H}^3}\,,\end{aligned} \tag{B.8}$$

and the functions $\mathcal{R}, \mathcal{S}$ in the coefficients are

$$\mathcal{R} = \frac{2(1-\mathcal{Q})}{\chi\mathcal{H}} + \frac{\mathcal{H}'}{\mathcal{H}^2} \,, \tag{B.9}$$

$$\mathcal{S} = 4\left(2 - \frac{1}{\chi\mathcal{H}}\right)\frac{\partial b_{10}}{\partial \ln L} \,. \tag{B.10}$$

The magnification bias is defined by Alonso et al. (2015); Di Dio et al. (2016); Maartens et al. (2020):

$$\mathcal{Q} = -\frac{\partial \ln \bar{n}_g}{\partial \ln L}\bigg|_{\rm c} \,, \tag{B.11}$$

where L is the background luminosity and the derivative is evaluated at the flux cut. Similarly, $\partial b_{10}/\partial \ln L$ is understood to be evaluated at the flux cut. We use a short-hand notation for the second luminosity derivative of $\bar{n}_g$:

$$\frac{\partial \mathcal{Q}}{\partial \ln L} \equiv -\frac{\partial^2 \ln \bar{n}_g}{\partial (\ln L)^2}\bigg|_{\rm c} \,. \tag{B.12}$$

C. Upsilon coefficients

Υ_I functions in (8.74)

$$\frac{1}{f_{\rm NL}}\frac{\Upsilon_1}{\mathcal{H}^2} = 2(3-b_e)f + 3\Omega_m\left[1+b_e-4\mathcal{Q}-\frac{2(1-\mathcal{Q})}{\chi\mathcal{H}}-\frac{\mathcal{H}'}{\mathcal{H}^2}\right] + \frac{6\Omega_m}{\big(3\Omega_m+2f\big)}\left[\frac{f'}{\mathcal{H}}+\left(1+2\frac{\mathcal{H}'}{\mathcal{H}^2}\right)f\right] \tag{C.1}$$

$$\frac{1}{f_{\rm NL}}\frac{\Upsilon_2}{\mathcal{H}} = 2f\left[b_e-2\mathcal{Q}-\frac{2(1-\mathcal{Q})}{\chi\mathcal{H}}-\frac{\mathcal{H}'}{\mathcal{H}^2}\right] \tag{C.2}$$

$$\frac{1}{b_{01}}\frac{\Upsilon_3}{\mathcal{H}^2} = \frac{3}{2}\Omega_m\left[2+b_e-4\mathcal{Q}+\frac{2(1-\mathcal{Q})}{\chi\mathcal{H}}+\frac{\mathcal{H}'}{\mathcal{H}^2}+2\left(2-\frac{1}{\chi\mathcal{H}}\right)\frac{\partial\ln b_{01}}{\partial\ln L}\right] + f\left[3-f-b_e+\frac{1}{2}\frac{\partial\ln b_{01}}{\partial\ln a}\right] \tag{C.3}$$

$$\frac{1}{b_{01}}\frac{\Upsilon_4}{\mathcal{H}} = -\frac{3}{2}\Omega_m \tag{C.4}$$

$$\frac{1}{b_{01}}\frac{\Upsilon_5}{\mathcal{H}} = f\left[f+b_e-2\mathcal{Q}-\frac{2(1-\mathcal{Q})}{\chi\mathcal{H}}-\frac{\mathcal{H}'}{\mathcal{H}^2}+2\left(2-\frac{1}{\chi\mathcal{H}}\right)\frac{\partial\ln b_{01}}{\partial\ln L}\right] \tag{C.5}$$

Note that $\Upsilon_2 = 2f_{\rm NL}\,\gamma_1$.

Table C.1.: The $f_{\rm NL}\neq 0$ terms from relativistic projection effects [see (8.74)].

TERM	Υ	FOURIER KERNEL	COEFFICIENT
$V^{(2)}_{\rm nG}$	Υ_1	$2f_{\rm NL}\,\mathcal{H}f\mathcal{M}_3/(\mathcal{M}_1\mathcal{M}_2k_3^2)$	$(3-b_e)\mathcal{H}$
$\Psi^{(2)}_{\rm nG}=\Phi^{(2)}_{\rm nG}$	Υ_1	$-3f_{\rm NL}\Omega_m\mathcal{H}^2\mathcal{M}_3/(\mathcal{M}_1\mathcal{M}_2k_3^2)$	$4\mathcal{Q}-1-b_e+\mathcal{R}$

$\Psi^{(2)\prime}_{\rm nG}$	Υ_1	$6f_{\rm NL}\left[f' + (\mathcal{H} + 2\mathcal{H}'/\mathcal{H})f\right]\Omega_m\mathcal{H}^2\mathcal{M}_3/\left[(3\Omega_m + 2f)(\mathcal{M}_1\mathcal{M}_2k_3^2)\right]$	$1/\mathcal{H}$
$\partial_\parallel V^{(2)}_{\rm nG}$	Υ_2	$\mathrm{i}\ 2f_{\rm NL}\,\mathcal{H}f\,\mu_3\mathcal{M}_3/(\mathcal{M}_1\mathcal{M}_2k_3)$	$b_e - 2Q - \mathcal{R}$
$\Psi\varphi_{\rm p}$	Υ_3	$-3\Omega_m\mathcal{H}^2\left[(k_1^2/\mathcal{M}_1) + (k_2^2/\mathcal{M}_2)\right]/(4k_1^2k_2^2)$	$b_{01}\left[8\mathcal{Q} + 2\mathcal{R} - 2b_e - 4 - \mathcal{S}/(b_{10} - 1)\right]$
$V\varphi_{\rm p}$	Υ_3	$f\mathcal{H}\left[(k_1^2/\mathcal{M}_1) + (k_2^2/\mathcal{M}_2)\right]/(2k_1^2k_2^2)$	$b_{01}\left[2(3 - b_e - f)\mathcal{H} + b'_{10}/(b_{10} - 1)\right]$
$\Psi\partial_\parallel\varphi_{\rm p}$	Υ_4	$-\mathrm{i}\,3\Omega_m\mathcal{H}^2\left[(\mu_1k_1^3/\mathcal{M}_1) + (\mu_2k_2^3/\mathcal{M}_2)\right]/(4k_1^2k_2^2)$	$2b_{01}/\mathcal{H}$
$\varphi_{\rm p}\partial_\parallel V$	Υ_5	$\mathrm{i}\ f\mathcal{H}\left[(\mu_1k_2/\mathcal{M}_2) + (\mu_2k_1/\mathcal{M}_1)\right]/(2k_1k_2)$	$b_{01}\left[2f + 2b_e - 4\mathcal{Q} - 2\mathcal{R} + \mathcal{S}/(b_{10} - 1)\right]$

D. Derivation of sum formula

Here we present a detailed derivation of the analytic result of the integration of

$$X_{\ell m}^{ab} = \int_0^{2\pi} \mathrm{d}\varphi \int_{-1}^{1} \mathrm{d}\mu_1 \, (\mathrm{i}\,\mu_1)^a (\mathrm{i}\,\mu_2)^b \, Y_{\ell m}^*(\mu_1, \varphi) \, . \tag{D.1}$$

In the above, we have used that $\mu_1 = \cos\theta$, such that $Y_{\ell m}(\theta, \varphi) = Y_{\ell, m}(\mu_1, \varphi)$. The standard orthonormal spherical harmonics are defined as,

$$Y_{\ell m}(\mu_1, \varphi) = \sqrt{\frac{2\ell+1}{4\pi}} \sqrt{\frac{(\ell-m)!}{(\ell+m)!}} P_{\ell m}(\mu_1) e^{\mathrm{i}\, m\varphi} \, , \tag{D.2}$$

and the spherical harmonics are related to their complex conjugate as,

$$Y_{\ell, -m} = (-1)^m Y_{\ell, m}^* \, , \quad Y_{\ell, m}^* = (-1)^m Y_{\ell, -m} \, . \tag{D.3}$$

Equation (D.1) is separable. We can make this explicit as follows. First expressing μ_2 in terms of μ_1 using $\mu_2 = \sqrt{1-\mu_1^2} \sin\theta \sin\varphi + \mu_1 \cos\theta$, where $\theta \equiv \theta_{12} \neq \theta_1$– it is the angle between vectors $\boldsymbol{k}_1$ and $\boldsymbol{k}_2$. Then we can expand $(\mathrm{i}\,\mu_2)^b$ using the binomial series,

$$\begin{aligned}
(\mathrm{i}\,\mu_2)^b &= \mathrm{i}^{\,b} (\sqrt{1-\mu_1^2} \sin\theta \sin\varphi + \mu_1 \cos\theta)^b \\
&= \mathrm{i}^{\,b} \sum_{g=0}^{b} \binom{b}{g} \left[\sqrt{1-\mu_1^2} \sin\theta \sin\varphi \right]^g [\mu_1 \cos\theta]^{b-g} \\
&= \mathrm{i}^{\,b} \sum_{g=0}^{b} \binom{b}{g} (1-\mu_1^2)^{g/2} \mu_1^{b-g} \sin^g\varphi \sin^g\theta \cos^{b-g}\theta \, .
\end{aligned} \tag{D.4}$$

Using this, we have,

$$X_{\ell m}^{ab} = \mathrm{i}^{\,a+b} \sum_{g=0}^{b} \sin^g\theta \cos^{b-g}\theta \binom{b}{g} \int_0^{2\pi} \mathrm{d}\varphi \int_{-1}^{1} \mathrm{d}\mu (1-\mu^2)^{g/2} \mu^{a+b-g} \times$$

$$\sin^g \varphi Y^*_{\ell m}(\mu, \varphi)\,, \tag{D.5}$$

where we have dropped subscript on $\mu_1 \equiv \mu$ for brevity. Now using the definition of the complex-conjugated standard spherical harmonics,

$$\begin{aligned} Y^*_{\ell m} &= (-1)^m Y_{\ell,-m} \\ &= (-1)^m \sqrt{\frac{2\ell+1}{4\pi}} \sqrt{\frac{(\ell+m)!}{(\ell-m)!}} P_{\ell,-m}(\mu) e^{-\mathrm{i} m\varphi} \end{aligned} \tag{D.6}$$

and the associated Legendre polynomials $P_{\ell m}$ can be rewritten for negative m as,

$$P_{\ell,-m} = (-1)^m \frac{(\ell-m)!}{(\ell+m)!} P_{\ell,m}\,, \tag{D.7}$$

such that,

$$Y^*_{\ell m} = \sqrt{\frac{2\ell+1}{4\pi}} \sqrt{\frac{(\ell-m)!}{(\ell+m)!}} P_{\ell m}(\mu) e^{-\mathrm{i} m\varphi}\,. \tag{D.8}$$

This makes the separability of the integral (D.1) explicit,

$$\begin{aligned} X^{ab}_{\ell m} =& \mathrm{i}^{\,a+b} \sum_{g=0}^{b} \binom{b}{g} \sin^g \theta \cos^{b-g} \theta \sqrt{\frac{2\ell+1}{4\pi}} \sqrt{\frac{(\ell-m)!}{(\ell+m)!}} \int_0^{2\pi} \mathrm{d}\varphi \, \sin^g \varphi e^{-\mathrm{i} m\varphi} \times \\ & \int_{-1}^{1} \mathrm{d}\mu \, (1-\mu^2)^{g/2} \mu^{a+b-g} P_{\ell m}(\mu)\,. \end{aligned} \tag{D.9}$$

Now these two integrals can be solved independently. Starting with the integral over μ, splitting the interval $\int_{-1}^{1} = \int_{-1}^{0} + \int_{0}^{1}$, the $\int_{-1}^{1}$ term can be rewritten using a change of variables and the parity of the associated Legendre polynomials as,

$$\begin{aligned} & \int_{-1}^{0} \mathrm{d}\mu \, (1-\mu^2)^{g/2} \mu^{a+b-g} P_{\ell m}(\mu) \\ &= -\int_{0}^{-1} \mathrm{d}\mu \, (1-\mu^2)^{g/2} \mu^{a+b-g} P_{\ell m}(\mu) \\ &= \int_{0}^{1} \mathrm{d}\tilde{\mu} \, (1-\tilde{\mu}^2)^{g/2} (-\tilde{\mu})^{a+b-g} P_{\ell m}(-\tilde{\mu}) \\ &= (-1)^{\ell+m+a+b-g} \int_{0}^{1} \mathrm{d}\mu \, (1-\mu)^{g/2} \mu^{a+b-g} P_{\ell m}(\mu)\,, \end{aligned} \tag{D.10}$$

where we have used that $P_{\ell m}(-x) = (-1)^{\ell+m} P_{\ell m}(x)$, and renamed $\tilde{\mu} = \mu$ in the last line. The full integral over μ then can be written as,

$$\left[1 + (-1)^{\ell+m+a+b-g}\right] \int_0^1 \mathrm{d}\mu \, (1-\mu^2)^{g/2} \mu^{a+b-g} P_{\ell m}(\mu) \, . \tag{D.11}$$

The associated Legendre polynomials can be written in closed form, using,

$$\begin{aligned} P_{\ell m}(\mu) &= (-1)^m P_\ell^m \\ &= (-1)^m (-1)^m 2^\ell (1-\mu^2)^{m/2} \sum_{k=m}^{\ell} \frac{k!}{(k-m)!} \mu^{k-m} \binom{\ell}{k} \binom{\frac{1}{2}(\ell+k-1)}{\ell} \\ & 2^\ell (1-\mu^2)^{m/2} \sum_{k=m}^{\ell} \frac{k!}{(k-m)!} \mu^{k-m} \binom{\ell}{k} \binom{\frac{1}{2}(\ell+k-1)}{\ell} \, , \end{aligned} \tag{D.12}$$

such that,

$$\begin{aligned} & \left[1 + (-1)^{\ell+m+a+b-g}\right] (-1)^m 2^\ell \sum_{k=m}^{\ell} \frac{k!}{(k-m)!} \binom{\ell}{k} \binom{\frac{1}{2}(\ell+k-1)}{\ell} \times \\ & \int_0^1 \mathrm{d}\mu \, (1-\mu^2)^{\frac{1}{2}(m+g)} \mu^{a+b+k-g-m} \, . \end{aligned} \tag{D.13}$$

Changing variables $\xi = \mu^2$, omitting the prefactor for brevity, we get,

$$\int_0^1 \mathrm{d}\xi \, \frac{1}{2} (1-\xi)^{\frac{1}{2}(m+g)} \xi^{\frac{1}{2}(a+b+k-g-m-1)} \, . \tag{D.14}$$

Comparing to the Beta function,

$$B(x,y) = \int_0^1 \mathrm{d}t \, (1-t)^{y-1} t^{x-1} \, , \tag{D.15}$$

we can identify $x = \frac{1}{2}(a+b+k-g-m+1)$ and $y = \frac{1}{2}(m+g+2)$. The Beta function can be expressed in terms of Gamma functions $B(x,y) = \frac{\Gamma(x)\Gamma(y)}{\Gamma(x+y)}$, which in turn can be written in terms of factorials, for any positive integer n this relation is $\Gamma(n) = (n-1)!$. We will express the result in terms of Gamma functions as,

$$\begin{aligned} & \int_{-1}^1 \mathrm{d}\mu \, (1-\mu^2)^{g/2} \mu^{a+b-g} P_{\ell m}(\mu) \\ & = \left[1 + (-1)^{\ell+m+a+b-g}\right] (-1)^m 2^\ell \sum_{k=m}^{\ell} \frac{k!}{(k-m)!} \binom{\ell}{k} \binom{\frac{1}{2}(\ell+k-1)}{\ell} \times \end{aligned}$$

$$\left\{\Gamma\left[\frac{1}{2}(m+g+2)\right]\Gamma\left[\frac{1}{2}(a+b+k-g-m+1)\right]\right\}\cdot\left\{\Gamma\left[\frac{1}{2}(a+b+k+3)\right]\right\}^{-1}. \tag{D.16}$$

Now to solve the integral over φ,

$$\int_0^{2\pi} \mathrm{d}\varphi \, \sin^g \varphi e^{-\mathrm{i}\, m\varphi} . \tag{D.17}$$

Write $\sin^g \varphi$ in terms of e using the usual trig identities and binomial expansion as,

$$\sin^g \varphi = \frac{1}{(2\mathrm{i}\,)^g}\sum_{n=0}^{g}\binom{g}{n} e^{\mathrm{i}\,(g-n)\varphi}(-1)^n e^{-\mathrm{i}\, n\varphi} \tag{D.18}$$

to get,

$$\begin{aligned}
&\int_0^{2\pi} \mathrm{d}\varphi \, \frac{1}{(2\mathrm{i}\,)^g}\sum_{n=0}^{g}\binom{g}{n}(-1)^n e^{\mathrm{i}\,\varphi(g-m-2n)} \\
&= \frac{1}{(2\mathrm{i}\,)^g}\sum_{n=0}^{g}\binom{g}{n}(-1)^n \int_0^{2\pi} \mathrm{d}\varphi \, e^{\mathrm{i}\,\varphi(g-m-2n)} \\
&= \frac{1}{(2\mathrm{i}\,)^g}\sum_{n=0}^{g}\binom{g}{n}(-1)^n (2\pi)\delta_{g-m-2n,0} .
\end{aligned} \tag{D.19}$$

The Kronecker δ picks out the term in the sum which satisfies $g-m-2n=0 \Rightarrow n=\frac{1}{2}(g-m)$, s.t.

$$\int_0^{2\pi} \mathrm{d}\varphi \, \sin^g \varphi e^{-\mathrm{i}\, m\varphi} = \frac{1}{(2\mathrm{i}\,)^g}\binom{g}{\frac{1}{2}(g-m)}(2\pi)(-1)^{\frac{1}{2}(g-m)} \tag{D.20}$$

where n must be a positive integer (or zero), so $g \geq m$ and $g-m$ even.

E. Presentation of kernel coefficients

Here we present the higher order $\mathcal{H}/k$ kernels for the first of the cyclic permutations. It is worth noting that these cannot be exacly manipulated to obtain the coefficients for the other two cyclic permutations, since making the replacements $\mu_1 \to \mu_2,\, \mu_3$ introduces additional powers of μ_i, giving rise to slightly different coefficients $\mathcal{K}_{ab}$. It is however easy enough to extract the coefficients for these permutations following the same method. Below we focus on only the first of the cyclic permutations, that is, the 123 permutation, as outlined before. Schematic representations of the higher order Newtonian and GR kernels are given, along with their corresponding coefficients. Like before, for brevity we use shorthand notations; $F = F_2(\boldsymbol{k}_1, \boldsymbol{k}_2)$, $G = G_2(\boldsymbol{k}_1, \boldsymbol{k}_2)$, and $S = S_2(\boldsymbol{k}_1, \boldsymbol{k}_2)$. Superscript n on $\mathcal{K}^{(n)}_{ab}$ denotes the power $(\mathcal{H}/k)^n$.

$$\mathcal{K}^{(2)}_{ab} = \begin{pmatrix} \bullet & \circ & \bullet & \circ & \bullet & \circ \\ \circ & \bullet & \circ & \bullet & \circ & \bullet \\ \bullet & \circ & \bullet & \circ & \bullet & \circ \\ \circ & \bullet & \circ & \bullet & \circ & \circ \\ \bullet & \circ & \bullet & \circ & \circ & \circ \\ \circ & \bullet & \circ & \circ & \circ & \circ \end{pmatrix}, \tag{E.1}$$

with coefficients,

$$\begin{aligned}
\mathcal{K}^{(2)}_{00} =& b_1 b_{s^2} S \gamma_2 \left(\frac{1}{k_1^2} + \frac{1}{k_2^2}\right) + b_1^2 \left\{ \left[\gamma_2 \left(1+F\right) + \beta_{12}\right] \left[\frac{1}{k_1^2} + \frac{1}{k_2^2}\right] + \frac{\mu \beta_{11}}{k_1 k_2} + \frac{F\beta_6 + G\beta_7}{k_3^2} \right\} \\
\mathcal{K}^{(2)}_{02} =& = \frac{f b_{s^2} S \gamma_2}{k_1^2} - b_1 f \left[\frac{\gamma_2 \left(1+F\right) + \beta_{12}}{k_1^2} + \frac{G\gamma_2 k_2^2}{k_1^2 k_3^2} + \frac{\beta_{11}\mu}{k_1 k_2} + \frac{\beta_{12}}{k_2^2} + \frac{F\beta_6 + G(\beta_7 + \gamma_2)}{k_3^2} \right] \\
& + b_1 \gamma_1 \left[\frac{\beta_{14}}{k_1^2} + \frac{\mu \beta_{15}}{k_1 k_2} + \frac{\beta_{16}}{k_2^2} - \frac{G\beta_{19}}{k_3^2} \right] - b_1^2 \left[\frac{(\beta_9 + E\beta_{10} + \beta_{13})}{k_1^2} + f\gamma_2 \left(\frac{1}{k_1^2} + \frac{1}{k_2^2}\right) \right]
\end{aligned}$$

$$\begin{aligned}
\mathcal{K}_{04}^{(2)} =& f^2\gamma_2\left[\frac{b_1}{k_1^2}+\frac{Gk_2^2}{k_1^2k_3^2}\right]+\frac{b_1}{k_1^2}\left[f\left(\beta_9+E\beta_{10}+\beta_{13}\right)-\beta_{17}\gamma_1\right]\\
\mathcal{K}_{11}^{(2)} =& \frac{b_{s^2}S\gamma_1^2}{k_1k_2}+b_1\left[\beta_{15}\gamma_1\mu\left(\frac{1}{k_1^2}+\frac{1}{k_2^2}\right)+\beta_{14}\gamma_1\left(\frac{k_1}{k_2^3}+\frac{k_2}{k_1^3}\right)+\frac{2\beta_{16}\gamma_1+\gamma_1^2\left(1+F\right)}{k_1k_2}\right.\\
&\left.-\frac{G\left(k_1^2+k_2^2\right)\left(\beta_{19}\gamma_1+2f\gamma_2\right)}{k_1k_2k_3^2}\right]\\
\mathcal{K}_{13}^{(2)} =& f\gamma_1\left[-\frac{k_2\beta_{14}}{k_1^3}-\frac{\beta_{15}\mu}{k_1^2}-\frac{\beta_{16}}{k_1k_2}+Gk_2\frac{\left(\beta_{19}-\gamma_1\right)}{k_1k_3^2}\right]+b_1\left[-\gamma_1\left(\frac{k_2\beta_{17}}{k_1^3}+\frac{\beta_{18}}{k_1k_2}\right)\right.\\
&\left.+\frac{f}{k_1k_2}\left(\beta_8+2\beta_9+2E\beta_{10}-\gamma_1^2\right)+2f^2\gamma_2\left(\frac{1}{k_1k_2}+\frac{k_2}{k_1^3}\right)\right]\\
\mathcal{K}_{15}^{(2)} =& \frac{fk_2}{k_1^3}\left[\gamma_1\beta_{17}-\gamma_2\right]\\
\mathcal{K}_{20}^{(2)} =& -\frac{fb_{s^2}S\gamma_2}{k_2^2}+b_1\left[\frac{\beta_{16}\gamma_1-f\beta_{12}}{k_1^2}+\frac{\beta_{14}\gamma_1-f\left[\beta_{12}+\gamma_2\left(1+F\right)\right]}{k_2^2}+\mu\frac{\left(-f\beta_{11}+\gamma_1\beta_{15}\right)}{k_1k_2}\right.\\
&\left.-f\frac{F\beta_6+G\left(\beta_7+\gamma_2\right)}{k_3^2}-\frac{fGk_1^2\gamma_2}{k_2^2k_3^2}\right]-b_1^2\left[\frac{\beta_9+E\beta_{10}+\beta_{13}}{k_2^2}+f\gamma_2\left(\frac{1}{k_1^2}+\frac{1}{k_2^2}\right)\right]\\
\mathcal{K}_{22}^{(2)} =& f\gamma_1\left[-\left(\beta_{14}+\beta_{16}\right)\left(\frac{1}{k_1^2}+\frac{1}{k_2^2}\right)-\frac{2\beta_{15}\mu}{k_1k_2}+\frac{2G\left(\beta_{19}-\gamma_1\right)}{k_3^2}\right]+f^2\left[\beta_{12}\left(\frac{1}{k_1^2}+\frac{1}{k_2^2}\right)\right.\\
&\left.+\frac{\beta_{11}\mu}{k_1k_2}+\frac{F\beta_6+G\left(\beta_7+2\gamma_2\right)}{k_3^2}\right]+b_1\left[\left(3f^2\gamma_2-\beta_{18}\gamma_1\right)\left(\frac{1}{k_1^2}+\frac{1}{k_2^2}\right)\right.\\
&\left.+f\frac{\left(k_1^2+k_2^2\right)\left(\beta_9+E\beta_{10}+\beta_{13}-\gamma_1^2\right)}{k_1^2+k_2^2}\right]\\
\mathcal{K}_{24}^{(2)} =& \frac{f}{k_1^2}\left[\gamma_1\left(\beta_{17}+\beta_{18}\right)+f\left(-\beta_9-E\beta_{10}-\beta_{13}+\gamma_1^2\right)-2f^2\gamma_2\right]\\
\mathcal{K}_{31}^{(2)} =& -f\gamma_1\left[\frac{k_1\beta_{14}}{k_2^3}+\frac{\beta_{15}\mu}{k_2^2}+\frac{\beta_{16}}{k_1k_2}-\frac{Gk_1\beta_{19}}{k_2k_3^2}\right]+\left[-f\gamma_1^2+2f^2\gamma_2\right]\frac{Gk_1}{k_2k_3^2}\\
&+b_1\left[\frac{k_1}{k_2^3}\left(-\beta_{17}\gamma_1+2f^2\gamma_2\right)+f\frac{\beta_8+2\beta_9+2E\beta_{10}-\gamma_1^2}{k_1k_2}-\frac{\beta_{18}\gamma_1^2-2f^2\gamma_2}{k_1k_2}\right]\\
\mathcal{K}_{33}^{(2)} =& \frac{f}{k_1k_2}\left[2\beta_{18}\gamma_1+f\left(-\beta_8-2\beta_9-2E\beta_{10}+2\gamma_1^2\right)-2f^2\gamma_2\right]\\
\mathcal{K}_{40}^{(2)} =& f^2\gamma_2\frac{Gk_1^2}{k_2^2k_3^2}-b_1\gamma_1\frac{\beta_{17}}{k_2^2}+b_1f\left[\frac{\beta_9+E\beta_{10}+\beta_{13}}{k_2^2}\right]+b_1f^2\frac{\gamma_2}{k_2^2}\\
\mathcal{K}_{42}^{(2)} =& f\gamma_1\frac{\left(\beta_{17}+\beta_{18}\right)}{k_2^2}+\frac{f^2}{k_2^2}\left[-\beta_9-E\beta_{10}\beta_{13}+\gamma_1^2\right]-f^3\frac{2\gamma_2}{k_2^2}\\
\mathcal{K}_{51}^{(2)} =& f\frac{k_1}{k_2^3}\left[\beta_{17}\gamma_1-f^2\gamma_2\right].
\end{aligned}$$

$$\mathcal{K}^{(3)}_{ab} = \begin{pmatrix} \circ & \bullet & \circ & \bullet & \circ & \bullet \\ \bullet & \circ & \bullet & \circ & \bullet & \circ \\ \circ & \bullet & \circ & \bullet & \circ & \circ \\ \bullet & \circ & \bullet & \circ & \circ & \circ \\ \circ & \bullet & \circ & \circ & \circ & \circ \\ \bullet & \circ & \circ & \circ & \circ & \circ \end{pmatrix}, \tag{E.2}$$

with coefficients,

$$\begin{aligned}
\mathcal{K}^{(3)}_{01} =& \gamma_1\gamma_2\frac{b_{s^2}S}{k_1^2k_2} + b_1\gamma_1\left[\frac{\beta_{12}\left(k_1^2+k_2^2\right)}{k_1^2k_2^3} + \frac{\beta_{11}\mu}{k_1k_2^2} + \frac{F\beta_6+G\beta_7}{k_2k_3^2}\right] + b_1\gamma_2\,\Bigg[\frac{\beta_{14}+\beta_{16}}{k_1^2k_2} \\
&+\frac{\beta_{15}\mu}{k_1k_2^2} + \frac{(k_2\beta_{14}+k_1\beta_{15}\mu)}{k_1^4} + \frac{\beta_{16}}{k_2^3} - G\beta_{19}\left(\frac{1}{k_2k_3^2}+\frac{k_2}{k_1^2k_3^2}\right)\Bigg] + b_1\gamma_1\gamma_2\frac{(1+F)}{k_1^2k_2} - b_1^2\frac{(\beta_4-\beta}{k_1} \\
\mathcal{K}^{(3)}_{03} =& -\frac{f\gamma_2}{k_1^2}\left[\frac{k_2\beta_{14}}{k_1^2}+\frac{\beta_{15}\mu}{k_1}+\frac{\beta_{16}}{k_2}\right] + f\gamma_2Gk_2\frac{[\beta_{19}-\gamma_1]}{k_1^2k_3^2} - b_1\,\Bigg[\frac{k_2\beta_{17}\gamma_2}{k_1^4} + [\gamma_2\beta_{17} - f\,(\beta_4-\beta_3+ \\
&+\gamma_1\left(\beta_9+E\beta_{10}+\beta_{13}\right) + f\gamma_1\gamma_2]\,\frac{1}{k_1^2k_2}\Bigg] \\
\mathcal{K}^{(3)}_{05} =& f\gamma_2\frac{k_2\beta_{17}}{k_1^4} \\
\mathcal{K}^{(3)}_{10} =& \gamma_1\gamma_2\frac{b_{s^2}S}{k_1k_2^2} + b_1\gamma_1\left[\frac{\left(k_1^2+k_2^2\right)\beta_{12}}{k_1^3k_2^2}+\frac{F\beta_6+G\beta_7}{k_1k_3^2}+\frac{\beta_{11}\mu}{k_1^2k_2}\right] + b_1\gamma_2\,\Bigg[\frac{\left(k_1^2+k_2^2\right)\beta_{16}}{k_1^3k_2^2} \\
&+\frac{\left(k_1^2+k_2^2\right)(k_1\beta_{14}+k_2\beta_{15}\mu)}{k_1^2k_2^4} - G\beta_{19}\frac{\left(k_1^2+k_2^2\right)}{k_1k_2^2k_3^2}\Bigg] + b_1\gamma_1\gamma_2\frac{[1+F]}{k_1k_2^2} - b_1^2\frac{[\beta_4-\beta_3+E\beta_5]}{k_1k_2^2} \\
\mathcal{K}^{(3)}_{12} =& \gamma_1^2\left[\frac{\beta_{14}}{k_1^3}+\frac{\beta_{15}\mu}{k_1^2k_2}+\frac{\beta_{16}}{k_1k_2^2}-G\frac{\beta_{19}}{k_1k_3^2}\right] + f\,\Bigg[-\gamma_1\frac{\left(k_1^2+k_2^2\right)\beta_{12}}{k_1^3k_2^2} - \gamma_1\,\Bigg(\frac{F\beta_6+G\,[\beta_7+3\gamma_2]}{k_1k_3^2} - \frac{\beta_{11}}{k_1^2} \\
&+\gamma_2\left(-\frac{\beta_{14}}{k_1k_2^2}-\frac{\beta_{15}\mu}{k_1^2k_2}-\frac{\beta_{16}}{k_1^3}+3\frac{G\gamma_2}{k_1k_3^2}\right)\Bigg] - b_1\,\Bigg[\frac{\beta_{13}\gamma_1}{k_1^3} + \frac{-f\left(\beta_4-\beta_3+E\beta_5\right)+\beta_8\gamma_1}{k_1k_2^2} \\
&+\frac{\gamma_1\left(2k_1^2+k_2^2\right)}{k_1^3k_2^2}\left(\beta_9+E\beta_{10}+f\gamma_2\right) + \frac{\left(k_1^2+k_2^2\right)\beta_{18}\gamma_2}{k_1^3k_2^2}\Bigg] \\
\mathcal{K}^{(3)}_{14} =& \gamma_1\frac{-\beta_{17}\gamma_1+f^2\gamma_2}{k_1^3} + f\gamma_1\frac{[\beta_9+E\beta_{10}+\beta_{13}]}{k_1^3} + f\gamma_2\frac{\beta_{18}}{k_1^3} \\
\mathcal{K}^{(3)}_{21} =& \gamma_1^2\left[\frac{\beta_{14}}{k_2^3}+\frac{\beta_{15}\mu}{k_1k_2^2}+\frac{\beta_{16}}{k_1^2k_2}-\frac{G\beta_{19}}{k_2k_3^2}\right] + f\,\Bigg[-\frac{\left(k_1^2+k_2^2\right)\beta_{12}\gamma_1}{k_1^2k_2^3} - \gamma_1\frac{F\beta_6}{k_2k_3^2} + G\gamma_1\frac{-\beta_7-3\gamma_2}{k_2k_3^2} \\
&+G\gamma_2\frac{\beta_{19}}{k_2k_3^2} - \frac{\mu}{k_1k_2^2}\left(\gamma_1\beta_{11}+\gamma_2\beta_{15}\right) - \gamma_2\left(\frac{\beta_{14}}{k_1^2k_2}+\frac{\beta_{16}}{k_2^3}\right)\Bigg] + b_1\,\Bigg[f\frac{\left(\beta_4-\beta_3+E\beta_5\right)}{k_1^2k_2} - \gamma_2\frac{(k_1^2}{} \\
&-\gamma_1\gamma_2f\left(\frac{1}{k_2^3}+\frac{2}{k_1^2k_2}\right) - \gamma_1E\frac{\left(k_1^2+2k_2^2\right)\beta_{10}}{k_1^2k_2^3} - \gamma_1\frac{\left(k_1^2+2k_2^2\right)\beta_9}{k_1^2k_2^3} - \gamma_1\left(\frac{\beta_8}{k_1^2k_2}+\frac{\beta_{13}}{k_2^3}\right)\Bigg]
\end{aligned}$$

$$
\begin{aligned}
\mathcal{K}_{23}^{(3)} =& -\gamma_1^2\frac{\beta_{18}}{k_1^2k_2} + f\gamma_1\frac{[\beta_8+3\beta_9+3E\beta_{10}+\beta_{13}]}{k_1^2k_2} + f\gamma_2\frac{[\beta_{17}+\beta_{18}]}{k_1k_2^2} + f^2\frac{[-\beta_4+\beta_3-E\beta_5+3\gamma_1\gamma_2 \ldots}{k_1^2k_2} \\
\mathcal{K}_{30}^{(3)} =& -f\gamma_2\left[\frac{k_1\beta_{14}}{k_2^4}+\frac{\beta_{15}\mu}{k_2^3}+\frac{\beta_{16}}{k_1k_2^2}\right] + f\gamma_2 G\frac{k_1\left(\beta_{19}-\gamma_1\right)}{k_2^2k_3^2} - b_1\gamma_1\left[\frac{\beta_9+E\beta_{10}+\beta_{13}}{k_1k_2^2}\right] \\
& - b_1\gamma_2\frac{\left(k_1^2+k_2^2\right)\beta_{17}}{k_1k_2^4} + b_1 f\frac{\left(\beta_4-\beta_3+E\beta_5-\gamma_1\gamma_2\right)}{k_1k_2^2} \\
\mathcal{K}_{32}^{(3)} =& -\gamma_1^2\frac{\beta_{18}}{k_1k_2^2} + f\gamma_1\frac{\left(\beta_8+3\beta_9+3E\beta_{10}+\beta_{13}\right)}{k_1k_2^2} + f\gamma_2\frac{\left(\beta_{17}+\beta_{18}\right)}{k_1k_2^2} - f^2\frac{(\beta_4-\beta_3+E\beta_5-3\gamma_1\gamma_2 \ldots}{k_1k_2^2} \\
\mathcal{K}_{41}^{(3)} =& -\gamma_1^2\frac{\beta_{17}}{k_2^3} + f^2\frac{\gamma_1\gamma_2}{k_2^3} + f\gamma_1\frac{\left(\beta_9+E\beta_{10}+\beta_{13}\right)}{k_2^3} + f\gamma_2\frac{\beta_{18}}{k_2^3} \\
\mathcal{K}_{50}^{(3)} =& f\gamma_2\frac{k_1\beta_{17}}{k_2^4}.
\end{aligned}
$$

$$
\mathcal{K}_{ab}^{(4)} = \begin{pmatrix}
\bullet & \circ & \bullet & \circ & \bullet & \circ \\
\circ & \bullet & \circ & \bullet & \circ & \circ \\
\bullet & \circ & \bullet & \circ & \circ & \circ \\
\circ & \bullet & \circ & \circ & \circ & \circ \\
\bullet & \circ & \circ & \circ & \circ & \circ \\
\circ & \circ & \circ & \circ & \circ & \circ
\end{pmatrix}, \tag{E.3}
$$

with coefficients,

$$
\begin{aligned}
\mathcal{K}_{00}^{(4)} =& \gamma_2^2\frac{b_{s^2}S}{k_1^2k_2^2} + b_1\gamma_2\left[F\frac{\left(k_1^2+k_2^2\right)\beta_6}{k_1^2k_2^2k_3^2} + G\frac{\left(k_1^2+k_2^2\right)\beta_7}{k_1^2k_2^2k_3^2} + \frac{\left(k_1^2+k_2^2\right)\beta_{11}\mu}{k_1^3k_2^3} + \frac{\left(k_1^2+k_2^2\right)^2\beta_{12}}{k_1^4k_2^4}\right] \\
& + b_1\gamma_2^2\frac{(1+F)}{k_1^2k_2^2} + b_1^2\frac{\left(\beta_1+E\beta_2\right)}{k_1^2k_2^2} \\
\mathcal{K}_{02}^{(4)} =& \gamma_1\gamma_2\left[\frac{\beta_{14}}{k_1^4}+\frac{\beta_{15}\mu}{k_1^3k_2}+\frac{\beta_{16}}{k_1^2k_2^2}-G\frac{\beta_{19}}{k_1^2k_2^2}\right] - f\gamma_2\left[F\frac{\beta_6}{k_1^2k_3^2}+G\frac{\beta_7}{k_1^2k_3^2}+\frac{\beta_{11}\mu}{k_1^3k_2}+\frac{\left(k_1^2+k_2^2\right)\beta_{12}}{k_1^4k_2^2}\right] \\
& - b_1 f\frac{\left(\beta_1+E\beta_2+\gamma_2^2\right)}{k_1^2k_2^2} - b_1\gamma_1\frac{\left(\beta_4-\beta_3+E\beta_5\right)}{k_1^2k_2^2} - b_1\gamma_2\left[\frac{\left(k_1^2+k_2^2\right)\beta_9}{k_1^4k_2^2} + E\frac{\left(k_1^2+k_2^2\right)\beta_{10}}{k_1^4k_2^2} + \ldots\right. \\
\mathcal{K}_{04}^{(4)} =& -\gamma_1\gamma_2\frac{\beta_{17}}{k_1^4} + f\gamma_2\frac{\left(\beta_9+E\beta_{10}+\beta_{13}\right)}{k_1^4} \\
\mathcal{K}_{11}^{(4)} =& \gamma_1^2\left[F\frac{\beta_6}{k_1k_2k_3^2}+G\frac{\beta_7}{k_1k_2k_3^2}+\frac{\beta_{11}\mu}{k_1^2k_2^2}+\frac{\left(k_1^2+k_2^2\right)\beta_{12}}{k_1^3k_2^3}\right] - \gamma_2^2 f\frac{2G}{k_1k_2k_3^2} + \gamma_1\gamma_2\left[\frac{\left(k_1^2+k_2^2\right)\beta_{14}}{k_1^3k_2^3}\right. \\
& \left. +2\frac{\beta_{15}\mu}{k_1^2k_2^2} + \frac{\left(k_1^2+k_2^2\right)\beta_{16}}{k_1^3k_2^3} - 2G\frac{\beta_{19}}{k_1k_2k_3^2}\right] - b_1\gamma_1\frac{\left(k_1^2+k_2^2\right)\left(\beta_4-\beta_3+E\beta_5\right)}{k_1^3k_2^3} - b_1\gamma_2\left[\frac{(k_1^2+k_2^2 \ldots}{k_1^3k_2^3}\right. \\
& \left. +2\frac{\left(k_1^2+k_2^2\right)\beta_9}{k_1^3k_2^3} + 2E\frac{\left(k_1^2+k_2^2\right)\beta_{10}}{k_1^3k_2^3}\right] - b_1 f\gamma_2^2\frac{\left(k_1^2+k_2^2\right)}{k_1^3k_2^3}
\end{aligned}
$$

$$
\begin{aligned}
\mathcal{K}^{(4)}_{13} =& f^2\frac{\gamma_2^2}{k_1^3k_2} + f\gamma_1\frac{(\beta_4-\beta_3+E\beta_5)}{k_1^3k_2} + f\gamma_2\frac{(\beta_8+2\beta_9+2E\beta_{10})}{k_1^3k_2} - \gamma_1^2\frac{(\beta_9+E\beta_{10}+\beta_{13})}{k_1^3k_2} - \gamma_1\gamma_2 (\beta \\
\mathcal{K}^{(4)}_{20} =& \gamma_1\gamma_2\left[\frac{\beta_{14}}{k_2^4} + \frac{\beta_{15}\mu}{k_1k_2^3} + \frac{\beta_{16}}{k_1^2k_2^2} - G\frac{\beta_{19}}{k_2^2k_3^2}\right] - f\gamma_2\left[F\frac{\beta_6}{k_2^2k_3^2} + G\frac{\beta_7}{k_2^2k_3^2} + \frac{\beta_{11}\mu}{k_1k_2^3} + \frac{(k_1^2+k_2^2)\,\beta_{12}}{k_1^2k_2^4}\right] \\
&- f\gamma_2^2\frac{G}{k_2^2k_3^2} - b_1\gamma_1\frac{(\beta_4-\beta_3+E\beta_5)}{k_1^2k_2^2} - b_1\gamma_2\left[\frac{(k_1^2+k_2^2)\,\beta_9}{k_1^2k_2^4} + E\frac{(k_1^2+k_2^2)\,\beta_{10}}{k_1^2k_2^4} + \frac{(k_1^2+k_2^2)\,\beta_{13}}{k_1^2k_2^4}\right. \\
&+ b_1f\frac{(\beta_1-E\beta_2-\gamma_2^2)}{k_1^2k_2^2} \\
\mathcal{K}^{(4)}_{22} =& -\gamma_1^2\frac{(\beta_8+2\beta_9+2E\beta_{10})}{k_1^2k_2^2} - \gamma_1\gamma_2\frac{2\beta_{18}}{k_1^2k_2^2} + f\gamma_1\frac{2\,(\beta_4-\beta_3+E\beta_5)}{k_1^2k_2^2} + f\gamma_2\frac{2\,(\beta_9+E\beta_{10}+\beta_{13})}{k_1^2k_2^2} \\
&+ f^2\frac{(\beta_1+E\beta_2+2\gamma_2^2)}{k_1^2k_2^2} \\
\mathcal{K}^{(4)}_{31} =& f^2\frac{\gamma_2^2}{k_1k_2^3} + f\gamma_1\frac{(\beta_4-\beta_3+E\beta_5)}{k_1k_2^3} + f\gamma_2\frac{(\beta_8+2\beta_9+2E\beta_{10})}{k_1k_2^3} - \gamma_1^2\frac{(\beta_9+E\beta_{10}+\beta_{13})}{k_1k_2^3} - \gamma_1\gamma_2 (\beta \\
\mathcal{K}^{(4)}_{40} =& -\gamma_1\gamma_2\frac{\beta_{17}}{k_2^4} + f\gamma_2\frac{(\beta_9+E\beta_{10}+\beta_{13})}{k_2^4}.
\end{aligned}
$$

$$
\mathcal{K}^{(5)}_{ab} = \begin{pmatrix}
\circ & \bullet & \circ & \bullet & \circ & \circ \\
\bullet & \circ & \bullet & \circ & \circ & \circ \\
\circ & \bullet & \circ & \circ & \circ & \circ \\
\bullet & \circ & \circ & \circ & \circ & \circ \\
\circ & \circ & \circ & \circ & \circ & \circ \\
\circ & \circ & \circ & \circ & \circ & \circ
\end{pmatrix}, \tag{E.4}
$$

with coefficients,

$$
\begin{aligned}
\mathcal{K}^{(5)}_{01} =& \gamma_1\gamma_2\left[\frac{(F\beta_6+G\beta_7)}{k_1^2k_2k_3^2} + \frac{\beta_{11}\mu}{k_1^3k_2^2} + \frac{(k_1^2+k_2^2)\,\beta_{12}}{k_1^4k_2^3}\right] + \gamma_2^2\left[\frac{\beta_{14}}{k_1^4k_2} + \frac{\beta_{15}\mu}{k_1^3k_2^2} + \frac{\beta_{16}}{k_1^2k_2^3} - G\frac{\beta_{19}}{k_1^2k_2k_3^2}\right] \\
&+ b_1\gamma_1\frac{(\beta_1+E\beta_2)}{k_1^2k_2^3} - b_1\gamma_2\frac{(k_1^2+k_2^2)\,(\beta_4-\beta_3+E\beta_5)}{k_1^4k_2^3} \\
\mathcal{K}^{(5)}_{03} =& -\gamma_1\gamma_2\frac{(\beta_9+E\beta_{10}+\beta_{13})}{k_1^4k_2} - \gamma_2^2\frac{\beta_{17}}{k_1^4k_2} + f\gamma_2\frac{(\beta_4-\beta_3+E\beta_5)}{k_1^4k_2} \\
\mathcal{K}^{(5)}_{10} =& \gamma_1\gamma_2\left[\frac{(F\beta_6+G\beta_7)}{k_1k_2^2k_3^2} + \frac{\beta_{11}\mu}{k_1^2k_2^3} + \frac{(k_1^2+k_2^2)\,\beta_{12}}{k_1^3k_2^4}\right] + \gamma_2^2\left[\frac{\beta_{14}}{k_1k_2^4} + \frac{\beta_{15}\mu}{k_1^2k_2^3} + \frac{\beta_{16}}{k_1^3k_2^2} - G\frac{\beta_{19}}{k_1k_2^2k_3^2}\right] \\
&+ b_1\gamma_1\frac{(\beta_1+E\beta_2)}{k_1^3k_2^2} - b_1\gamma_2\frac{(k_1^2+k_2^2)\,(\beta_4-\beta_3+E\beta_5)}{k_1^3k_2^4} \\
\mathcal{K}^{(5)}_{12} =& -\gamma_1^2\frac{(\beta_4-\beta_3+E\beta_5)}{k_1^3k_2^2} - \gamma_2^2\frac{\beta_{18}}{k_1^3k_2^2} - \gamma_1\gamma_2\frac{(\beta_8+3\beta_9+3E\beta_{10}+\beta_{13})}{k_1^3k_2^2} - f\gamma_1\frac{(\beta_1+E\beta_2)}{k_1^3k_2^2} + f\gamma_2 \\
\mathcal{K}^{(5)}_{21} =& -\gamma_1^2\frac{(\beta_4-\beta_3+E\beta_5)}{k_1^2k_2^3} - \gamma_2^2\frac{\beta_{18}}{k_1^2k_2^3} - \gamma_1\gamma_2\frac{(\beta_8+3\beta_9+3E\beta_{10}+\beta_{13})}{k_1^2k_2^3} - f\gamma_1\frac{(\beta_1+E\beta_2)}{k_1^2k_2^3} + f\gamma_2
\end{aligned}
$$

$$\mathcal{K}^{(5)}_{30} = -\gamma_1\gamma_2\frac{(\beta_9 + E\beta_{10} + \beta_{13})}{k_1 k_2^4} - \gamma_2^2\frac{\beta_{17}}{k_1 k_2^4} + f\gamma_2\frac{(\beta_4 - \beta_3 + E\beta_5)}{k_1 k_2^4}.$$

$$\mathcal{K}^{(6)}_{ab} = \begin{pmatrix} \bullet & \circ & \bullet & \circ & \circ & \circ \\ \circ & \bullet & \circ & \circ & \circ & \circ \\ \bullet & \circ & \circ & \circ & \circ & \circ \\ \circ & \circ & \circ & \circ & \circ & \circ \\ \circ & \circ & \circ & \circ & \circ & \circ \\ \circ & \circ & \circ & \circ & \circ & \circ \end{pmatrix}, \tag{E.5}$$

with coefficients,

$$\begin{aligned}
\mathcal{K}^{(6)}_{00} =& \gamma_2^2\left[\frac{(F\beta_6 + G\beta_7)}{k_1^2 k_2^2 k_3^2} + \frac{\beta_{11}\mu}{k_1^3 k_2^3} + \frac{(k_1^2 + k_2^2)\,\beta_{12}}{k_1^4 k_2^4}\right] + b_1\gamma_2\frac{(k_1^2 + k_2^2)\,(\beta_1 + E\beta_2)}{k_1^4 k_2^4} \\
\mathcal{K}^{(6)}_{02} =& -\gamma_1\gamma_2\frac{(\beta_4 - \beta_3 + E\beta_5)}{k_1^4 k_2^2} - \gamma_2^2\frac{(\beta_9 + E\beta_{10} + \beta_{13})}{k_1^4 k_2^2} - f\gamma_2\frac{(\beta_1 + E\beta_2)}{k_1^4 k_2^2} \\
\mathcal{K}^{(6)}_{11} =& \gamma_1^2\frac{(\beta_1 + E\beta_2)}{k_1^3 k_2^3} - 2\gamma_1\gamma_2\frac{\beta_4 - \beta_3 + E\beta_5}{k_1^3 k_2^3} - \gamma_2^2\frac{(\beta_8 + 2\beta_9 + 2E\beta_{10})}{k_1^3 k_2^3} \\
\mathcal{K}^{(6)}_{20} =& -\gamma_1\gamma_2\frac{(\beta_4 - \beta_3 + E\beta_5)}{k_1^2 k_2^4} - \gamma_2^2\frac{(\beta_9 + E\beta_{10} + \beta_{13})}{k_1^2 k_2^4} - f\gamma_2\frac{(\beta_1 + E\beta_2)}{k_1^2 k_2^4}.
\end{aligned}$$

$$\mathcal{K}^{(7)}_{ab} = \begin{pmatrix} \circ & \bullet & \circ & \circ & \circ & \circ \\ \bullet & \circ & \circ & \circ & \circ & \circ \\ \circ & \circ & \circ & \circ & \circ & \circ \\ \circ & \circ & \circ & \circ & \circ & \circ \\ \circ & \circ & \circ & \circ & \circ & \circ \\ \circ & \circ & \circ & \circ & \circ & \circ \end{pmatrix}, \tag{E.6}$$

with coefficients,

$$\begin{aligned}
\mathcal{K}^{(7)}_{01} =& \gamma_1\gamma_2\frac{(\beta_1 + E\beta_2)}{k_1^4 k_2^3} - \gamma_2^2\frac{(\beta_4 - \beta_3 + E\beta_5)}{k_1^4 k_2^3} \\
\mathcal{K}^{(7)}_{10} =& \gamma_1\gamma_2\frac{(\beta_1 + E\beta_2)}{k_1^3 k_2^4} - \gamma_2^2\frac{(\beta_4 - \beta_3 + E\beta_5)}{k_1^3 k_2^4}.
\end{aligned}$$

$$\mathcal{K}_{ab}^{(8)} = \begin{pmatrix} \bullet & \circ & \circ & \circ & \circ & \circ \\ \circ & \circ & \circ & \circ & \circ & \circ \\ \circ & \circ & \circ & \circ & \circ & \circ \\ \circ & \circ & \circ & \circ & \circ & \circ \\ \circ & \circ & \circ & \circ & \circ & \circ \\ \circ & \circ & \circ & \circ & \circ & \circ \end{pmatrix}, \tag{E.7}$$

with coefficient

$$\mathcal{K}_{00}^{(8)} = \gamma_2^2 \frac{(\beta_1 + E\beta_2)}{k_1^4 k_2^4}.$$

F. Squeezed limit of multipoles

These are the leading contributions to the squeezed limits for the multipoles – up to $O(\mathcal{H}/k)$ and $\ell = 3$.

$$B_{0,0} = -2\sqrt{\pi}\frac{P_L P_S}{105}\left[f^4 + \left(-3b_1 - \frac{15}{7}\right)f^3 + \left(-77b_1^2 - 33b_1 - 14b_2 + \frac{14}{3}b_{s^2}\right)f^2 - 105\left(b_1^2 + \frac{3}{2}\right.\right.$$
$$\left.\left. -\frac{4}{9}b_{s^2}\right)b_1 f - 195b_1^2\left(b_1 + \frac{14b_2}{13} - \frac{14b_{s^2}}{39}\right)\right] \tag{F.1}$$

$$B_{1,1} = \sqrt{6\pi}\frac{P_L P_S}{105k_L}\left\{\gamma_1 f^3 + \left(18b_1\gamma_1 - 9\beta_{14} + 6\beta_{16} - 5\beta_{17} + 2\beta_{18} + \frac{15}{7}\gamma_1\right)f^2 + \left[49\gamma_1 b_1^2 + (-42\right.\right.$$
$$+56\beta_{16} - 24\beta_{17} + 12\beta_{18} + 18\gamma_1)\,b_1 + 14\gamma_1\left(b_2 - \frac{b_{s^2}}{3}\right)\Big]f - 35\left[\left(\beta_{14} - 2\beta_{16} + \frac{3\beta_{17}}{5} - \frac{2\beta_{18}}{5}\right.\right.$$
$$\left.\left.\left. -\frac{13\gamma_1}{7}\right)b_1 - 2\gamma_1\left(b_2 - \frac{b_{s^2}}{3}\right)\right]b_1\right\} \tag{F.2}$$

$$B_{2,0} = -4\sqrt{5\pi}f\frac{P_L P_S}{1155}\left[f^3 + \left(-\frac{55}{14} - \frac{11b_1}{2}\right)f^2 + \left(-110b_1^2 - \frac{429}{7}b_1 - 11b_2 + \frac{11}{3}b_{s^2}\right)f\right.$$
$$\left. -231\frac{b_1}{2}\left(b_1^2 + \frac{23}{21}b_1 + \frac{2}{3}b_2 - \frac{2}{9}b_{s^2}\right)\right] \tag{F.3}$$

$$B_{2,2} = 2\sqrt{30\pi}f\frac{P_L P_S}{1155}\left[f^3 + \left(-\frac{11b_1}{6} - \frac{55}{42}\right)f^2 + \left(-44b_1^2 - \frac{99}{7}b_1 - 11b_2 + \frac{11}{3}b_{s^2}\right)f\right.$$
$$\left. -77\frac{b_1}{2}\left(b_1^2 + \frac{13}{7}b_1 + 2b_2 - \frac{2}{3}b_{s^2}\right)\right] \tag{F.4}$$

$$B_{3,1} = \sqrt{21\pi}\frac{P_L P_S}{165k_L}\left\{\gamma_1 f^3 + \left[\frac{418}{21}b_1\gamma_1 - \frac{33}{7}\beta_{14} + \frac{22}{7}\beta_{16} - 5\beta_{17} + 2\beta_{18} + \frac{440}{147}\gamma_1\right]f^2 + \left[\frac{143\gamma_1 b_1^2}{7}\right.\right.$$
$$\left(-\frac{99\beta_{14}}{7} + \frac{22\beta_{16}}{7} - \frac{77\beta_{17}}{3} + \frac{242\beta_{18}}{21} + \frac{792\gamma_1}{49}\right)b_1 + \frac{88\gamma_1}{7}\left(b_2 - \frac{b_{s^2}}{3}\right)\Big]f - b_1^2\frac{132}{7}\left(\beta_{17} - \right.$$
$$\tag{F.5}$$

$$B_{3,3} = -f\sqrt{35\pi}\frac{P_L P_S}{1155k_L}\left[\gamma_1 f^2 + \left(\frac{22b_1\gamma_1}{3} - 5\beta_{17} + 2\beta_{18} - 11\beta_{14} + \frac{22\beta_{16}}{3}\right)f - 11\left(-3b_1\gamma_1 + \beta_1\right.\right.$$
$$\left.\left. + 3\beta_{14} - 6\beta_{16}\right)b_1\right] \tag{F.6}$$

G. SNR Euclid

Newtonian kernels in eqn

$$F_2(\boldsymbol{k}_1,\boldsymbol{k}_2) = \frac{10}{7} + \hat{\boldsymbol{k}}_1 \cdot \hat{\boldsymbol{k}}_2\left(\frac{k_1}{k_2} + \frac{k_2}{k_1}\right) + \frac{4}{7}\left(\hat{\boldsymbol{k}}_1 \cdot \hat{\boldsymbol{k}}_2\right)^2 , \tag{G.1}$$

$$G_2(\boldsymbol{k}_1,\boldsymbol{k}_2) = \frac{6}{7} + \hat{\boldsymbol{k}}_1 \cdot \hat{\boldsymbol{k}}_2\left(\frac{k_1}{k_2} + \frac{k_2}{k_1}\right) + \frac{8}{7}\left(\hat{\boldsymbol{k}}_1 \cdot \hat{\boldsymbol{k}}_2\right)^2 , \tag{G.2}$$

$$Z_2(\boldsymbol{k}_1,\boldsymbol{k}_2) = f\frac{\mu_1\mu_2}{k_1k_2}\left(\mu_1k_1 + \mu_2k_2\right)^2 + \frac{b_1}{k_1k_2}\left[\left(\mu_1^2 + \mu_2^2\right)k_1k_2 + \mu_1\mu_2\left(k_1^2 + k_2^2\right)\right] , \tag{G.3}$$

$$S_2(\boldsymbol{k}_1,\boldsymbol{k}_2) = \left(\hat{\boldsymbol{k}}_1 \cdot \hat{\boldsymbol{k}}_2\right)^2 - \frac{1}{3} . \tag{G.4}$$

Fitting formulas for Fig.figure curves

$$b_1(z) = 0.9 + 0.4z\,, \quad b_2(z) = -0.741 - 0.125\,z + 0.123\,z^2 + 0.00637\,z^3\,, \tag{G.5}$$

$$b_{s^2}(z) = 0.0409 - 0.199\,z - 0.0166\,z^2 + 0.00268\,z^3\,, \tag{G.6}$$

$$V(z) = 8.85\,z^{1.65}\exp\left(-0.777\,z\right)\,h^{-3}\,\mathrm{Gpc}^3\,, \tag{G.7}$$

$$n_g(z) = 0.0193\,z^{-0.0282}\exp\left(-2.81\,z\right)\,h^3\,\mathrm{Mpc}^{-3}\,, \tag{G.8}$$

$$\sigma(z) = \left(5.29 - 0.249\,z - 0.720\,z^2 + 0.187\,z^3\right)\,h^{-1}\,\mathrm{Mpc}\,. \tag{G.9}$$

Number of orientation bins

Figure G.1 shows the effect on the relativistic total SNR of changing the number of orientation bins, $n_{\mu_1} = N_{\mu_1}/\Delta\mu_1 = 2/\Delta\mu_1$ and $n_\varphi = N_\varphi/\Delta\varphi = 2\pi/\Delta\varphi$. It is apparent that reducing the number of bins increases the cumulative SNR. The cumulative SNR converges towards a minimum for $n_{\mu_1}, n_\varphi > 40$. We choose $n_{\mu_1} = n_\varphi = 50$, which is equivalent to eq.

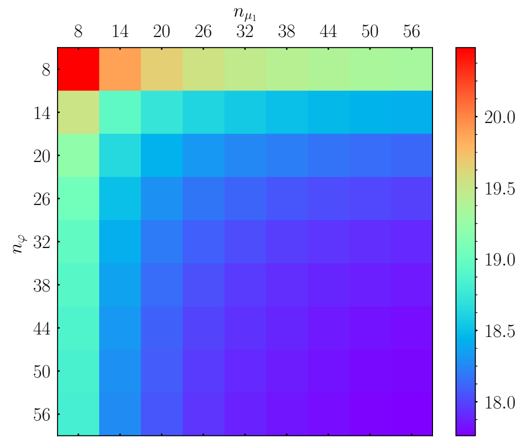

Figure G.1.: Effect on total relativistic SNR of changing number of φ and μ_1 bins.

Effect of changing magnification and evolution biases

The effect on the relativistic SNR of changes in magnification bias and in evolution bias is illustrated in Fig. G.2.

Comparison with Jeong & Schmidt (2020)

In Jeong & Schmidt (2020), a significant number of terms is neglected in the relativistic second-order galaxy number count contrast, $\delta^{(2)}_{g\mathrm{D}}$, given by our (4.4). (Note that our (4.4), derived in Clarkson et al. (2019), was independently confirmed by Di Dio & Seljak (2019)). They have the first term, $A\,\boldsymbol{v}^{(2)}\cdot\boldsymbol{n}$, on the right of (4.4). In the second term, $2C(\boldsymbol{v}\cdot\boldsymbol{n})\,\delta$, they do not have the correct form of the coefficient C – they include only the first part, b_1A, of C [see the right-hand side of eq 26?]. All terms after the second term in (4.4) are omitted by Jeong & Schmidt (2020). Note that none of the omitted terms is suppressed by a higher power of k^{-1}; they all have the same scaling, i.e., $\propto (\mathcal{H}/k)\,(\delta)^2$. In detail, they omit the following terms:

$$\delta^{(2)}_{g\mathrm{D}}(\mathrm{us}) - \delta^{(2)}_{g\mathrm{D}}(\text{Jeong \& Schmidt (2020)}) = 2\left[b_1 f + \frac{b_1'}{\mathcal{H}} + 2\left(1-\frac{1}{r\mathcal{H}}\right)\frac{\partial b_1}{\partial \ln L}\bigg|_{\mathrm{c}}\right](\boldsymbol{v}\cdot\boldsymbol{n})\,\delta \tag{G.10}$$

$$+\frac{2}{\mathcal{H}}\left(4-2A-\frac{3}{2}\Omega_m\right)(\boldsymbol{v}\cdot\boldsymbol{n})\,\partial_r(\boldsymbol{v}\cdot\boldsymbol{n})$$

$$+\frac{2}{\mathcal{H}^2}\left[(\boldsymbol{v}\cdot\boldsymbol{n})\,\partial_r^2\Phi - \Phi\,\partial_r^2(\boldsymbol{v}\cdot\boldsymbol{n})\right] - \frac{2}{\mathcal{H}}\,\partial_r(\boldsymbol{v}\cdot\boldsymbol{v}) + 2\frac{b_1}{\mathcal{H}}\Phi$$

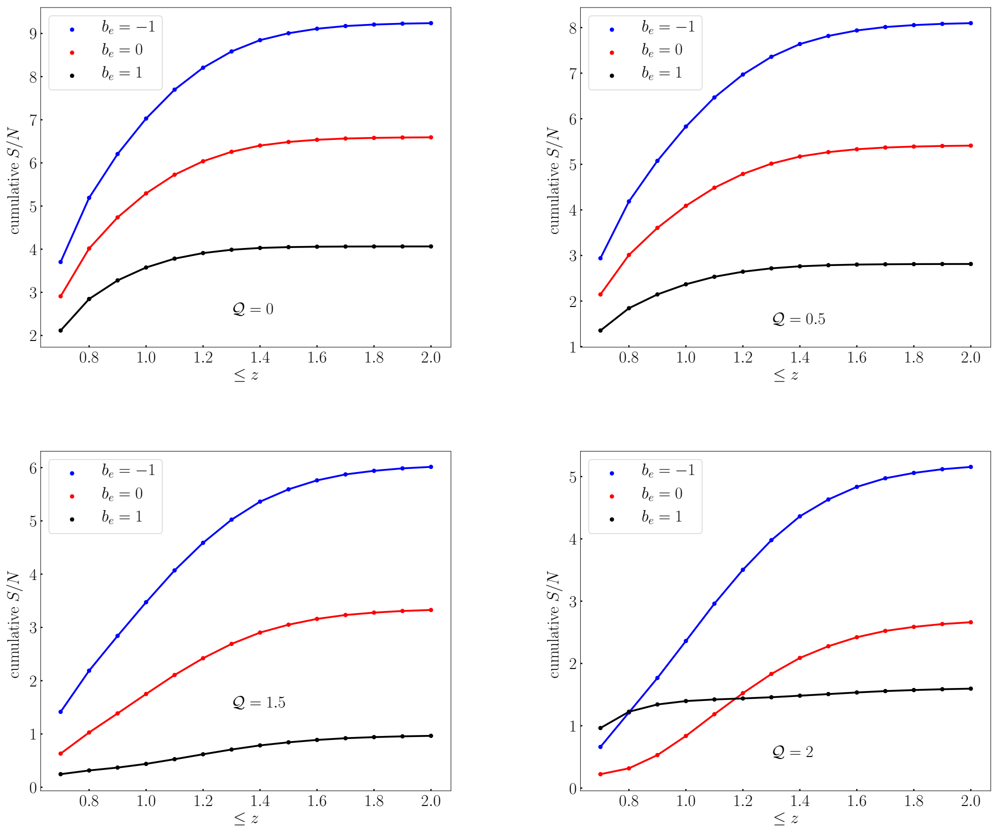

Figure G.2.: Effect of changing $\mathcal{Q}$ and b_e on relativistic cumulative SNR.

H. HI intensity mapping

Bibliography

Abramo L. R., Bertacca D., 2017, Physical Review D, 96

Aghanim N., et al., 2018

Alonso D., Ferreira P. G., 2015, Phys. Rev. D, 92, 063525

Alonso D., Bull P., Ferreira P. G., Maartens R., Santos M., 2015, Astrophys. J., 814, 145

Baldauf T., Seljak U., Senatore L., 2011, JCAP, 1104, 006

Ballardini M., Matthewson W. L., Maartens R., 2019, Mon. Not. Roy. Astron. Soc., 489, 1950

Barreira A., 2020, JCAP, 12, 031

Barreira A., Cabass G., Schmidt F., Pillepich A., Nelson D., 2020, JCAP, 12, 013

Bartolo N., et al., 2016, Phys. Dark Univ., 13, 30

Bernal J. L., Bellomo N., Raccanelli A., Verde L., 2020, JCAP, 10, 017

Bernardeau F., Colombi S., Gaztañaga E., Scoccimarro R., 2002, Physics Reports, 367, 1–248

Bertacca D., 2015, Class. Quant. Grav., 32, 195011

Bertacca D., Maartens R., Clarkson C., 2014a, JCAP, 09, 037

Bertacca D., Maartens R., Clarkson C., 2014b, JCAP, 1411, 013

Bertacca D., Bartolo N., Bruni M., Koyama K., Maartens R., Matarrese S., Sasaki M., Wands D., 2015, Class. Quant. Grav., 32, 175019

Bertacca D., Raccanelli A., Bartolo N., Liguori M., Matarrese S., Verde L., 2018, Phys. Rev., D97, 023531

Beutler F., Castorina E., Zhang P., 2019, JCAP, 03, 040

Bharadwaj S., Mazumdar A., Sarkar D., 2020, Mon. Not. Roy. Astron. Soc., 493, 594

Bolejko K., Clarkson C., Maartens R., Bacon D., Meures N., Beynon E., 2013, Phys. Rev. Lett., 110, 021302

Bonvin C., 2008, Phys. Rev. D, 78, 123530

Bonvin C., 2014, Class. Quant. Grav., 31, 234002

Bonvin C., Durrer R., 2011, Phys. Rev. D, 84, 063505

Bonvin C., Fleury P., 2018, JCAP, 05, 061

Bonvin C., Hui L., Gaztanaga E., 2014, Phys. Rev. D, 89, 083535

Bonvin C., Hui L., Gaztanaga E., 2016, JCAP, 08, 021

Bruni M., Crittenden R., Koyama K., Maartens R., Pitrou C., Wands D., 2012, Phys. Rev. D, 85, 041301

Bruni M., Hidalgo J. C., Meures N., Wands D., 2014, Astrophys. J., 785, 2

Camera S., Santos M. G., Maartens R., 2015a, Mon. Not. Roy. Astron. Soc., 448, 1035

Camera S., Maartens R., Santos M. G., 2015b, Mon. Not. Roy. Astron. Soc., 451, L80

Camera S., Fonseca J., Maartens R., Santos M. G., 2018, Mon. Not. Roy. Astron. Soc., 481, 1251

Castorina E., White M., 2018, Mon. Not. Roy. Astron. Soc., 476, 4403

Celoria M., Matarrese S., 2020, Proc. Int. Sch. Phys. Fermi, 200, 179

Challinor A., Lewis A., 2011, Phys. Rev. D, 84, 043516

Chan K. C., Blot L., 2017, Phys. Rev. D, 96, 023528

Clarkson C., de Weerd E. M., Jolicoeur S., Maartens R., Umeh O., 2019, Monthly Notices of the Royal Astronomical Society, 486, L101

Dai L., Pajer E., Schmidt F., 2015, JCAP, 10, 059

Dalal N., Dore O., Huterer D., Shirokov A., 2008, Phys. Rev. D, 77, 123514

Desjacques V., Jeong D., Schmidt F., 2018, Phys. Rept., 733, 1

Di Dio E., Seljak U., 2019, JCAP, 04, 050

Di Dio E., Durrer R., Marozzi G., Montanari F., 2014, JCAP, 12, 017

Di Dio E., Durrer R., Marozzi G., Montanari F., 2016, JCAP, 01, 016

Di Dio E., Perrier H., Durrer R., Marozzi G., Moradinezhad Dizgah A., Noreña J., Riotto A., 2017, JCAP, 1703, 006

Di Dio E., Durrer R., Maartens R., Montanari F., Umeh O., 2019, JCAP, 04, 053

Durrer R., Jalilvand M., Kothari R., Maartens R., Montanari F., 2020, JCAP, 12, 003

Fonseca J., Camera S., Santos M., Maartens R., 2015, Astrophys. J. Lett., 812, L22

Fonseca J., Maartens R., Santos M. G., 2017, Mon. Not. Roy. Astron. Soc., 466, 2780

Fonseca J., Maartens R., Santos M. G., 2018, Mon. Not. Roy. Astron. Soc., 479, 3490

Gagrani P., Samushia L., 2017, Mon. Not. Roy. Astron. Soc., 467, 928

Gaztanaga E., Bonvin C., Hui L., 2017, JCAP, 01, 032

Giannantonio T., Porciani C., 2010, Phys. Rev. D, 81, 063530

Gil-Marín H., Percival W. J., Verde L., Brownstein J. R., Chuang C.-H., Kitaura F.-S., Rodríguez-Torres S. A., Olmstead M. D., 2017, Mon. Not. Roy. Astron. Soc., 465, 1757

Grimm N., Scaccabarozzi F., Yoo J., Biern S. G., Gong J.-O., 2020, JCAP, 11, 064

Hall A., Bonvin C., 2017, Phys. Rev. D, 95, 043530

Hall A., Bonvin C., Challinor A., 2013, Phys. Rev. D, 87, 064026

Iršič V., Di Dio E., Viel M., 2016, JCAP, 02, 051

Jeong D., Komatsu E., 2009, Astrophys. J., 703, 1230

Jeong D., Schmidt F., 2020, Phys. Rev. D, 102, 023530

Jeong D., Schmidt F., Hirata C. M., 2012, Physical Review D, 85

Jolicoeur S., Umeh O., Maartens R., Clarkson C., 2017, JCAP, 09, 040

Jolicoeur S., Umeh O., Maartens R., Clarkson C., 2018, JCAP, 03, 036

Jolicoeur S., Allahyari A., Clarkson C., Larena J., Umeh O., Maartens R., 2019, JCAP, 03, 004

Jolicoeur S., Maartens R., De Weerd E. M., Umeh O., Clarkson C., Camera S., 2020

Kaiser N., 1987, Mon. Not. Roy. Astron. Soc., 227, 1

Karagiannis D., Lazanu A., Liguori M., Raccanelli A., Bartolo N., Verde L., 2018, Monthly Notices of the Royal Astronomical Society, 478, 1341–1376

Karagiannis D., Fonseca J., Maartens R., Camera S., 2020a

Karagiannis D., Slosar A., Liguori M., 2020b, JCAP, 11, 052

Kehagias A., Moradinezhad Dizgah A., Noreña J., Perrier H., Riotto A., 2015, JCAP, 08, 018

Koyama K., Umeh O., Maartens R., Bertacca D., 2018, JCAP, 07, 050

Lepori F., Di Dio E., Villa E., Viel M., 2018, JCAP, 05, 043

Lepori F., Iršič V., Di Dio E., Viel M., 2020, JCAP, 04, 006

Lewis A., Challinor A., Lasenby A., 2000, Astrophys. J., 538, 473

Liguori M., Sefusatti E., Fergusson J. R., Shellard E. P. S., 2010, Adv. Astron., 2010, 980523

Lopez-Honorez L., Mena O., Rigolin S., 2012, Phys. Rev. D, 85, 023511

Lorenz C. S., Alonso D., Ferreira P. G., 2018, Phys. Rev. D, 97, 023537

Maartens R., Jolicoeur S., Umeh O., De Weerd E. M., Clarkson C., Camera S., 2020, JCAP, 2020, 065–065

Majumdar S., Pritchard J. R., Mondal R., Watkinson C. A., Bharadwaj S., Mellema G., 2018, Mon. Not. Roy. Astron. Soc., 476, 4007

Matarrese S., Verde L., 2008, Astrophys. J. Lett., 677, L77

Matarrese S., Pilo L., Rollo R., 2021, JCAP, 01, 062

McDonald P., 2009, JCAP, 11, 026

Moradinezhad Dizgah A., Biagetti M., Sefusatti E., Desjacques V., Noreña J., 2020

Nan Y., Yamamoto K., Hikage C., 2018, JCAP, 07, 038

Oddo A., Sefusatti E., Porciani C., Monaco P., Sánchez A. G., 2020, JCAP, 03, 056

Okoli C., Scrimgeour M. I., Afshordi N., Hudson M. J., 2017, Mon. Not. Roy. Astron. Soc., 468, 2164

Pan H., Obreschkow D., Howlett C., Lagos C. d. P., Elahi P. J., Baugh C., Gonzalez-Perez V., 2019

Pozzetti L., et al., 2016, Astron. Astrophys., 590, A3

Raccanelli A., Bertacca D., Doré O., Maartens R., 2014, JCAP, 08, 022

Raccanelli A., Montanari F., Bertacca D., Doré O., Durrer R., 2016, JCAP, 05, 009

Raccanelli A., Bertacca D., Jeong D., Neyrinck M. C., Szalay A. S., 2018, Phys. Dark Univ., 19, 109

Sargent W. L. W., Turner E. L., 1977, The Astrophysical Journal, 212, L3

Sarkar D., Majumdar S., Bharadwaj S., 2019, Mon. Not. Roy. Astron. Soc., 490, 2880

Scoccimarro R., 2015, Phys. Rev. D, 92, 083532

Scoccimarro R., Couchman H. M. P., Frieman J. A., 1999, The Astrophysical Journal, 517, 531–540

Scoccimarro R., Sefusatti E., Zaldarriaga M., 2004, Phys. Rev. D, 69, 103513

Sefusatti E., Komatsu E., 2007, Phys. Rev. D, 76, 083004

Sefusatti E., Crocce M., Pueblas S., Scoccimarro R., 2006, Phys. Rev. D, 74, 023522

Shirasaki M., Sugiyama N. S., Takahashi R., Kitaura F.-S., 2021, Phys. Rev. D, 103, 023506

Smith R. E., et al., 2003, Mon. Not. Roy. Astron. Soc., 341, 1311

Sugiyama N. S., Saito S., Beutler F., Seo H.-J., 2018, Monthly Notices of the Royal Astronomical Society, 484, 364–384

Sugiyama N. S., Saito S., Beutler F., Seo H.-J., 2020, Mon. Not. Roy. Astron. Soc., 497, 1684

Tansella V., Bonvin C., Durrer R., Ghosh B., Sellentin E., 2018, JCAP, 03, 019

Tellarini M., Ross A. J., Tasinato G., Wands D., 2015, JCAP, 07, 004

Tellarini M., Ross A. J., Tasinato G., Wands D., 2016, Journal of Cosmology and Astroparticle Physics, 2016, 014–014

Tram T., Fidler C., Crittenden R., Koyama K., Pettinari G. W., Wands D., 2016, JCAP, 05, 058

Umeh O., Koyama K., 2019, JCAP, 12, 048

Umeh O., Maartens R., Santos M., 2016, JCAP, 03, 061

Umeh O., Jolicoeur S., Maartens R., Clarkson C., 2017, JCAP, 03, 034

Umeh O., Koyama K., Maartens R., Schmidt F., Clarkson C., 2019, JCAP, 1905, 020

Umeh O., Koyama K., Crittenden R., 2020

Verde L., Heavens A. F., Matarrese S., Moscardini L., 1998, Monthly Notices of the Royal Astronomical Society, 300, 747–756

Verde L., Wang L.-M., Heavens A., Kamionkowski M., 2000, Mon. Not. Roy. Astron. Soc., 313, L141

Villa E., Rampf C., 2016, JCAP, 1601, 030

Villumsen J. V., 1995

Wang M. S., Beutler F., Bacon D., 2020, Mon. Not. Roy. Astron. Soc., 499, 2598

Watkinson C. A., Majumdar S., Pritchard J. R., Mondal R., 2017, Mon. Not. Roy. Astron. Soc., 472, 2436

Yankelevich V., Porciani C., 2019, Mon. Not. Roy. Astron. Soc., 483, 2078

Yoo J., 2010, Phys. Rev. D, 82, 083508

Yoo J., Zaldarriaga M., 2014, Phys. Rev. D, 90, 023513

Yoo J., Fitzpatrick A. L., Zaldarriaga M., 2009, Phys. Rev. D, 80, 083514

Yoo J., Hamaus N., Seljak U., Zaldarriaga M., 2012, Phys. Rev. D, 86, 063514

de Putter R., Doré O., Green D., 2015, JCAP, 10, 024

de Weerd E. M., Clarkson C., Jolicoeur S., Maartens R., Umeh O., 2020, JCAP, 05, 018

List of Figures

List of Tables